공학박사학위논문

구조화된 레이저 조명 평면 이미징 기법을 이용한 기체중심 동축 와류형 분사기의 동적 특성 연구

A Study on Dynamic Characteristics of Gas-centered Swirl Coaxial Injectors Using Structured Laser Illumination Planar Imaging Technique

2021년 2월

서울대학교 대학원

기계항공공학부

정 기 정

구조화된 레이저 조명 평면 이미징 기법을 이용한 기체중심 동축 와류형 분사기의 동적 특성 연구

A Study on Dynamic Characteristics of Gas-centered Swirl Coaxial Injectors Using Structured Laser Illumination Planar Imaging Technique

지도교수 윤 영 빈

이 논문을 공학박사 학위논문으로 제출함

2020 년 12 월

서울대학교 대학원

기계항공공학부

정 기 정

정기정의 공학박사 학위논문을 인준함

2021 년 2 월

위 원 장 : 余載翊

부위원장 : 尹寧彬

위 원 : 李福植

위 원 : 具滋叡

위 원 : 南宮赫濬

ABSTRACT

In liquid rocket engine systems such as the staged combustion cycle with high efficiency, the propellant is introduced into the combustion chamber in the form of gas-liquid. Since a nozzle for accelerating the combustion products is connected behind the cylindrical chamber in the case of a general axisymmetric combustor, the gas which is not completed the combustion reaction may be exhausted. Therefore, it is necessary to use a swirl injector that can increase the travel distance and residence time with the same axial displacement comparing to the jet injectors.

In the case of a gas-centered coaxial gas-liquid swirl injector, gas and liquid could interact inside the injector, if a recessed region is applied. Also, the liquid spray characteristics influenced by the wall of the central injector. As the wall thickness of the inner injector (lip thickness) increased, liquid film region in the swirl chamber and nozzle was invaded, and consequently, the liquid spray angle decreased. Therefore, when the gas injection angle is constant, the gas and liquid flow may collide with each other outside the injector if the liquid spray angle decreased. In this study, the spray pattern and spray angle were measured by the backlight method using a stroboscope for the internal and external mixing type sprays. However, it was difficult to figure out the mechanism of liquid breakup because the liquid film decomposed into a large number of small droplets near the outlet of the injector due to the central gas vortex. Therefore, real-time instantaneous information on the distribution of liquid ligaments and droplets in the spray section was obtained by using a planar laser and a 2-phase structured laser illumination planar imaging (2p-SLIPI) technique that eliminated multiple scattering. Also, a dynamic pressure sensor was used to measure the pressure vibration of gas injection. Since the gas vortex discharged through the swirl type injector moved in the axial direction while rotating, it pushed the inner surface of the liquid film outwardly, and at the same time, it was accompanied a entrainment effect by pressure drop in interspace of liquid and gas flow. In the internal mixing spray, a fine droplet zone was created around the injector axis as the gas stream scraped the liquid film from the mixing chamber (recessed region). In the external mixing spray, the liquid film is ruptured by gas impingement on the film. Thus, the fine droplets are distributed in a hollow cone shape. The droplets in liquid spray of a single swirl injector are created by the wave – ligament model caused by the gas-liquid interaction. However, in the case of the external mixed-type binary injector, the effect of gas was more dominant to the liquid film breakup process than the inherent liquid flow characteristics. In addition, the pressure oscillation of the gas causes the liquid film to vibrate, and as a result, the liquid film is periodically disrupted generating droplets. In this process, the fracture frequency was transited from gas acoustic frequency and the liquid film wave frequency. However, there was also some spraying condition where the fracture frequency was not appeared. In general, it was found that the fracture frequency was proportional to the gas impinging velocity and the liquid velocity, and the aerodynamic resistance of the liquid film could have different effects on the frequency and amplitude.

Keywords: Gas centered gas-liquid injector, Gas swirl injector, Droplet formation, 2p SLIPI, Liquid rocket engine

Student Number: 2015-31003

LIST

CHAPTER 4

CHAPTER 5

CHAPTER 6

LIST OF FIGURES

LIST OF TABLES

NOMENCLATURE

Alphabet

2p-SLIPI – two phase structured laser illumination planar imaging

BL – breakup length

CMOS – complementary metal–oxide–semiconductor

FFT – fast Fourier transform

GCSC – gas-centered swirl coaxial gas-liquid injector

IP – distance from injector head to impinging position

PTU – programmable time unit

Re – Reynolds number

We – Weber number

A – Amplitude

d – diameter (mm)

F – area (mm^2)

f – frequency (Hz)

h – film length (cm)

J – momentum flux ratio

t – liquid film thickness (mm)

u – velocity (m/s)

Δp – differential pressure (bar)

μ – coefficient of viscosity (Pa·s)

σ – coefficient of surface tension (N/m)

θ – impinging angle (deg)

Subscripts

g – gas

l – liquid

n – normal vector

r – radial axis

z – vertical axis (axis of injector)

CHAPTER 1

INTRODUCTION

The conventional engines such as R-4D, TR-308, S-400, 11D458M and 11D428A-14, which are used in the launch vehicle upper stage and manned and unmanned spacecraft use hypergolic propellants. Recently, small engines are being developed which use harmless propellants to the human body as manned planetary exploration is being pursued again. However, the phase of the propellant, the suitable type of injector system, and the cooling method are not fully established for these propellants. It is known that most of non-toxic propellants have cryogenic and non-hypergolic characteristics and gas phase propellant component is required for the small size combustion chamber.

European countries and Russia have used small engines with single bipropellant injectors for decades. Prior to applying the single gas-liquid injector type to the engine, it is necessary to consider a conventional small rocket engine of a similar type. As mentioned above, the hypergolic propellant is mostly used because of operational advantages, and the phase of the propellant flowing from the injector to the combustion chamber is liquid-liquid state at room temperature. The European Airbus Astrium S400 engine and Russian NIIMASh 11D428A and 11D459M are equipped with a coaxial bipropellant injector and apply hydrazine type (MMH, UDMH) and nitric oxide materials as fuel and oxidizer. In all three cases, the oxidizer is located outside, and the spray angle is larger than the fuel spray cone. This is because the oxidizer film has a cooling effect. Depending on the material of the combustion chamber, the radiative cooling and the relationship between the temperature distribution of the combustion products and the dimensions of the combustion chamber geometry may necessitate the application of additional cooling systems as in the case of Russian engine.

Jet injectors and swirl injectors are widely used type. Some injectors for gas-liquid propellant can be considered. There are several representative injectors for applying gas-liquid propellants. For example, there are some cases in which the inner gas jet injector and the outer liquid swirl injector are constructed, such as the RD-8. Varying the position of two injectors with each other can also be considered, and since the combustion chamber volume is small and the length is short, a swirl injector can be considered instead of a gas jet injector Fig. 1.1.

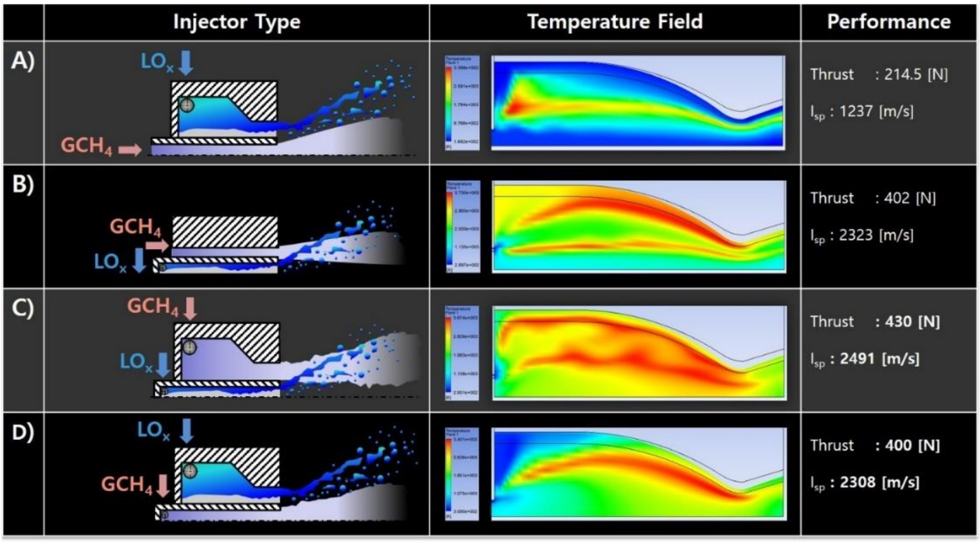

	Injector Type	Temperature Field	Performance
A)	LO_x GCH_4		Thrust : 214.5 [N] I_{sp} : 1237 [m/s]
B)	GCH_4 LO_x		Thrust : 402 [N] I_{sp} : 2323 [m/s]
C)	GCH_4 LO_x		**Thrust : 430 [N]** **I_{sp} : 2491 [m/s]**
D)	LO_x GCH_4		**Thrust : 400 [N]** **I_{sp} : 2308 [m/s]**

Figure 1.1 Comparison of injector types by numerical analysis [Lee (2019)].

The most important parameter for determining the interaction of the two injectors is the difference in momentum between the two propellants, and the representative parameter is a difference in spray angle. Therefore, it is necessary to get the changes in atomization characteristics when the gas spray angle is constant and the liquid spray angle is changed, and the relationship between the fluid-dynamic characteristics and the geometrical parameters of the injector is examined.

The inner gas injector can be selected as open type with considering an ignition plug mounted on the center. In order to design the injector, the initial values were set as the spray angle and the injection pressure drop, and the lip thickness *t* and the recess number RN were determined as factors affecting the interaction between the gas injector and liquid injector. Liquid injector is designed by the methodology of Kurpatenkov (1987) and Dityakin (1977) and gas injector was designed by modifying the standard of the Russian standard (GOST 21980-76). The shape of the manifold was determined by referring to technical report of NASA [Gill & Nurick (1976)].

According to Kurpatenkov (1987), the spray characteristics are affected by the ratio between the outer diameter of the inner injector nozzle and the radius of outer liquid film surface, when the wall of the inner injector invades the liquid film of the outer injector (see Fig. 1.2). That is, as the lip thickness increases under the same design conditions, the outer liquid spray angle decreases.

In liquid rocket engines, operational instability can be characterized by combustion chamber performance parameters oscillating over a certain range [Dranovsky & Mark (2007)]. Depending on the type of propulsion system, there are complex mechanisms due to various factors, but it is generally known that high-frequency instability occurs as a result of pressure oscillations caused by the interaction between the combustion chamber and the propellant flowing into the chamber [Dranovsky & Mark (2007), Vasilev et al. (1975)]. Since the injector is an element that directly introduces the propellant into the combustion chamber, it is inevitable that it plays an important role in the dynamic system. It is also known that the dynamic characteristics of the injector have an indirect effect on the atomization of the liquid propellant and the mixing between the fuel and the oxidizer [Andreev et al. (1991)].

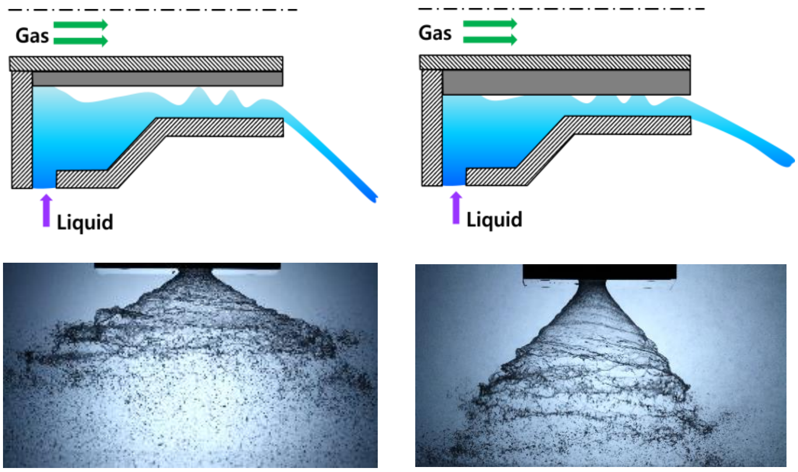

(a) (b)

Figure 1.2 Influence of small (a) and large (b) lip thickness on the spray angle.

In a system using a pre-burner or in a system in which one of the propellant components is vaporized in a regenerative cooling passage, the propellant entering the combustion chamber may have a gas-liquid phase. Gas-liquid injectors can be distinguished as internally mixed injectors in which gas-liquid interaction begins in the mixer (recessed zone), and externally mixed injectors in which liquid film and gas flow collide in the combustion chamber. Also, it can be classified into liquid-centered (LCSC) and gas-centered (GCSC) injectors depending on the arrangement of the stages.

Andreev et al. (1991), and Bazarov & Yang (1998) studied the dynamic characteristics of a gas-liquid injector with a liquid swirl stage at the center and an annular gas discharge at the outside. In this type, the gas passing through the jet injector was vibrated by the resistance of the liquid film in the mixer, which generated self-pulsation of the liquid film. Im et al. (2009) studied the relationship between the self-pulsation and the Reynolds number of gas and liquid in this type of gas-liquid injector. Fu & Yang (2010) proposed a theoretical model for the self-pulsation of the entire gas-liquid injector as a combination of the transfer function of the liquid injector stage and the mixer.

GCSC injectors have been mainly used in Russian closed-cycle liquid rocket engines RD-8, RD-120, RD-0208 and RD-170 series [Dranovsky & Mark (2007)]. Park et al. (2017) confirmed the relationship between the liquid film oscillation frequency and spray characteristics in the GCSC injector using the gas jet injector depending on of the gap thickness and recess length in the presence of gas perturbation.

CHAPTER 2

EXPERIMENT AND MEASUREMENT SYSTEMS

2.1 Spray Test Facility for Swirl Injector and Measuring Method

Spray images are taken by Canon EOS 7D camera with Canon 180 mm f / 3.5 L lens to measure the spray angle and obtain the overall shape of the spray. A single lamp stroboscope (MS-230DA, SUGAWARA Laboratories Inc., Japan, flash duration time less than 6 μs) was used as the light source and it is linked with camera setup (shutter speed 1/50, F/13, ISO-2000). The stroboscope was used to measure the spray angle and obtain the overall shape of the spray. Stroboscope and digital camera were installed as shown in Figure 2.1. In gas-liquid spray, it is difficult to understand the shape near the injector exit by small droplets.

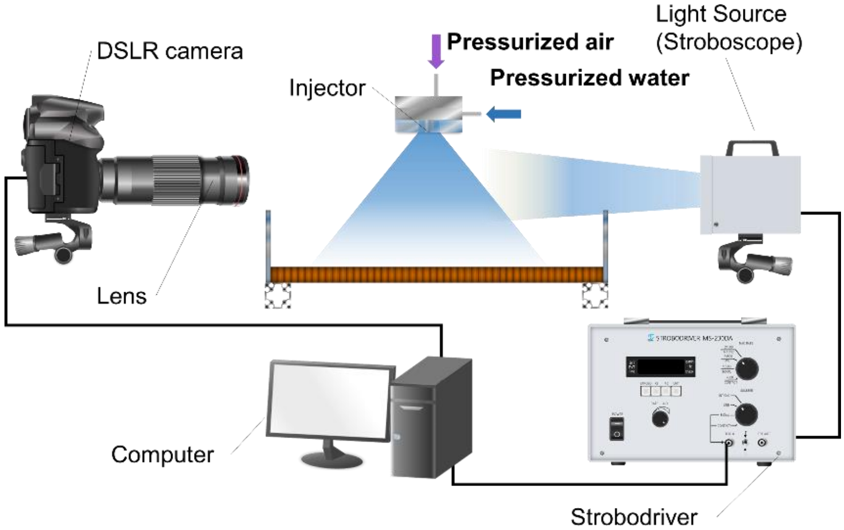

Figure 2.1 Schematic of experimental arrangement for the spray angle measurement.

When the liquid film is decomposed by gas flow, it is not easy to detect the boundary of the spray from a single instantaneous image, since the vibration of the liquid film and atomization near the injector outlet. Therefore, instantaneous images taken by digital camera were superimposed to produce an averaged image to obtain a clear boundary. As the distance from the injector outlet increases, droplets are scattered by the rotating turbulent gas flow. In this reason, the spray angle should be determined in the area adjacent to the injector outlet even on an averaged image. Near the exit of the injector, there is an area where the liquid film and ligaments exist (see Fig. 2.2). This zone was defined from the point where the axial distance from the injector exit was 2.5 mm to the point where white pixels were detected at the center of the spray. The linearized boundary in this region can be obtained through a linear detection algorithm using the Hough transform method. Due to partial liquid film breakup and vibration, the actual boundary consists of a curve similar to the Rias coastline. For this reason, since the angle of the detected straight line is not constant, 1000 straight lines are detected and averaged. The spray angle was obtained using the averaged angle of straight lines. According to the spray angle detection method used in this paper, it is considered that it is not easy to perform error analysis.

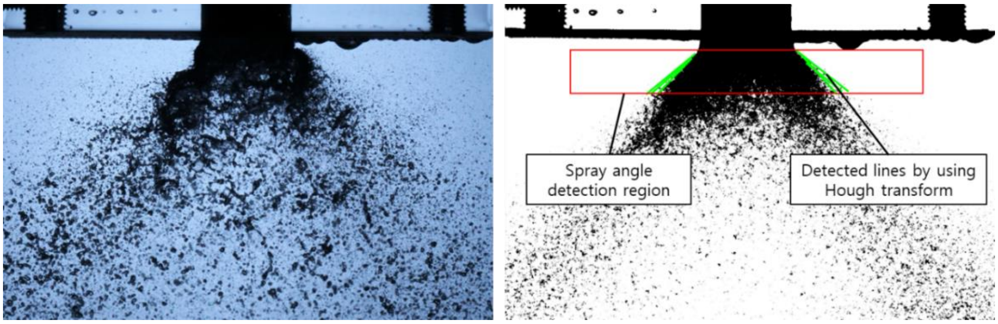

(a) (b)

Figure 2.2 Determination of gas-liquid spray angle: (a) Instant spray image, (b) Binarized average spray image (external mixing spray, Δp_l = 2 bar, Δp_g = 6 bar).

2.2 Two-phase Structured Laser Illumination Planar Imaging(2p-SLIPI) Technique

An electromagnetic wave incident on an arbitrary particle or droplet causes the electron cloud to vibrate or perturb. This creates an induced dipole moment by periodically separating charges in a molecule composed of a proton and an electron with discrete charges (Fig. 2.3). This acceleration motion causes the charge to emit electromagnetic waves (scattered light) consistently in all directions. The phase relationship depends on the size and shape of the particle and the angle of detection. In other words, scattering does not appear simply by reflecting electromagnetic waves from the surface of the particles. The scattered light passes through the lens and is detected by the receiver (P).

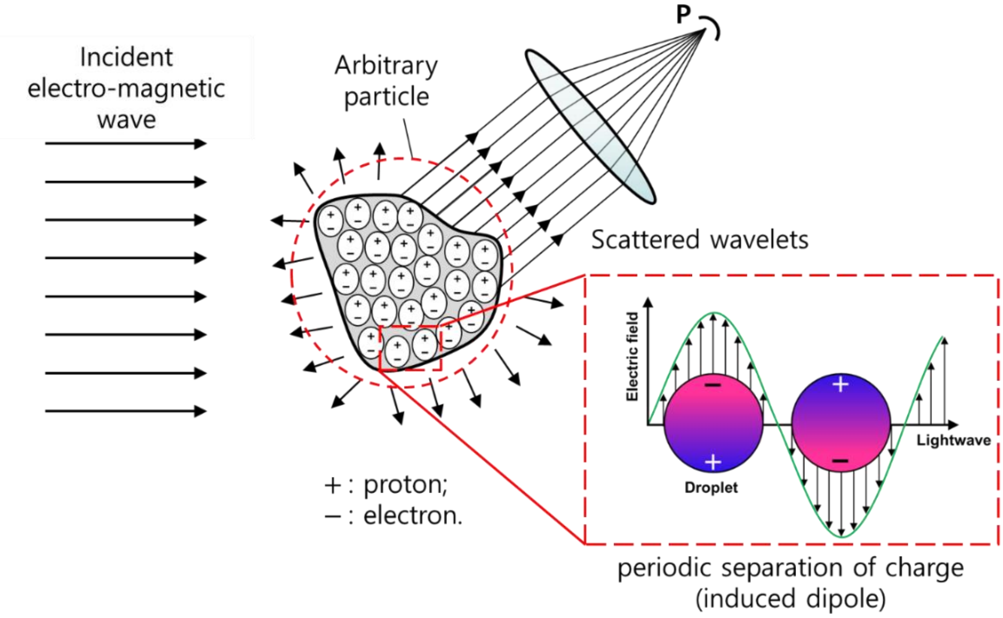

Figure 2.3 Physics of scattering by a single particle [Bohren & Human (1983)].

Elastic scattering refers to a scattering process in which the wavelengths of incident light and scattered light are the same. $\bar{\boldsymbol{x}}$ is a dimensionless number for the wavelength and droplet diameter of an electromagnetic wave, which becomes parameter to classify Rayleigh scattering and Mie scattering [Kristensson (2012) and Hahn (2009)]. The case where the wavelength of the incident light and the diameter of the droplet are similar is called Mie scattering:

where, $\bar{x}$: dimensionless particle size (diameter), *d*: diameter of spherical particle, λ_0: incident wavelength, m_0 – refractive index of the surrounding medium.

$$\bar{x} = \frac{\pi d}{\lambda_0 / m_0} \tag{2.1}$$

Table 2.1. Elastic scattering identified by particle size [Kristensson, (2012)].

$\bar{x} \ll 1$	Rayleigh	Wavelength > particle size
$\bar{x} \approx 1$	Mie	Wavelength ≈ particle size
$\bar{x} \gg 1$	Geometric	Wavelength < particle size

As shown in Equation (2.2), the optical depth τ and the transmittance *T*, which are the amount of light removed by scattering or absorption according to the Lambert-Beer law, can be calculated as follows: where, I_0: original intensity, I_t: transmitted signal, τ: optical depth, γ: attenuation coefficient, *s*: signal path.

$$T = \frac{I_t}{I_0} = I_0 e^{-\tau} = I_0 e^{\left[-\int_0^L \gamma(s) ds\right]} \tag{2.2}$$

Light propagating in a cloudy medium is divided into three modes according to its optical depth. When a photon is detected through a single scattering, it is in the optically diluted regime. In intermediate scattering regime, average scattering frequency is 1 to 10 times and transmittance is less than 37%. It is called 'optically dense' state. The case with the number of scattering more than 10 times is called as 'multiple scattering regime'. In this state, it can be said that it is the distributed regime where the dominant number of scattering does not exist.

Since the intensity contribution in the detection of multiple scattered photons cannot be expressed mathematically, the accuracy and precision of the measurement can be seriously degraded. Fig 2.4 is a schematic diagram of the various paths that can be taken before photons are detected. A is the direct scattered light, and paths B, C can give an incorrect interpretation of the origin of the scattering event. In the case of D, it is an accurate image of the droplet, but it can be said that the contribution of the intensity deviates from the Beer-Lambert law.

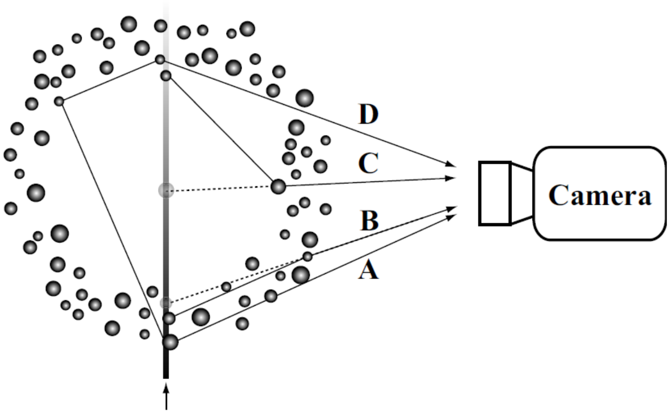

Figure 2.4 Schematic of signal path to the camera [Kristensson (2012)].

Eq. (2.3) is the intensity of the ray passing through the path L, where I_{MS}: undesired multiple light scattering intensity.

$$I(L) = I_0 \cdot e^{-\bar{\gamma} \cdot L} + I_{MS} \tag{2.3}$$

As shown in Fig. 2.5, gas-liquid spray is a multiple scattering state with low transmittance (*T*) and large optical depth (τ) due to dense fine droplets. A clearer image can be obtained as shown in Fig. 2.5 if a technique is used to remove multiple scattering.

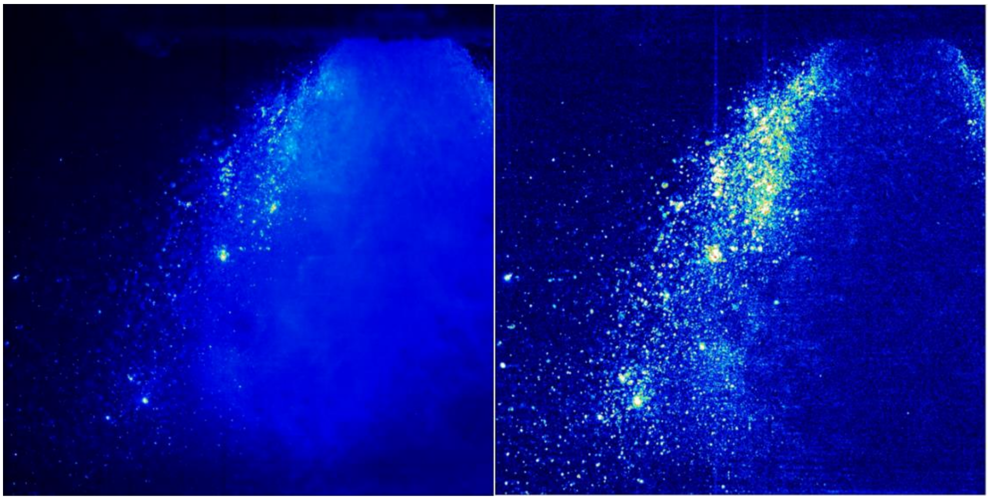
(a) (b)

Figure 2.5 Longitudinal section of spray images (a) with multiple scattering, and (b) removed multiple scattering.

SLIPI technology can be used to remove such multiple scattering Mie signals. Three phase SLIPI and two-phase SLIPI can be briefly expressed as Eqs. (2.4) and (2.5), respectively. Since multiple scattered signals are not modulated, they are removed from the difference between each modulated image (Berrocal, 2016). Unlike the synthesis of 3p-SLIPI [Figure 2.6 (a)], the fringe point inevitably arises because 2p-SLIPI has a phase difference between 180 degrees [Figure 2.6 (b)]. A low-pass filter (Gaussian filter) was used to remove these fringe points. This filter is a kind of smoothing technique in which the convolution method is applied.

$$I_{3P-SLIPI} = \frac{\sqrt{2}}{3} \cdot \sqrt{(I_0 - I_{120})^2 + (I_0 - I_{240})^2 + (I_{120} - I_{240})^2} \tag{2.4}$$

$$I_{2P-SLIPI} = \frac{\sqrt{2}}{2} \cdot \sqrt{(I_0 - I_{180})^2} + F_{2v} \tag{2.5}$$

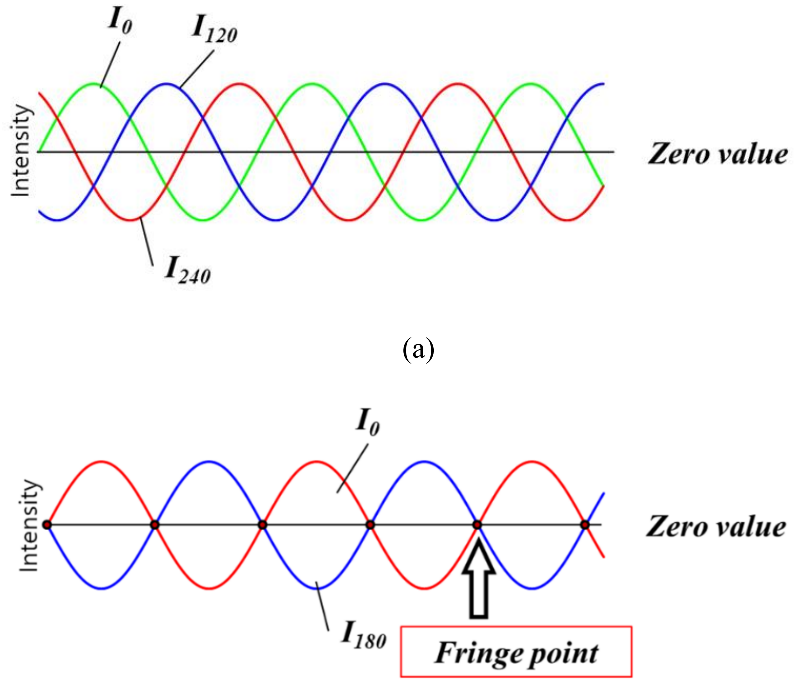

(a)

(b)

Figure 2.6 Synthesis of sinusoidal light structure (a) 3p-SLIPI and (b) 2p-SLIPI.

Fig 2.7 describes the image processing process of two-phase SLIPI. In images modulated by 0 and 180 degrees, a speckle pattern is found. In each image, the location of the droplet was not clearly revealed due to multiple scattering. The fringe point left a thin stripe in the subtraction of the two modulated images $[(\sqrt{2}/2) \cdot$

$\sqrt{(I_0 - I_{180})^2}$], although the blurry part was removed. The image after applying the filter (F_{2v}) is placed on the right.

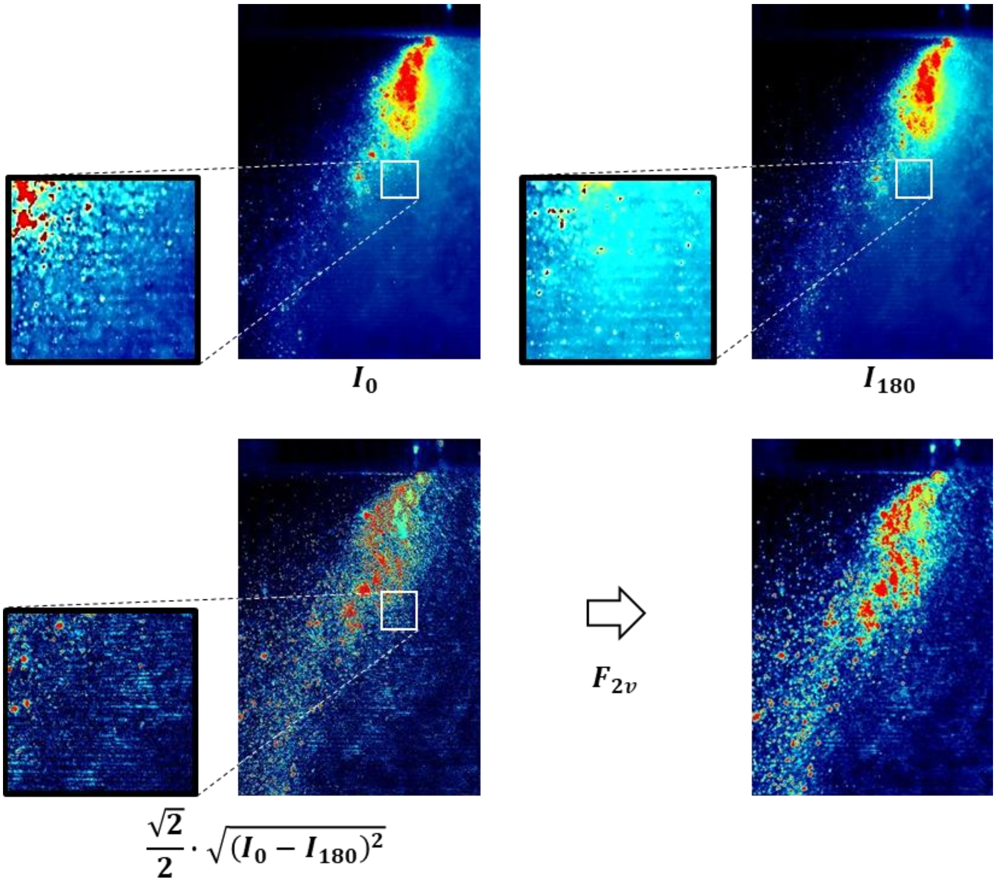

Figure 2.7 Spray image processing by 2p-SLIPI technique [Jeong et al. (2020)].

For this structured laser illumination planar imaging (SLIPI) technique, optical devices as shown in Fig. 2.8 were used. The installation form is similar to that of a structured illumination microscope (SIM). First, it expands the laser beam like a Galileo telescope. Next, light is passed through the aperture to remove Gaussian intensity. Use the Ronchi grating mask to create a speckle pattern. In order to obtain an optimized spray image, the grating period was set to approximately 10 pixels/period. Crossed polarized (homogeneous intensity distribution) light is required for two-phase (2p) SLIPI by using a beam displacer and λ/2-waveplate. Cylindrical lens was installed to correct the horizontal and vertical position of the laser beam. An imaging lens was used to receive a polarized light signal into the camera sensor in a rectangular shape.

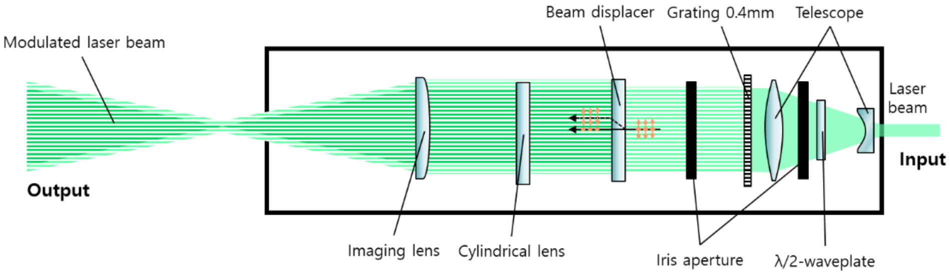

Figure 2.8 Arrangement of optics for 2p-SLIPI technique (side view).

The equipment for measuring the spray longitudinal section is shown in Fig. 2.9 [Jeong et al. (2019)]. Dual head Nd: YLF diode pumped Q-switched green lasers (DM20-527 / DH laser) of Photonics Industries International, Inc. were used as the light source. The wavelength of the laser was 527nm and the operating pulse rate of each single shot was 3500Hz synchronized with the CMOS camera. The laser was irradiated to the spray center through a SLIPI optics module (LaVision GmbH, Germany) connected to an optical articulated arm. The CMOS high-speed camera (FASTCAM SA5 Type 775K-M2) was located in the direction looking at the center of the spray at an angle of 90 degrees relative to the direction of the laser. A Canon 180mm f / 3.5L lens was attached to the camera. LaVision's programmable timing unit (PTU X) was used to synchronize the acquired signals between equipment components. The hardware connection of the laser, computer, and camera was made by PTU X and the equipment elements were controlled by the software Davis 8.4 (LaVision GmbH, Germany). The laser pulse separation time of the laser was set to 10μs, and 1024×1024pixel images were taken at a rate of 3500Hz and 512×512pixel images - for 7000Hz. The image resolution was 0.0861 mm / pixel.

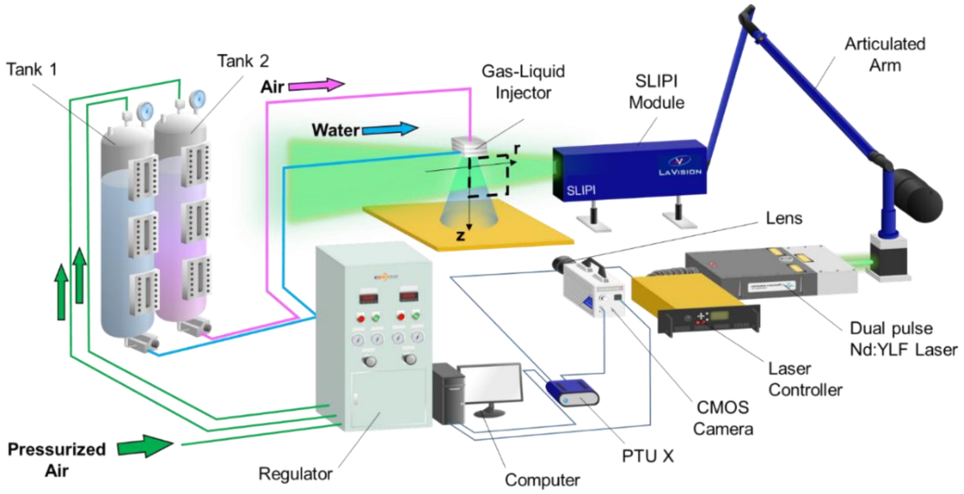

Figure 2.9 Experimental setup–Schematic of experimental arrangement for the laser measurement with 2p-SLIPI module [Jeong et al. (2020)].

2.3 Method for Droplet Size Measurement

As shown in Fig 2.3, the size of the droplet can be obtained by the Mie signal generated by the laser beam incident on the droplet. In Fig. 2.10(a), the image by Mie scattering on the right side of the spray is shown. The size occupied by the spray profile in the original image is 850 × 990 pixels. Fig 2.11 is a binarized image when the critical intensity (I_{cr}) is changed from 25 to 200 after post-processing using the SLIPI technique. In the image with $I_{cr} = 25$, the number and boundary of the droplets are somewhat unclear. However, if it was increased to $I_{cr} = 200$, it appeared to be divided into two particles. In order to binarize the image to define the boundary of the droplets, a reference value is required. The method of determining the boundary of the droplet may be used intensity gradient. But a method of comparing the data using the shadowgraphy method was chosen in this study.

At the top of the spray, the transmittance of light from the stroboscope is significantly reduced by liquid film, ligament and droplets. Therefore, backlight shadowgraphy was performed at $z = 80mm$ where the droplet could be identified as shown in Fig 2.10(a). Only droplet information within the range of 5 mm × 5 mm could be obtained at a time since a microscope and a Barlow lens were used. Images were acquired with an interval of 5mm from the center of the injector to the position of $r = 80mm$.

According to Im et al (2010), Kim and Lee (2007), and Otsu (1979), the appropriate threshold value for binarization of gray level histogram is 0.8. Sauter mean diameter (SMD) values at each point were calculated from data obtained from 900 images taken with sufficient time intervals, which are presented as 'Norm' points in Figure 2.10 (b). The resolution of images taken with the SLIPI technique is 86.14 μm/pixel, so if the diameter of the droplets obtained by shadowgraphy is smaller than 86.14 μm, they are ignored. The minimum average error (< 5%) $I_{cr} =100$ was set as the reference intensity as shown in Figure 2.5(b), from result of comparing the SMD values obtained in the first step with the SMD values at each measurement position in the second step calculated according to the potential reference intensities (I_{cr}). The two-dimensional position data of the droplet diameter distribution could be derived in the order shown in Figure 2.10 (c) using the obtained reference intensity. The image was binarized in the first step, and in the second step, pixel chunks were identified as droplets. Then, the diameter/position data according to the class of droplet size was calculated.

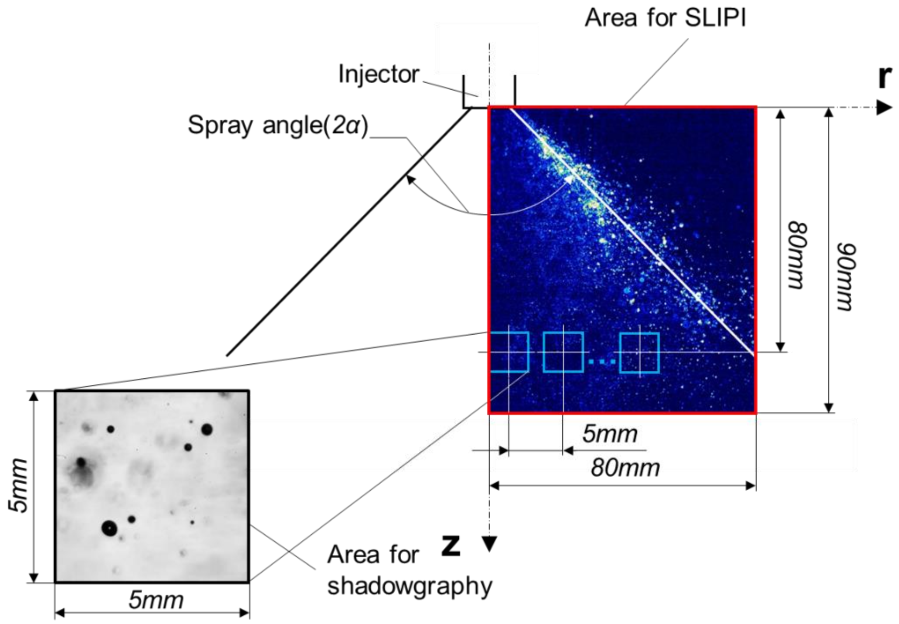
Area for SLIPI
Injector
Spray angle(2α)
r
80mm
90mm
5mm
5mm
80mm
5mm
z
Area for shadowgraphy

(a)

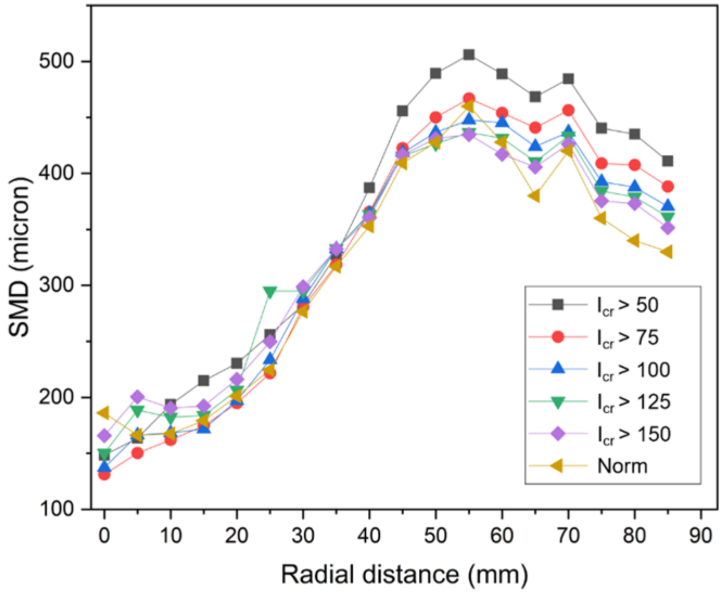
SMD (micron)
500
400
300
200
100
0
10
20
30
40
50
60
70
80
90
Radial distance (mm)
I_{cr} > 50
I_{cr} > 75
I_{cr} > 100
I_{cr} > 125
I_{cr} > 150
Norm

(b)

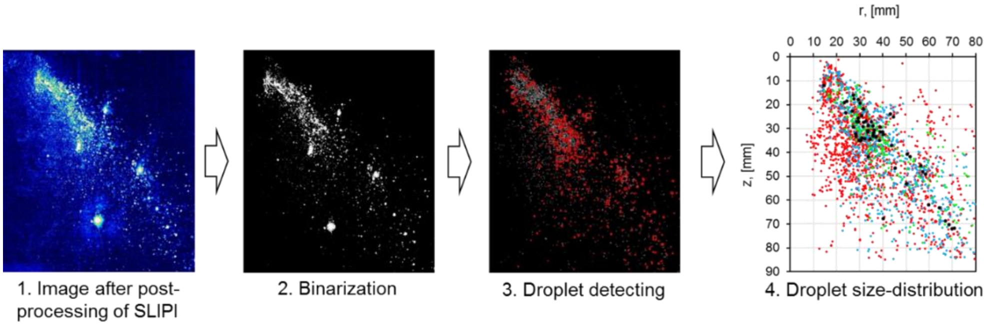

1. Image after post-processing of SLIPI

2. Binarization

3. Droplet detecting

4. Droplet size-distribution

(c)

Figure 2.10 Droplet detection method: (a) Measuring position, (b) calibration, and (c) diameter-position detection process [Jeong et al. (2020)].

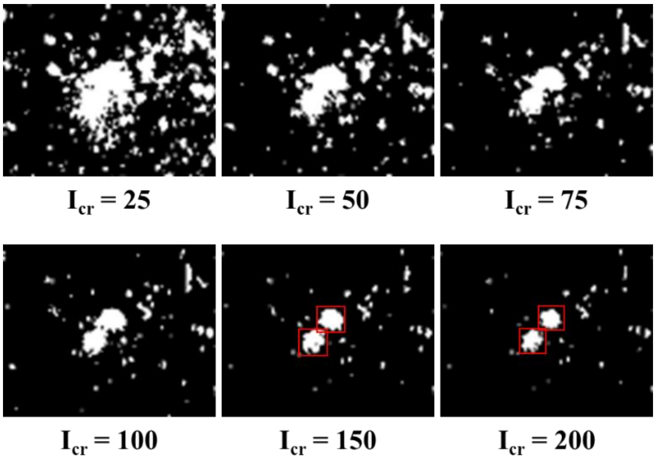

$I_{cr} = 25$ $I_{cr} = 50$ $I_{cr} = 75$

$I_{cr} = 100$ $I_{cr} = 150$ $I_{cr} = 200$

Figure 2.11 Binarization of images according to critical intensity.

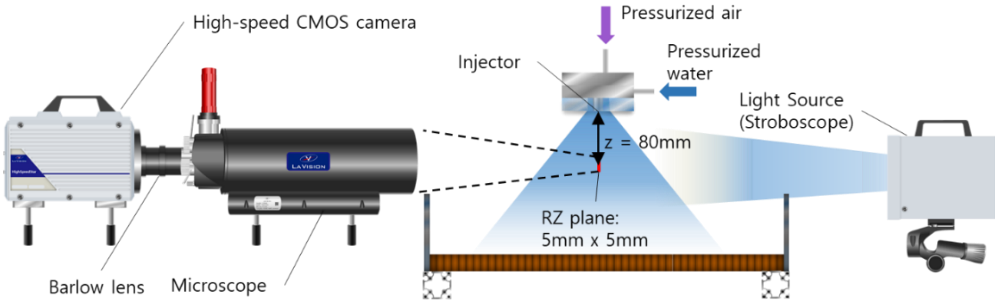

Figure 2.12 Equipment arrangement for droplet measurement by backlight shadowgraphy.

2.4 Method for Dynamic Analysis of Spray Image

Continuous instantaneous images were obtained using method which was used by Jeong (2020) to obtain the frequency characteristics of the spray according to each supply condition. In the binarized image post-processed with the 2p-SLIPI technique, it is believed that the bright part is occupied by the liquid in the spray cross section. According to Jeong et al. (2019), the pattern gradually faded downstream because the small droplets produced by the gas mixed with the ambient air. Therefore, as indicated by the red line in Fig. 2.13, the variation of the liquid distribution was measured in the distance range from the spray center at the vertical position near the injector outlet to the position with very few droplets in the outer radial direction.

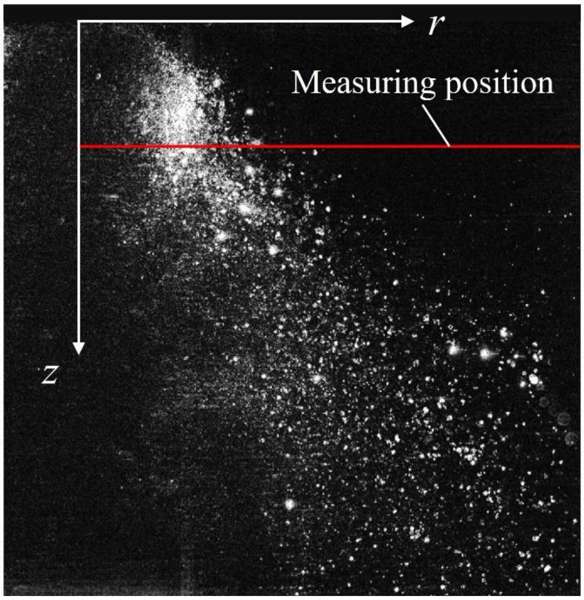

Figure 2.13 Binarized post-processed image.

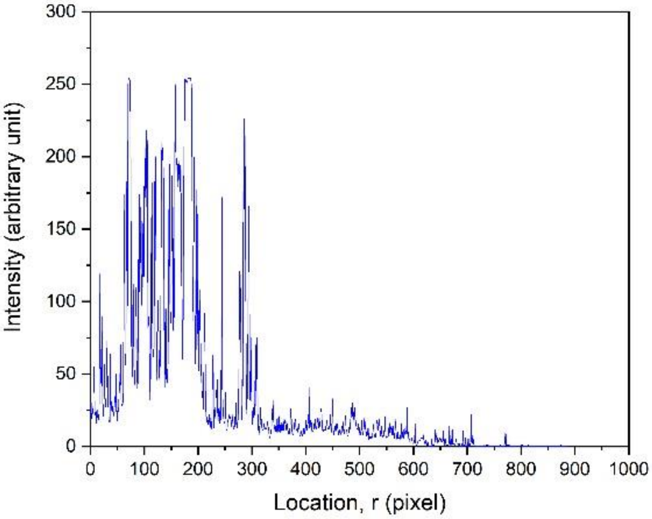

(a)

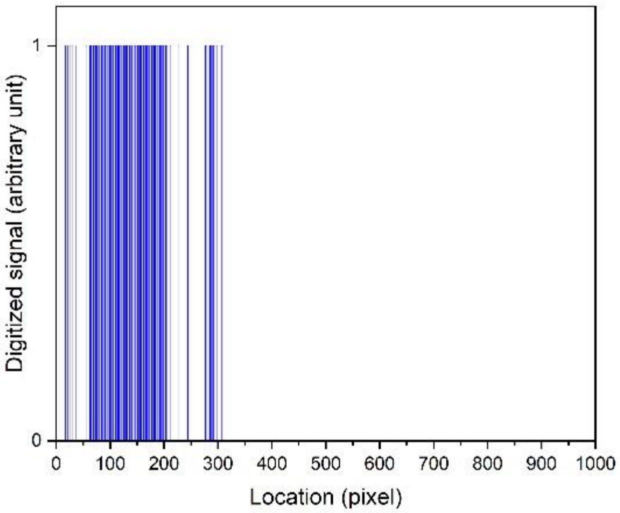
Digitized signal (arbitrary unit)
1
0
0
100
200
300
400
500
600
700
800
900
1000
Location (pixel)

(b)

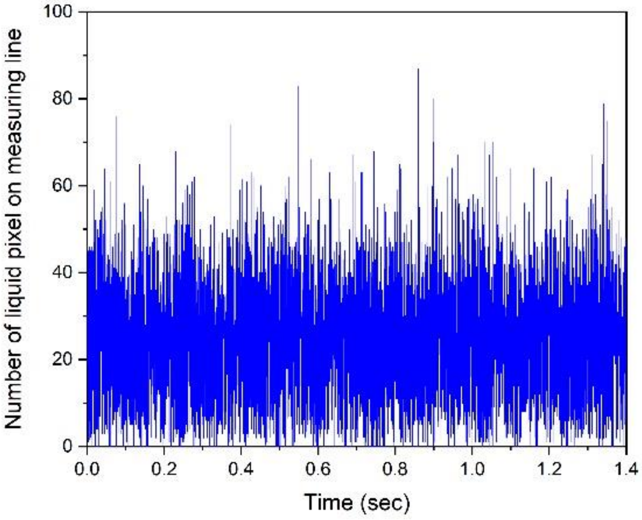
Number of liquid pixel on measuring line
100
80
60
40
20
0
0.0
0.2
0.4
0.6
0.8
1.0
1.2
1.4
Time (sec)

(c)

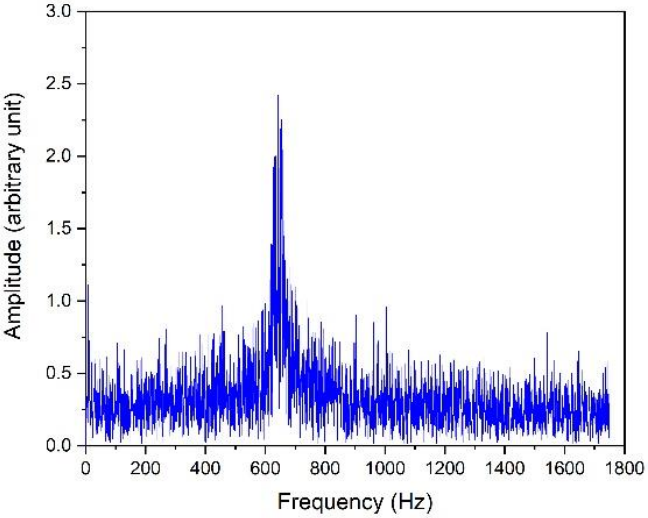

(d)

Figure 2.14 (a) Intensity profile at the detecting line for an image, (b) Binarized signal from liquid position for an image, (c) Oscillation of liquid passing through the detecting line, (d) FFT result.

In one image, the intensity of each pixel on the red line is shown in Fig. 2.14 (a). Here, an intensity of less than 50 was regarded as noise, and a value above noise was determined to be a Mie signal from a liquid. The liquid signal was converted to 1 and the background to 0 [see Fig. 2.7 (b)]. As shown in Fig. 2.14 (c), the number of liquid signals passing through the detecting line oscillated over time. The frequency-amplitude characteristics were derived using the fast Fourier transform (FFT) method [see Fig. 2.14 (d)].

CHAPTER 3

ATOMIZATION AND DISTRIBUTION OF DROPLETS IN GAS-LIQUID SPRAYS BY COAXIAL SWIRL INJECTORS

3.1 Objectives and Test Conditions

Propellants with low toxicity to humans should be used for use on manned spacecraft. Hydrazine-based propellants, which have been used in space shuttles and manned spaceships, can seriously damage the vascular system, nervous system, and skin even in very small amounts in the air. Hydrazine-based propellants give fatal damage to blood vessel-nerve system and skin. Allowable concentration in air lower than $0.5 \cdot 10^{-6}\ mg/L$ [Kozlov, A. A., et al. (1977)]. So, safety inspection is necessary even after landing. In addition to manned space exploration attempts currently being promoted in each country, engines using non-toxic propellants are being developed.

Swirl injectors add rotational speed to the fluid being injected compared to jet injectors. Therefore, it increases the total travel distance for the same axial displacement. Accordingly, the combustion efficiency may be increased since the residence time of the droplets in the combustion chamber is increased. In liquid rocket engines, the propellant component that has passed through the pre-burner or the cooling passage of the combustion chamber can be introduced into the combustion chamber as a gas phase. According to Lefebvre (1968), coaxial gas-liquid injectors using these gas components have the advantage of accelerating atomization by turbulent high-speed gases as well as an instability mechanism due to vibration of the liquid film [Clark and Dombrowski (1972)]. Therefore, gas-liquid swirl injectors need to be used in small rocket engines with small chamber volumes.

Fig. 3.1 is a conceptual diagram of a small engine combustion chamber using non-hypergolic (diergolic) propellant. Non-hypergolic propellants require additional equipment for ignition, unlike widely used hydrazine-based propellants. According to the engine structure, it is most reasonable to place the igniter on the engine axis. And according to Kochanov et al. (2017), spark igniter has more advantage than the pyrogen ignition type. If a gas swirl injector mounted on the center, fine oxidizer droplets may be guided to the igniter by the recirculation zone near the outlet, but the effect may be somewhat insufficient upon restart. Therefore, it can be considered to put low flow rate of liquid oxidizer into the ignition chamber for starting. In small engines, the propellant may escape to the nozzle before the combustion process is complete due to the small combustion chamber volume. This point is known as an important consideration when designing a small engine. Due to the use of vortex type injectors, the flame is stabilized and also allows sufficient time to burn even in small combustion chambers with short lengths. In addition, an oxidizer-rich zone is formed in the vicinity of the combustion chamber wall and in front of the flame wall of the head, since the liquid oxidizer film is sprayed on the outside. Film cooling effects can be expected in such a low temperature region. In addition, it is possible to cool the gas injector wall and increase the temperature of the liquid oxidizer as the oxidizer film surrounds the gas injector. Of course, this concept needs to check the expected effect through several test processes such as droplet velocity field analysis in the high-pressure environment, real propellant spray test, and hot fire test.

According to Andreev et al. (2017), the gas vortex continues the combustion process afterwards due to the vortex structure formed near the injector outlet. In addition, cooling due to convective heat exchange accompanying the eddy current may inhibit the downstream propagation of the high temperature flow in the ignition chamber. Tashev (2014) used an open-type gas swirl injector and studied the engine in which this injector acts as an ignition chamber. In the closed-type gas swirl injector, there is a risk of explosion due to sudden pressure increase during combustion or starting. Therefore, in this study, a gas-centered gas-liquid injector equipped with an open-type gas injector was used in consideration of the above-mentioned characteristics.

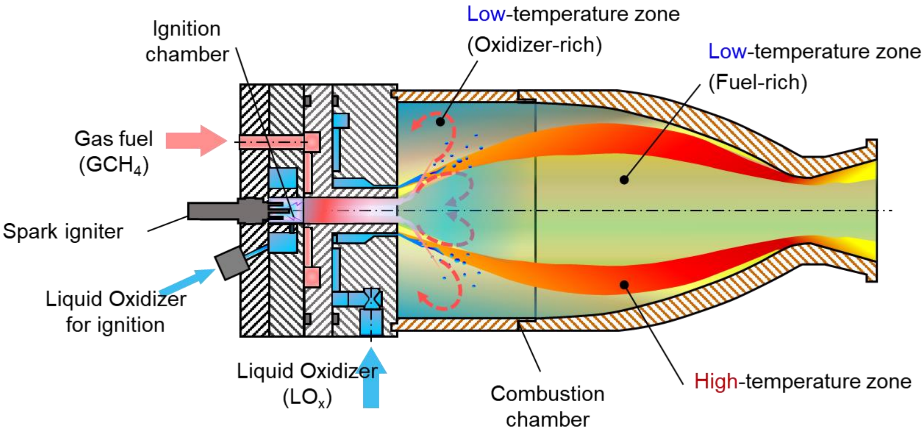

Figure 3.1 Concept of combustion chamber model with non-hypergolic gas-liquid propellant.

As studied by Kim et al (2007) and Im et al (2010), coaxial injectors can be divided into two spray types: internal mixing and external mixing type. The internal mixing injector has a mixing chamber that allows liquid and gas to meet before exiting the outlet. In the external mixing type injector, the gas flow impinges on the liquid film outside the outlet of the injector to provoke atomization process.

Figure 3.2 shows schematic illustrations of the injector and Table 1 shows the geometric parameters used in the experiments (Jeong et al., 2019 a, b). The object used in the experiments was a coaxial gas–liquid injector with a gas swirl injector centered in a liquid swirl injector. Individual liquid and gas injectors and manifolds were designed with reference to the methods presented by Yang et al. (2004) and Gill and Nurick (1976). Closed-type liquid injectors were chosen and open-type gas injectors were selected. In the design of the coaxial injectors, the geometrical parameters between the inner and outer injectors influence the spraying effect (Park et al., 2016).

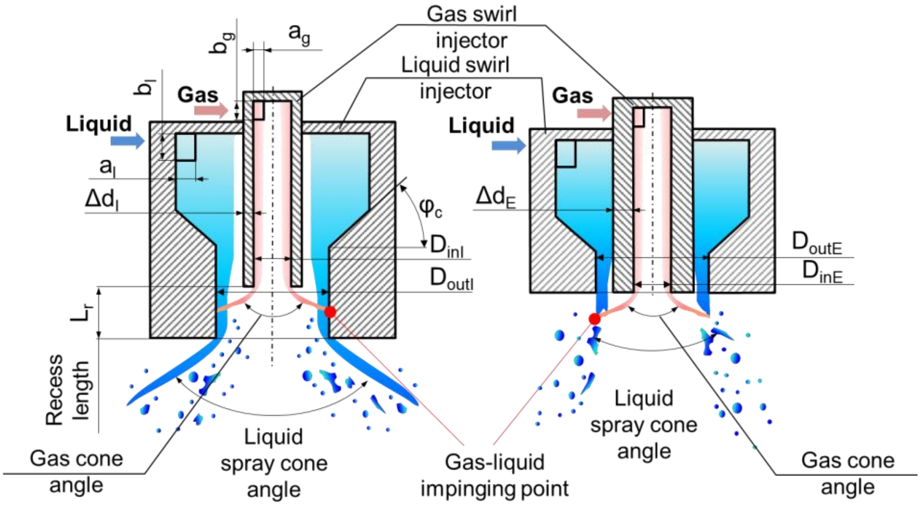

(a) (b)

Figure 3.2 Schematics of coaxial gas-liquid injectors: (a) – Internal mixing type injector; (b) – External mixing injector.

The spray mass flow non-uniformity coefficient *K* can be presented as Eq. (3.1) using a sector type spray patterner, where Q_{avg} – mean mass of liquid; Q_{max}, Q_{min} – maximum and minimum mass among the sectors. According to Stochek et al. (1987), Vasilyev et al. (1993), the injector expansion coefficient *C* at $K = 10\%$ is called the critical expansion coefficient C_{cr}.

$$K = \left[\frac{Q_{max}}{Q_{avg}} - \frac{Q_{min}}{Q_{avg}}\right] \times 100\% \tag{3.1}$$

$$C = \frac{2R}{d_c} \tag{3.2}$$

When the critical expansion coefficient is smaller than the injector's expansion coefficient as presented in Eq (3.2) ($C < C_{cr}$), it is called an open swirl injector, and when the critical expansion coefficient is larger ($C > C_{cr}$), it is called a closed type. Usually, if the swirl chamber radius R and the orifice radius r_c are the same, it is called an open type injector. Figure 3.3 shows the variation of the internal mixing dual coaxial injectors. Depending on the combination of closed and open single injectors, they are classified as closed, semi-open and open dual injectors.

The characteristics of the open-type gas injector also depend on the internal dimensions – internal diameter, length of the orifice, the number and size of tangential flow paths. The dimensions of the gas injector used in this paper for the internal mixing type and the external mixing type coaxial injector are the same except thickness of orifice wall.

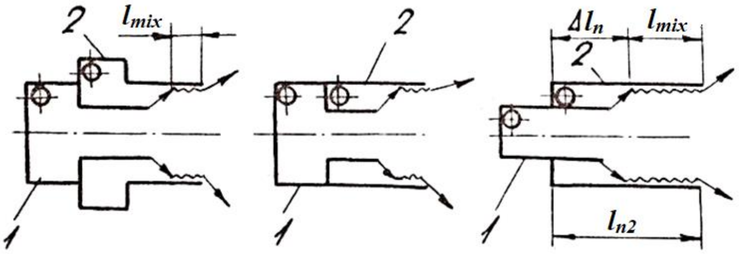

(a) (b) (c)

Figure 3.3 Internal mixing type dual swirl injectors: (a) – closed type, (b) – semi-open type, (c) – open type (1 – inner injector, 2 –outer injector) [Kurpatenkov (1987)].

The recess number RN is defined as the ratio of the recess length (L_r) to the axial distance from the inner injector exit to the impinging point (L_c). This can be expressed as formulae (3.3) and (3.4), where r_{outl} – the inner radius of the liquid jet nozzle; r_{inl} – the inner radius of the gas injector nozzle.

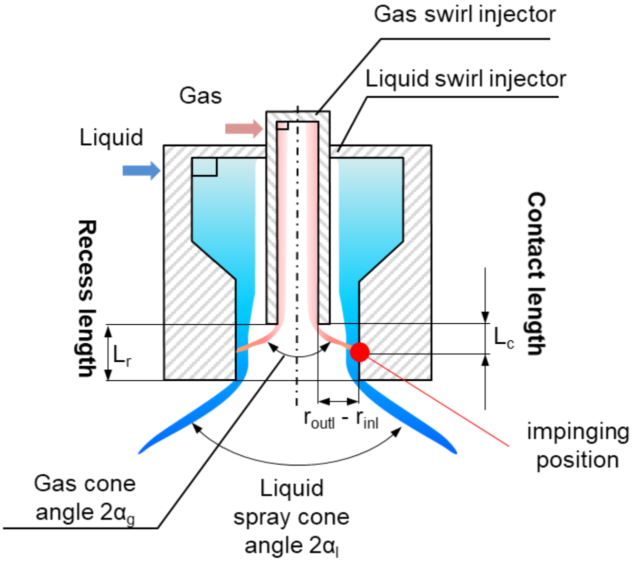

Figure 3.4 Schematic of internal mixing type dual coaxial swirl-swirl injector.

$$RN = \frac{L_r}{L_c} \tag{3.3}$$

$$L_c = \frac{r_{outl} - r_{inl}}{\tan \alpha_g} \tag{3.4}$$

A dual coaxial injector can be classified as the internal mixing type if the beginning point of the oxidizer-fuel interaction is inside the injector nozzle ($L_r \geq L_c$) as shown in Fig. 3.4. The difference between contact length and recess length is called the length of the mixing zone ($L_{mix} = L_r - L_c$). The oxidizer-fuel mixture residence time τ_ϕ in the injector is directly proportional to L_{mix}. It is known that τ_ϕ affects specific impulse, combustion stability, and cooling reliability of liquid rocket engines. *RN* is a parameter related to the gas impingement position on the liquid film in the liquid injector orifice [Arsentiev (1972)]. According to Yang (2008), recess number *RN* also affects atomization characteristics of gas-liquid mixture spray.

Each gas injector used for the internal and external mixing injectors was identical, with eight square inlets (1.5 mm × 2 mm) spaced at equal intervals. The lip thicknesses of the spout wall were $\Delta d_I = 2.99$ mm and $\Delta d_E = 3.59$ mm, respectively. The liquid injectors also had four equal square inlets (1.8 mm × 2.3 mm), but the recess numbers were $RN_I = 1$ and $RN_E = 0$ for the internal and external mixing injectors, respectively. The air from the compressor was controlled by a regulator before pressurizing tanks A and B. In the experiments, water and compressed air were used as the model fluids. The spray conditions used in the experiments are described in Table 3.2.

A simplified Piping & Instrument Diagram of the pressure-fed type liquid rocket engine is shown in the Fig. 3.5.

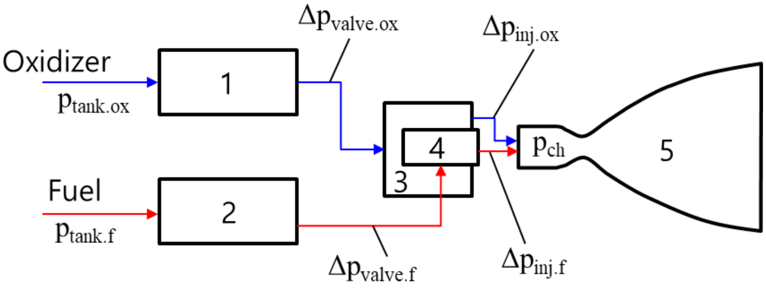

Figure 3.5 Schematic of pressure-fed cycle rocket engine: 1 – oxidizer valve; 2 – fuel valve; 3 – fuel injector; 4 – oxidizer injector; 5 – combustion chamber.

According to Kurpatenkov et al. (1987), it is important to obtain the pressure p_{ch} in the combustion chamber for the major factors (thrust, specific impulse) indicating the operating performance of the combustion chamber and engine. Given the tank pressures $p_{tank.ox}$ and $p_{tank.f}$, the Eqs. (3.5) and (3.6) for calculating p_{ch} can be expressed by the differential pressure and pressure loss of each engine elements.

$$p_{ch} = p_{tank.ox} - \Delta p_{valve.ox} - \Delta p_{inj.ox} \tag{3.5}$$

$$p_{ch} = p_{tank.f} - \Delta p_{valve.f} - \Delta p_{inj.f} \tag{3.6}$$

Andreev (2005) stated that the low frequency instability phenomenon in the combustion chamber of the small liquid rocket engine for RCS is related to the value of $\Delta p_{valve} + \Delta p_{head} + \Delta p_{inj}$. According to Yegorychev (2011), Alpatov (2007), the differential pressure of the injectors was not related to the spray quality and the complete combustion rate of the propellant. It is also known that the propellant flow rate is directly proportional to the differential pressure of the injector. Therefore, in this paper, the injection differential pressure was considered as the reference condition for the experiment. A pressure sensor was installed at the inlet of the injector to measure the differential pressure under normal pressure conditions.

It is known that the breakup in gas–liquid spray is caused by the kinetic energy exchange between the gas and liquid (Orlov, 2001). This is represented by the momentum flux ratio parameter, which is expressed as the ratio between the dynamic pressures of the liquid and gas as shown in Eq. (3.7):

$$J = \frac{\rho_g V_g^2}{\rho_l V_l^2} \tag{3.7}$$

, where $V_l = \sqrt{u_l^2 + w_l^2}$ and $V_g = \sqrt{u_g^2 + w_g^2}$ is the velocity of the liquid and gas. The liquid Weber number can be expressed as Eq. (3.8), where ρ_l is the density of the liquid, μ_l is the viscosity coefficient of the liquid, *h* is the liquid film thickness [Im et al. (2010); Kulkarni et al., (2010)]. The gas Reynolds number can be calculated as shown in Eq. (3.9), where ρ_g is the density of the gas, μ_g is the viscosity of the gas, D_{in} is the inner diameter of the gas injector nozzle outlet:

$$We_l = \frac{\rho_l V_l^2 t}{\sigma_l} \tag{3.8}$$

$$Re_g = \frac{\rho_g V_g D_{in}}{\mu_g} \tag{3.9}$$

Table 3.1. Geometric parameters of injectors.

Geometric Parameter	Value	Unit
a_l	1.80	mm
b_l	2.30	
a_g	1.50	
b_g	2.00	
t_I	2.99	
t_E	3.59	
D_{inI}	10.82	
D_{outI}	18.52	
D_{inE}	10.82	
D_{outE}	18.52	
L_r	4.52	

Rizk & Lefebvre (1985), Kim et al. (2010) suggested the liquid film thickness of swirl injectors as empirical equations (3.10 – 3.12), where t – liquid film thickness; $\dot{m}$ – mass flow rate; μ – viscosity; ρ_l – density of liquid; Δp – pressure drop; l – orifice length; d – orifice diameter.

$$t = 3.66\left(\frac{d\dot{m}_l\mu_l}{\rho_l\Delta p}\right)^{0.25} \tag{3.10}$$

$$t = 2.7\left(\frac{d\dot{m}_l\mu_l}{\rho_l\Delta p}\right)^{0.25} \tag{3.11}$$

$$\frac{t}{d} = 1.44\left(\frac{\dot{m}_l \mu_l}{\rho_l \Delta p d^3}\right)^{0.25}\left(\frac{l}{d}\right)^{0.6} \tag{3.12}$$

Table 3.2. Experimental conditions and parameters.

Simulant	Injection Pressure, MPa	Mass flow rate, g/s	Gas Reynolds number (Re_g)	Liquid Weber number (We_l)	Momentum flux ratio (J)
Gas	0.2	16	0.1×10^6	—	—
	0.4	60	0.5×10^6	—	—
	0.6	131	1.2×10^6	—	—
	0.8	228	1.8×10^6	—	—
	1.0	353	2.8×10^6	—	—
Internal mixing type					
Water	0.2	140	—	284	0.26 -147
	0.4	203	—	592	
	0.6	257	—	1060	
	0.8	297	—	1381	
	1.0	337	—	1777	
External mixing type					
Water	0.2	133	—	378	0.18 -97
	0.4	194	—	805	
	0.6	240	—	1205	
	0.8	280	—	1607	
	1.0	321	—	2034	

In the injector of this chapter, however, the thickness of the liquid film was measured by analyzing the images (see Fig. 3.6) obtained using a light source (HVC-SL, Photron) and a transparent injector. Distorted part at the injector exit appears due to the refraction of light. So, the thickness was measured 1.5 mm over the exit. According to the graph shown in Figure 3.7, when only the liquid passes through the injector, the amplitude variation of the liquid film thickness is not significant.

Therefore, the average value of the oscillating thickness was used when only liquid was sprayed.

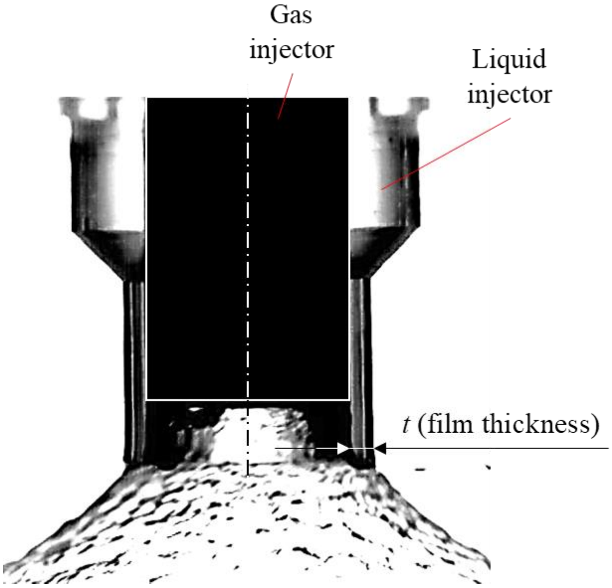

Figure 3.6 Liquid film in a transparent injector (liquid differential pressure Δp_l = 2bar, gas differential pressure Δp_g = 6bar).

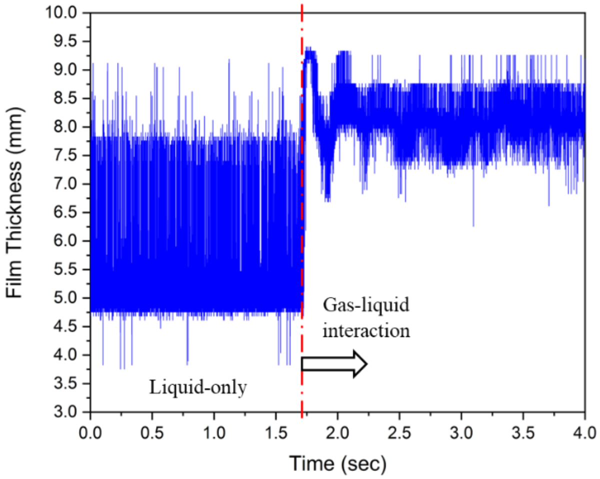

Figure 3.7 Variation of liquid film thickness over time (liquid differential pressure Δp_l = 2 bar, gas differential pressure Δp_g = 6 bar).

3.2 Spray Pattern and Gas-liquid Spray Angle of Internal and External Mixing Type Injectors

The spray forms of the internal mixing type and external mixing type injector according to the supply conditions are shown in Fig. 3.8. Both types of spray appear seemingly similar. It is similar to the spray form of a general simplex swirl injector when the flow rate of gas and liquid have low value. According to Clark and Dombrowski (1972), the liquid film becomes unstable in the form of waves when the liquid film moves in a stationary gas medium. During the vibration process caused by the aerodynamic force and the surface tension of the liquid, the portion whose thickness is locally reduced can be easily torn. These perforations were observed around the liquid ligament and appeared at the top of the spray cone in the form of horizontal stripes.

The region where the liquid film or ligament was observed decreased significantly, and 'droplet cloud' appeared as the gas flow rate increased. The generation of fine droplets by gas flow can be found in the coaxial shear type injector. Because the rotational speed was imposed on the gas, the pattern was slightly different in this study. As the gas-liquid volume flow rate ratio (GLR) increased, the boundary line of the spray cone tended to be blurred. It can be seen that the liquid flow is severely disturbed as the gas turbulence completely destroys the liquid film. However, according to image $I-g$ (Fig. 3.8), the size of the droplets distributed on the outside and the scale of the droplets on the inside of the spray were different. In particular, it was observed that a mist-like zone was formed at the center of the spray. It is apparent that this phenomenon is caused by gas flow, since a rotating gas turbulence is emitted from the central injector, and it is more clearly visible under the condition of a large gas flow rate.

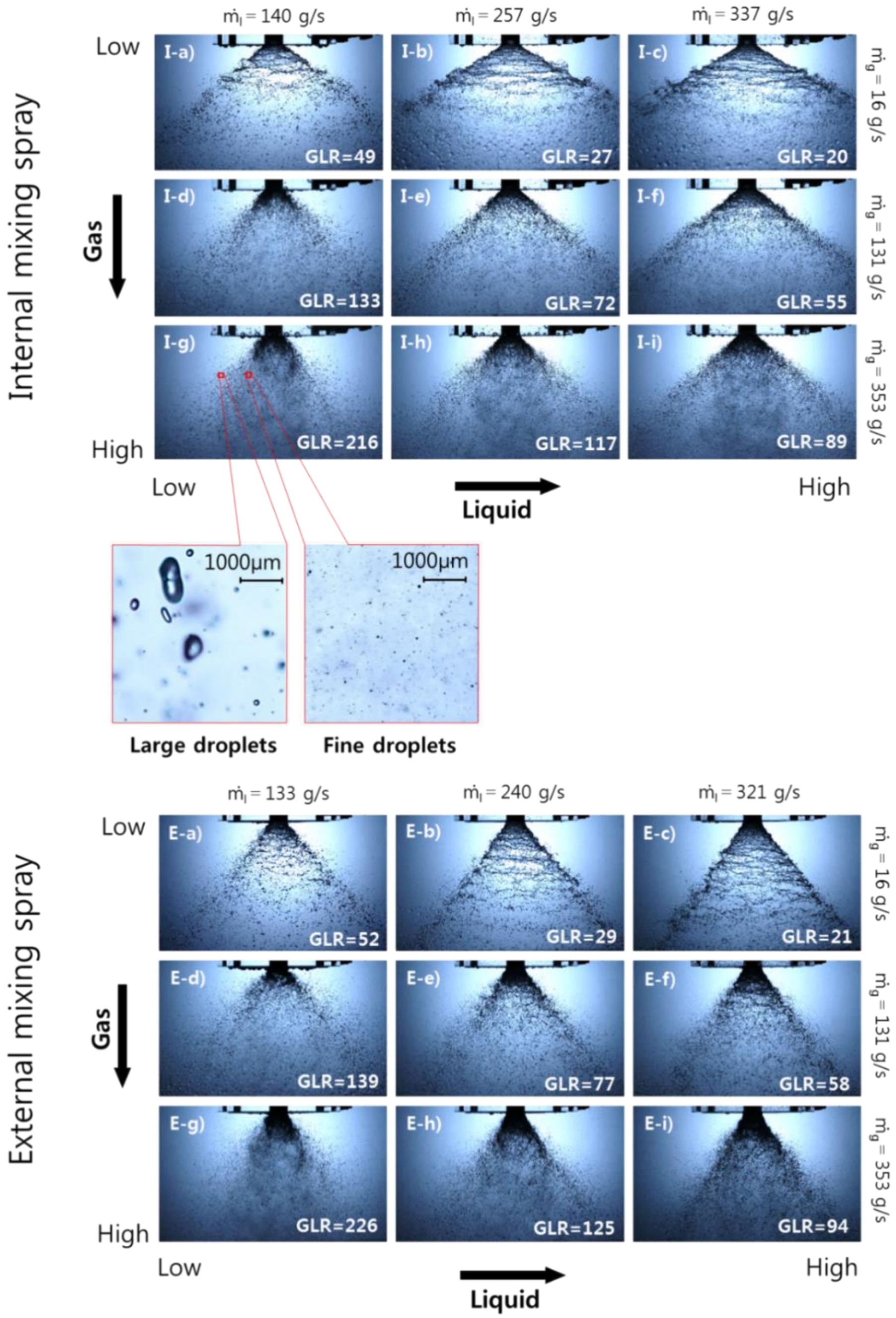

Figure 3.8 Gas-liquid spray pattern of internal and external mixing types [Jeong et al. (2020)].

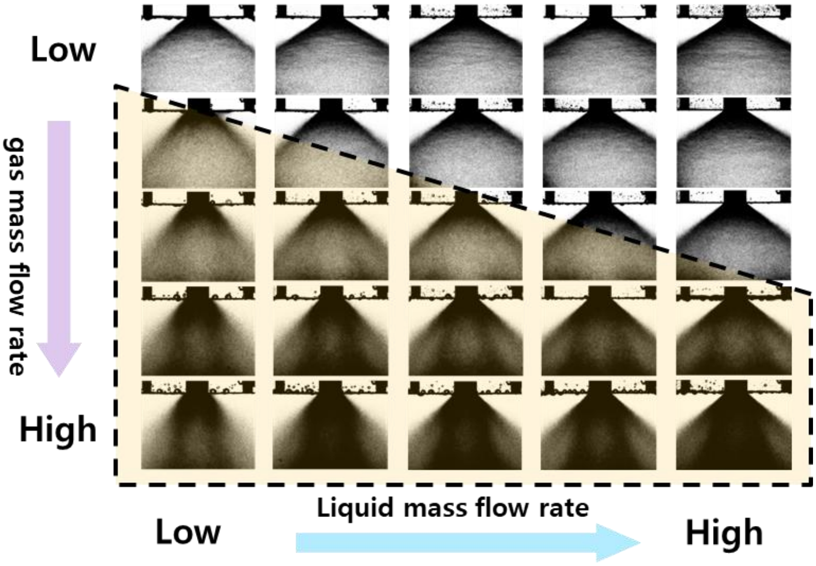

(a)

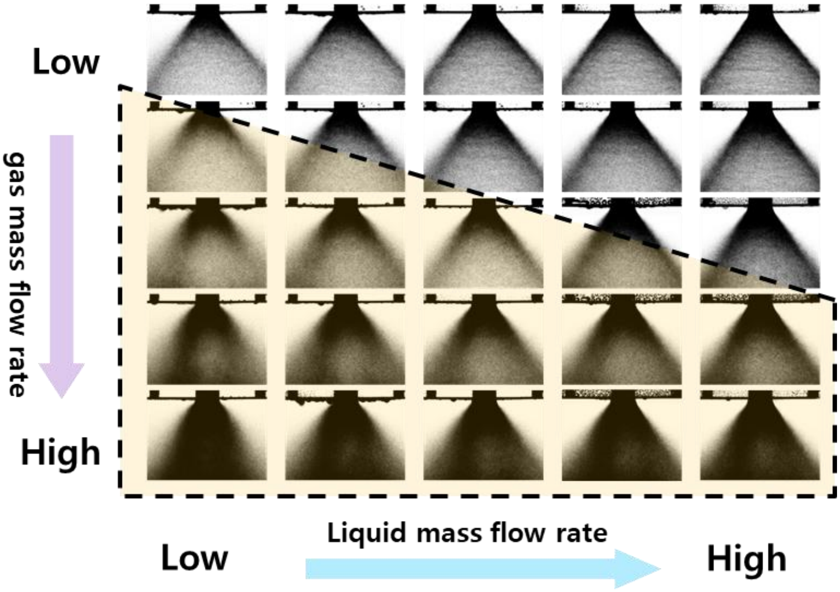

(b)

Figure 3.9 Cumulated-binarized spray image of (a) internal mixing type, (b) external mixing type.

However, since the spray is not fixed over time and the droplets move with their own speed, it was judged that it was too early to be sure of the mist-like region in individual images. So, after binarizing 100 spray images taken with a digital camera, a cumulative average image was created and presented in Fig. 3.9. In Fig. 3.9 (a) and (b), it was confirmed once again that a dark part distinguished from the existing spray pattern appeared in the lower right condition, respectively. It is judged that the dark part corresponds to the mist-area. In particular, there was a tendency for dark areas to be independently distinguished within the internal mixing spray. In the external mixing spray, it is difficult to determine whether these dark areas are independent as its spray angle is relatively small.

The wall thickness of the gas injector was not so thick that the gas flow did not affect the liquid atomization. Therefore, the gas could begin to affect the liquid immediately after exiting the injector outlet. In addition, since the internal mixing injector had a mixing zone, it was natural that the interaction already occurred from inside the injector. In the spray image taken with the camera, the area adjacent to the injector exit partially blocked the path of light from the light source due to the presence of a liquid film and a liquid, and the large amount of small droplets blocked the light incident on the camera lens. Therefore, it is difficult to obtain information about the formation of droplets in the area adjacent to the injector exit from the snapshot image.

The spray cross section was taken by changing the liquid flow rate under the condition of a large gas flow rate ($\mathrm{Re}_g = 2.77 \times 10^6$) using planar laser. In Figs 3.10 and 3.12, the images were normalized based on the lowest luminance (i.e., 0) (Kim et al., 2020). As shown in Fig. 3.5, a blue area with a relative intensity value from 0.1 to 0.3 developed generally vertically below the injector outlet. Since the green part with a relative intensity of 0.4~0.7 occurs partially above the top of the spray cone, it can be estimated that the gas and liquid interact violently. In Fig 3.10(a), the droplet area and the blue area have overlapping forms, and the interaction area is also distributed in the vertical direction. In Fig 3.10 (b), the blue area was separated from the droplet area. As shown in Fig 3.10(c), the distribution of the interaction zones in a diagonal direction could be seen as a decrease in the ability of gas flow to penetrate the liquid film as the liquid Weber number increased. In Fig. 3.10(d), the blue area and the outer droplet distribution area were independent of each other, but the range of the interaction area was somewhat reduced. The reason for this phenomenon was that the effect of the gas flow on the liquid film decreased, and rather, the gas flow slid down along the liquid film. In Fig. 3.10(e), considering that the green area has decreased considerably, it is most reasonable to judge that the liquid film penetration capacity of gas has decreased significantly as the liquid Weber number increased.

Since the Mie signal tends to increase as the diameter of the droplet increases, it can be considered that the size of the droplet increases as the relative intensity increases. In Fig 3.11(a), a high intensity close to 1 was found in a narrow area at the top of the cone, and the areas where large and fine droplets were scattered were overlapped. In Fig 3.11(b), it can be seen that the high-intensity zone was separated and the flow toward the center was created. As it changed from Fig 3.11(c) to Fig 3.11(d) (as Weber number increases), the masses with high intensity values were distributed diagonally.

The images of the longitudinal section of the external mixing spray are presented in Figs 3.12 and 3.13. In Figs 3.12(a) and (b), a blue area has already been found from the injector exit. The inertia of the liquid is weak enough to be easily caught in the gas stream at low Weber number conditions. Therefore, it means that gas collision occurred outside the injector, but the droplets bounced in all directions. In (c), (d), and (e), the blue areas were diagonally distributed, in contrast to the internal mixing spray. In Fig. 3.12, points with intensity close to 1 were generated diagonally downward at regular intervals. In Fig 3.13, fine droplets were found between these peaks. In Fig. 3.13 (a), the size of the clusters of high intensity and the distance between each cluster were rather large. However, the number of clusters tended to increase as the Weber number increases.

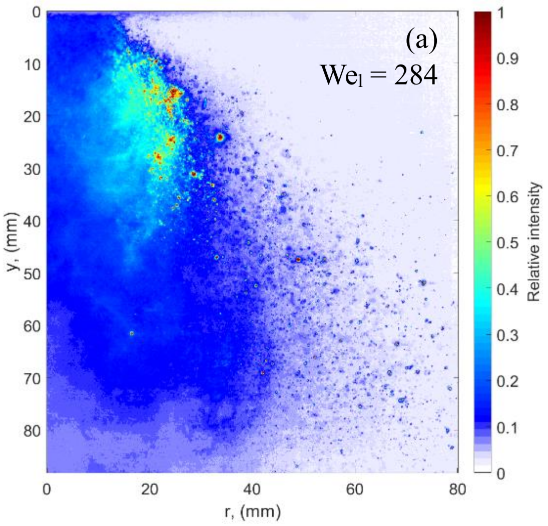

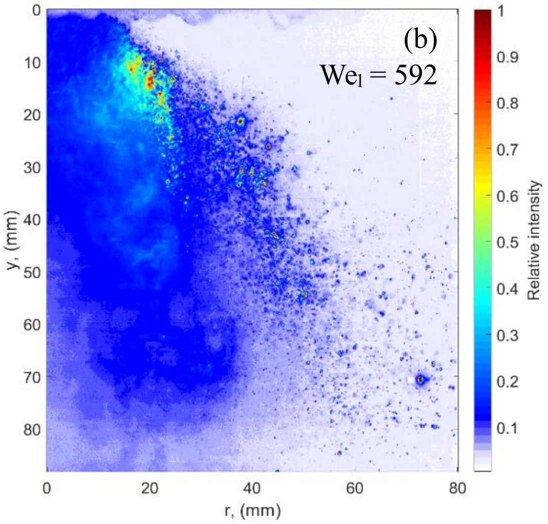

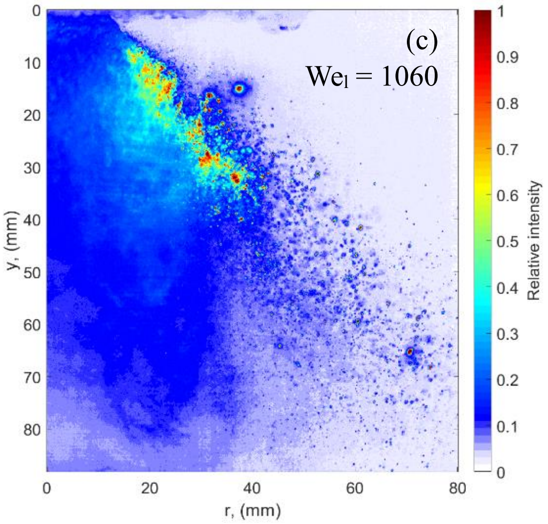
(c)
We$_l$ = 1060
y, (mm)
r, (mm)
0
10
20
30
40
50
60
70
80
0
20
40
60
80
Relative intensity
1
0.9
0.8
0.7
0.6
0.5
0.4
0.3
0.2
0.1
0

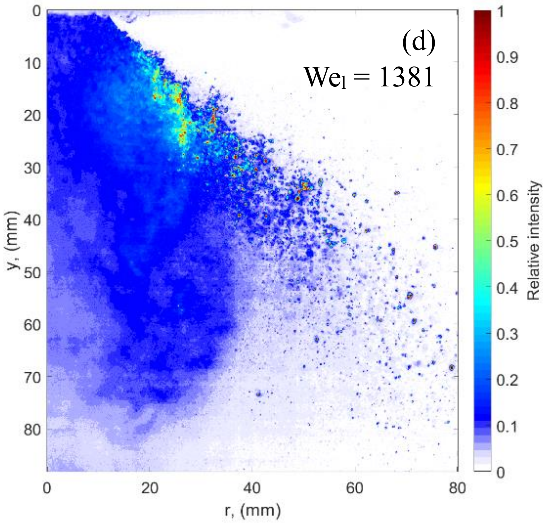
(d)
We$_l$ = 1381
y, (mm)
r, (mm)
0
10
20
30
40
50
60
70
80
0
20
40
60
80
Relative intensity
1
0.9
0.8
0.7
0.6
0.5
0.4
0.3
0.2
0.1
0

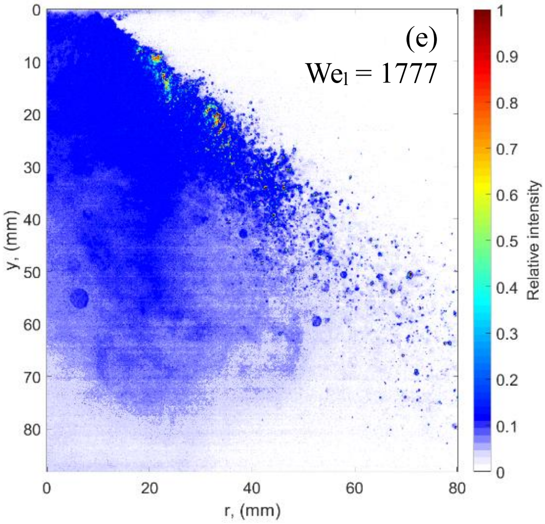

Figure 3.10 Internal mixing spray images of longitudinal section before applying SLIPI technique ($Re_g = 2.77 \times 10^6$).

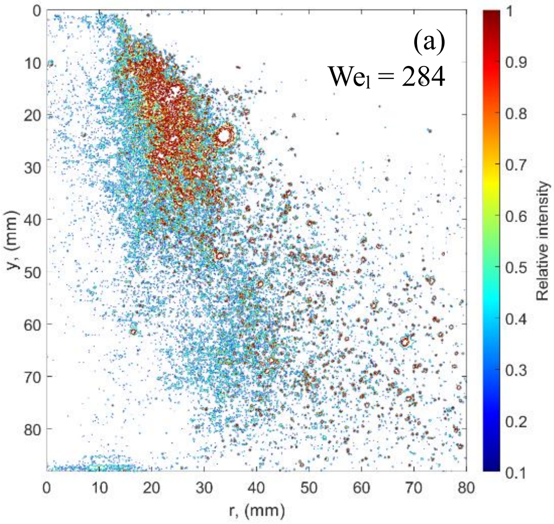

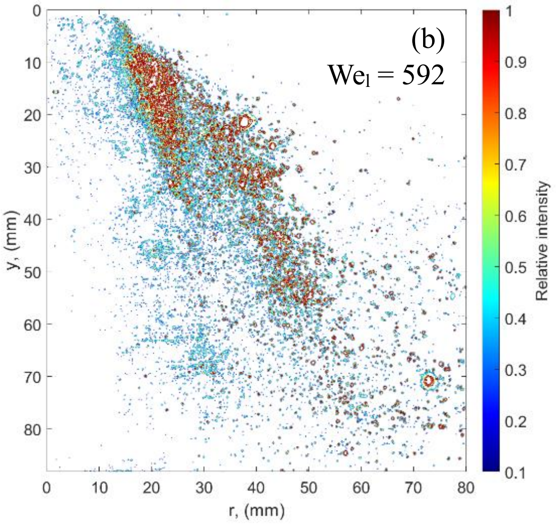
(b)
We$_l$ = 592
y, (mm)
r, (mm)
0
10
20
30
40
50
60
70
80
Relative intensity
0.1
0.2
0.3
0.4
0.5
0.6
0.7
0.8
0.9
1

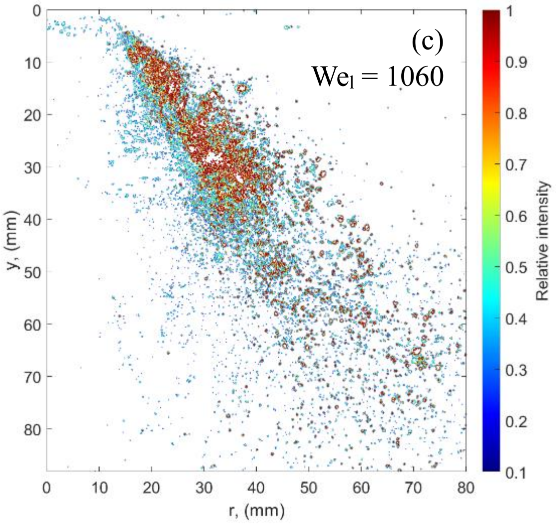
(c)
We$_l$ = 1060
y, (mm)
r, (mm)
0
10
20
30
40
50
60
70
80
Relative intensity
0.1
0.2
0.3
0.4
0.5
0.6
0.7
0.8
0.9
1

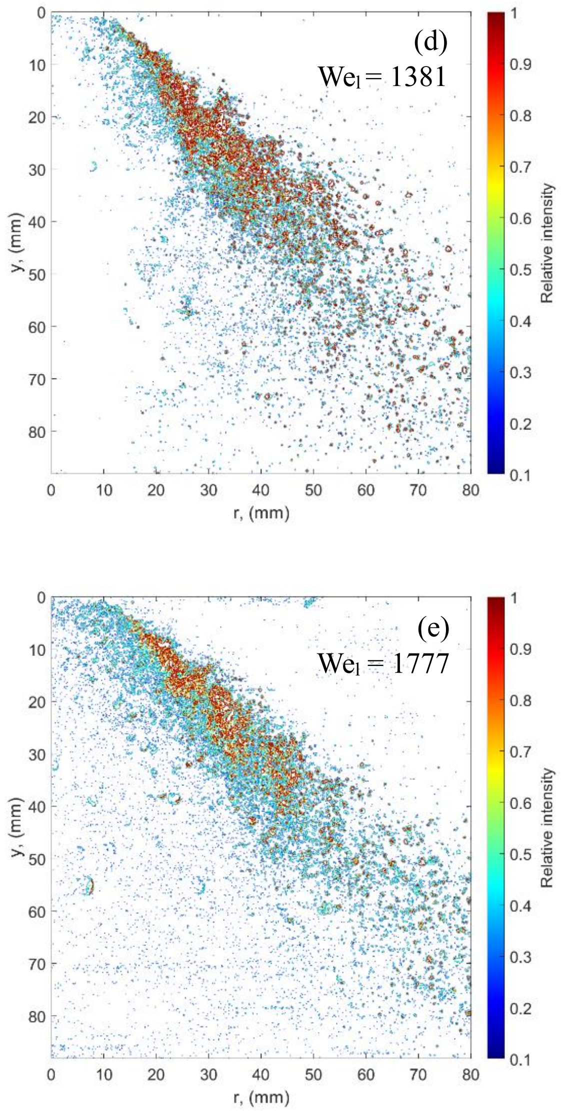

Figure 3.11 Internal mixing spray images of longitudinal section after postprocessing by SLIPI technique ($Re_g = 2.77 \times 10^6$).

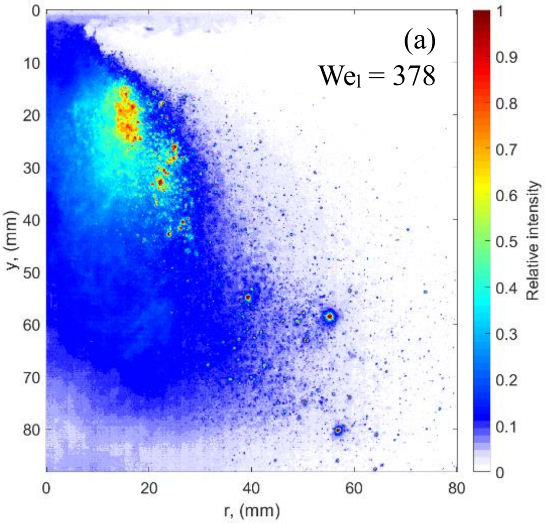
(a)
$We_l = 378$
y, (mm)
0
10
20
30
40
50
60
70
80
r, (mm)
0
20
40
60
80
Relative intensity
0
0.1
0.2
0.3
0.4
0.5
0.6
0.7
0.8
0.9
1

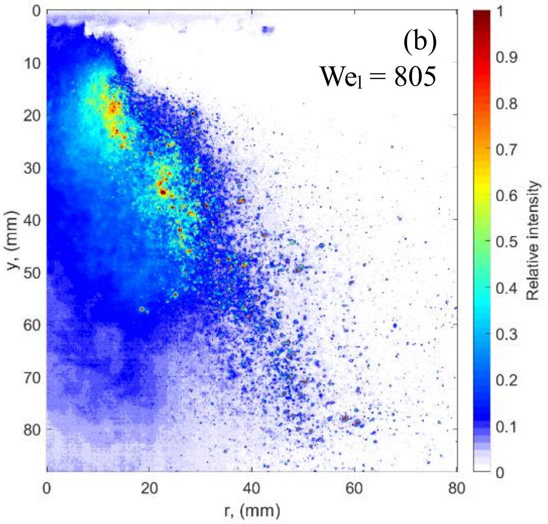
(b)
$We_l = 805$
y, (mm)
0
10
20
30
40
50
60
70
80
r, (mm)
0
20
40
60
80
Relative intensity
0
0.1
0.2
0.3
0.4
0.5
0.6
0.7
0.8
0.9
1

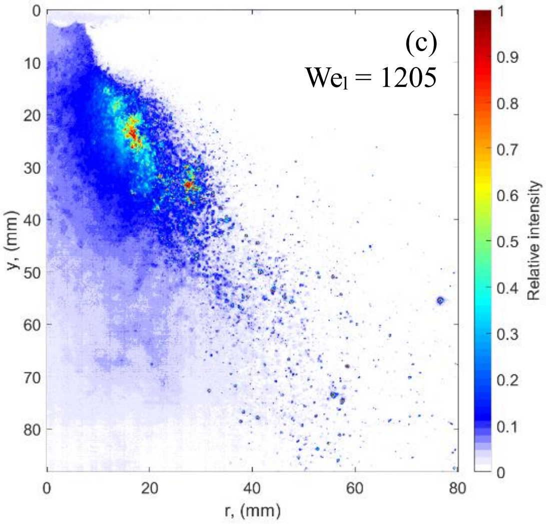
(c)
$We_l = 1205$
y, (mm)
0
10
20
30
40
50
60
70
80
r, (mm)
0
20
40
60
80
Relative intensity
0
0.1
0.2
0.3
0.4
0.5
0.6
0.7
0.8
0.9
1

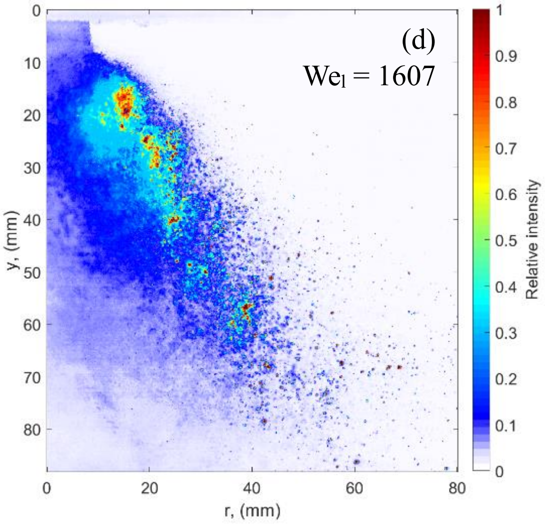
(d)
$We_l = 1607$
y, (mm)
0
10
20
30
40
50
60
70
80
r, (mm)
0
20
40
60
80
Relative intensity
0
0.1
0.2
0.3
0.4
0.5
0.6
0.7
0.8
0.9
1

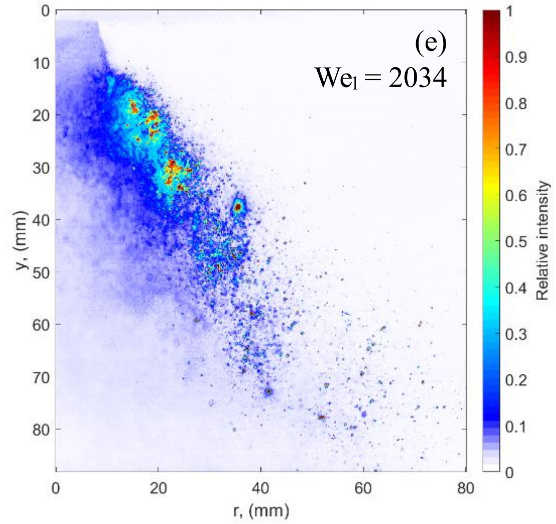

Figure 3.12 External mixing spray images of longitudinal section before applying SLIPI technique ($Re_g = 2.77 \times 10^6$).

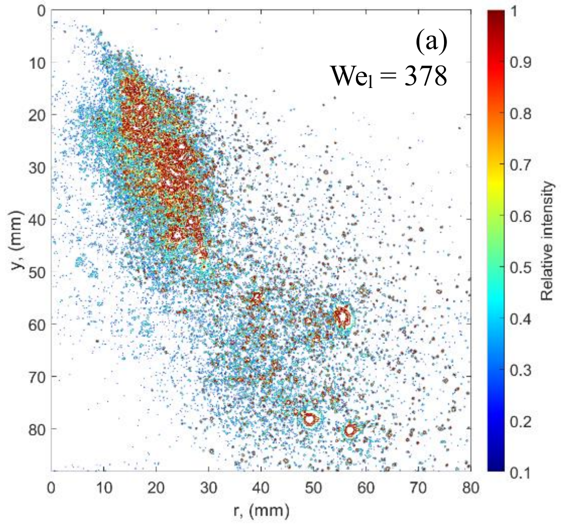

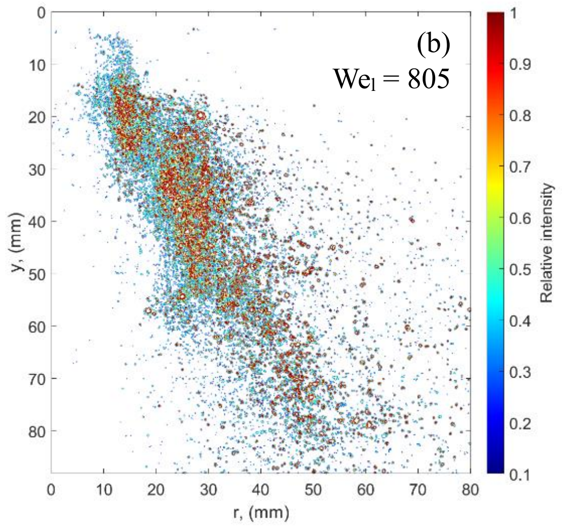
(b)
We$_l$ = 805
y, (mm)
r, (mm)
Relative intensity
0
10
20
30
40
50
60
70
80
0.1
0.2
0.3
0.4
0.5
0.6
0.7
0.8
0.9
1

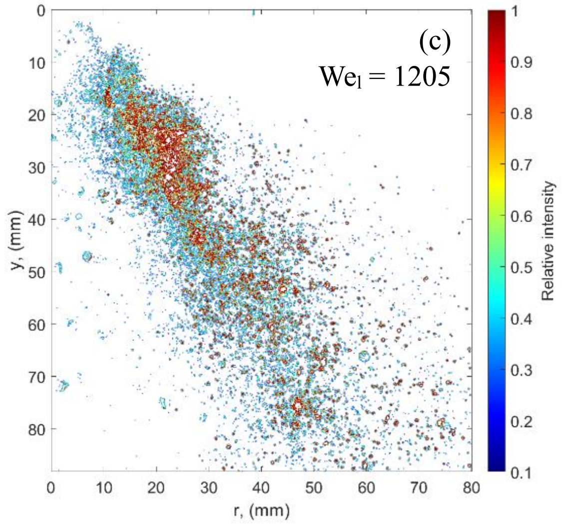
(c)
We$_l$ = 1205
y, (mm)
r, (mm)
Relative intensity
0
10
20
30
40
50
60
70
80
0.1
0.2
0.3
0.4
0.5
0.6
0.7
0.8
0.9
1

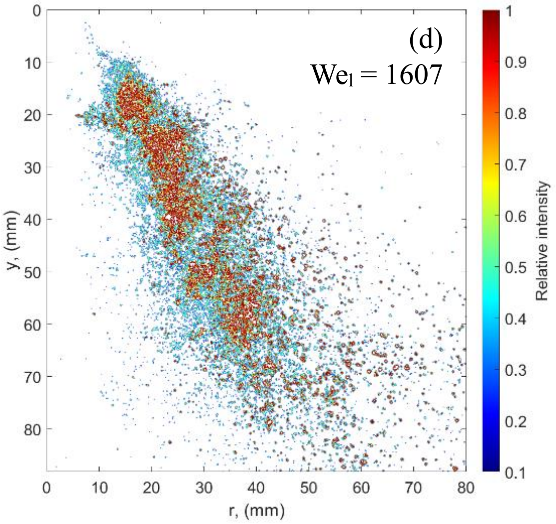

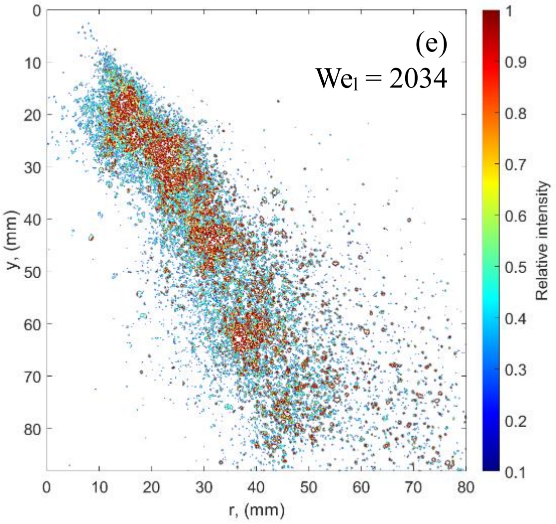

Figure 3.13 External mixing spray images of longitudinal section after postprocessing by SLIPI technique ($Re_g = 2.77 \times 10^6$).

The difference between these two spray types means that the effect of the gas on the liquid film is different. It is thought that, the gas flow scrapes the inside of the liquid film in the case of the internal mixing type spray, while the external mixing type collides with the liquid film and bursts it.

In the external mixed spray, the collision of gas flow on the liquid film has periodicity. Under the conditions with the most clusters (We_l = 2034), images were arranged continuously with a time interval of 1.143 ms (see Fig. 3.14). In the continuous SLIPI image, the droplet cluster nodes are arranged at intervals of about 10-20 mm. Here, the peak point on the image showed a tendency to move downwardly, and it was confirmed that a new peak was generated near the injector outlet. Therefore, it can be said that this phenomenon is not caused by simultaneous shocks caused by gas turbulence, but because the gas periodically affects the upper part of the spray cone.

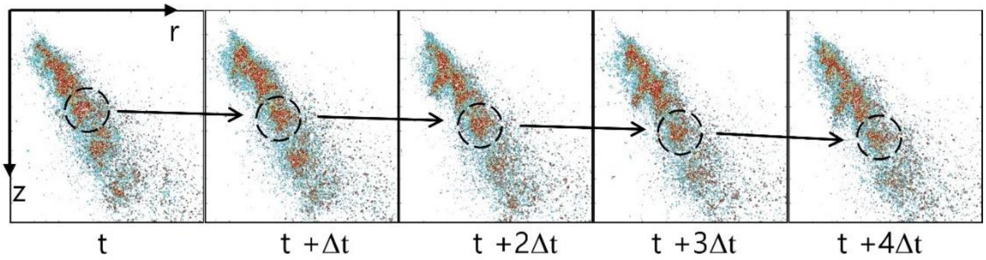

Figure 3.14 Consecutive post-processed image of external mixing type (Δt = 1.143 ms, We_l = 2034, $Re_g = 2.77 \times 10^6$).

Figure 3.15 shows the sum of the pixel intensity ($\bar{N}$ values) of each row on the z-axis of an externally mixed spray image processed after $\bar{N}$ with a time interval of $\Delta t = 1.143$ ms. Three high peaks (A, B, C) appeared at the initial time $t + \Delta t$ and had low values at the downstream position. The distance between the peaks was about 10-20 mm, but the size was not constant. As time passed, the peak position moved in the z-axis direction and the $\bar{N}$ value decreased slightly, but the shape of the peak was maintained. A new peak (D) occurred near the injector nozzle at time $t + 3\Delta t$. Thus, it can be said that the gas flow collides to create droplets in the liquid film outside the injector outlet at certain time intervals.

The z-axis extension range of the mist zone was investigated through binarization of the spray cross-section image without removing multiple scattering. Since both types of spray have a distribution range in the axial direction, the distribution in the z-axis direction was measured for uniformity of measurement. An eccentric point with $r = 9mm$ was chosen as measuring point since there is very little liquid droplet on the injector axis (see Fig. 3.16). The intensity of the image pixels was normalized, the darkest part was set to 0, and the brightest part was set to 1. Intensities obtained from 5000 images were averaged.

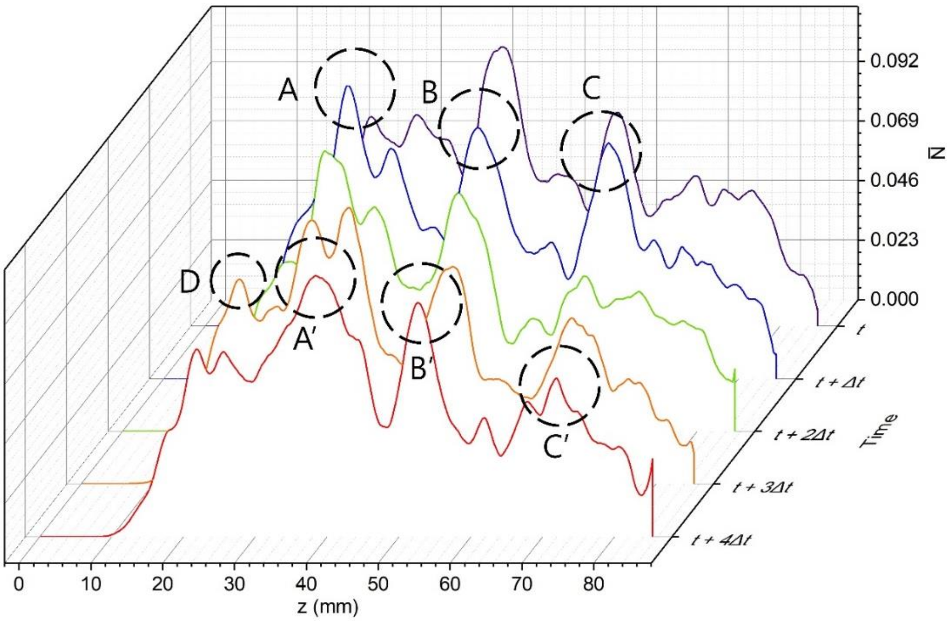

Figure 3.15 Peak position of external mixing type spray ($\Delta t = 1.143$ ms, $We_l = 2034$, $Re_g = 2.77 \times 10^6$).

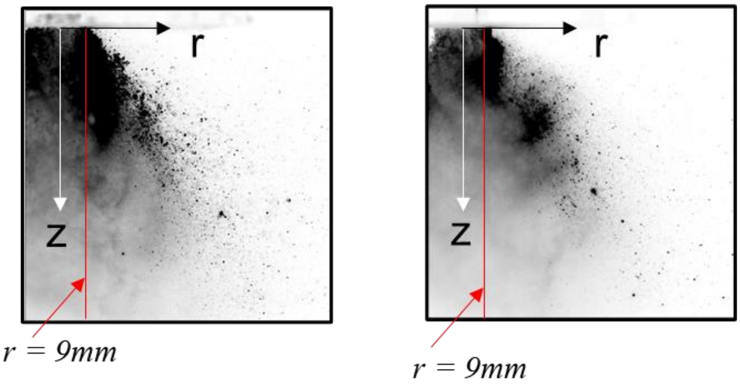

(a) (b)

Figure 3.16 Measurement position for the mist zone range of (a) internal mixing type and (b) external mixing type spray.

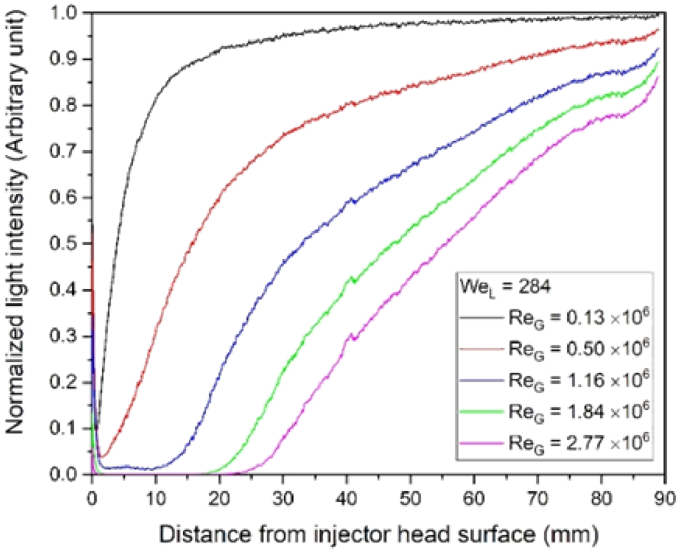

(a)

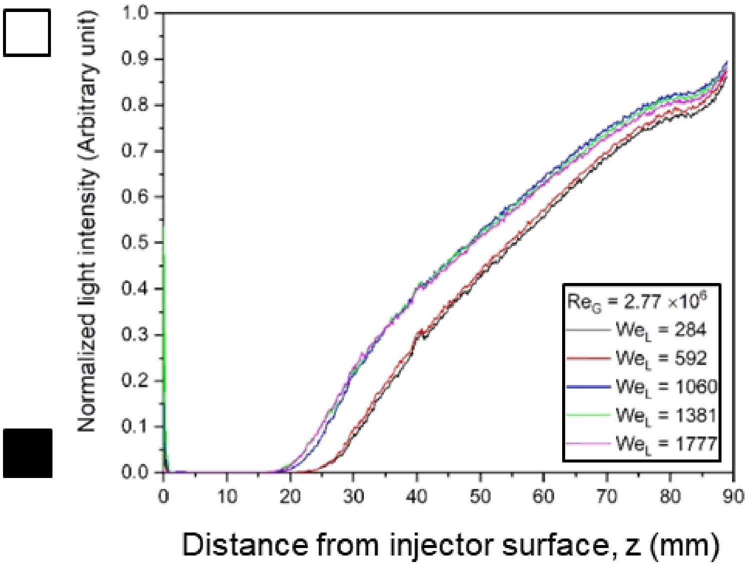

(b)

Figure 3.17 Normalized liquid intensity of internal mixing type spray images with (a) constant liquid Weber number and (b) constant gas Reynolds number.

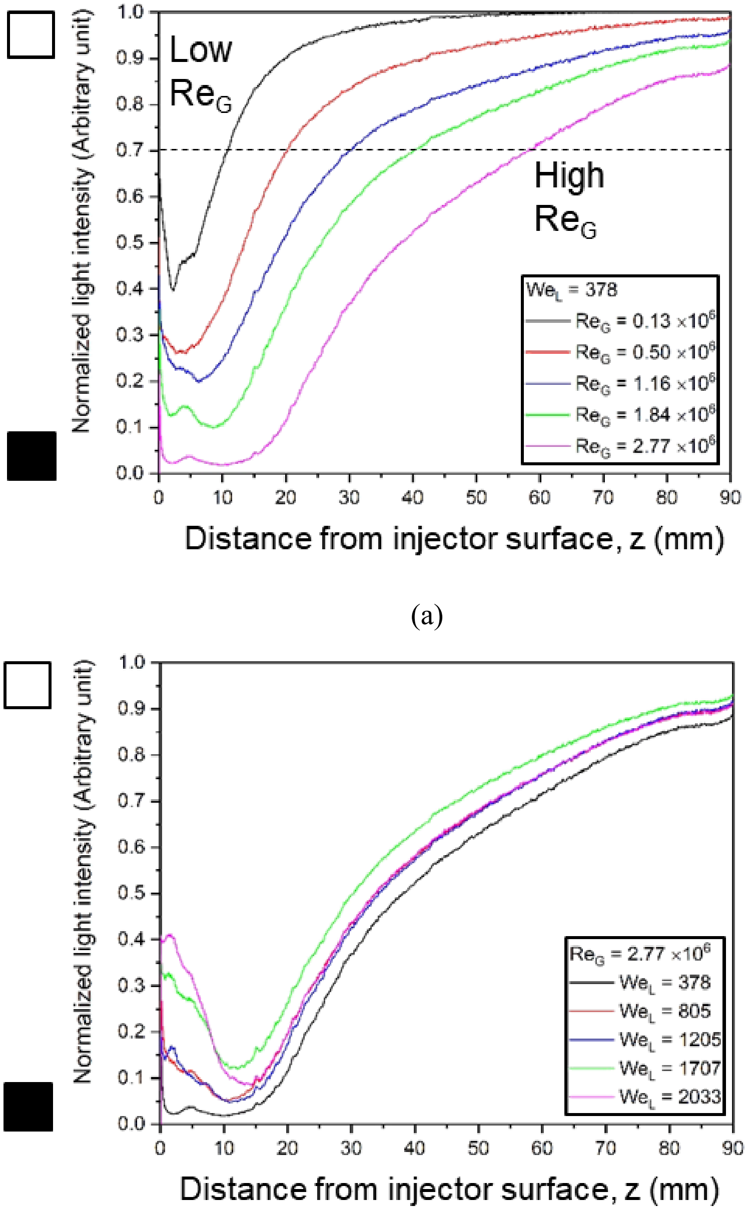

(a)

(b)

Figure 3.18 Normalized liquid intensity of external mixing type spray images with (a) constant liquid Weber number and (b) constant gas Reynolds number.

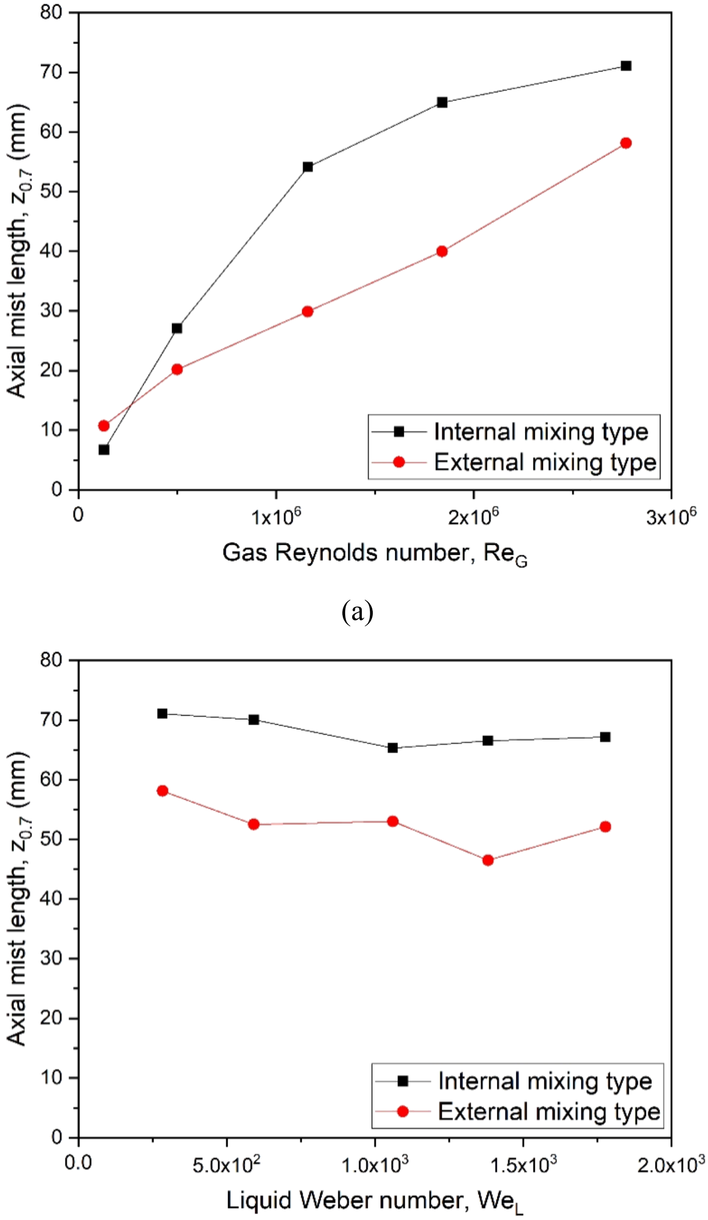

(a)

(b)

Figure 3.19 Virtual axial mist length (reference value 0.7) (a) constant liquid Weber number and (b) constant gas Reynolds number.

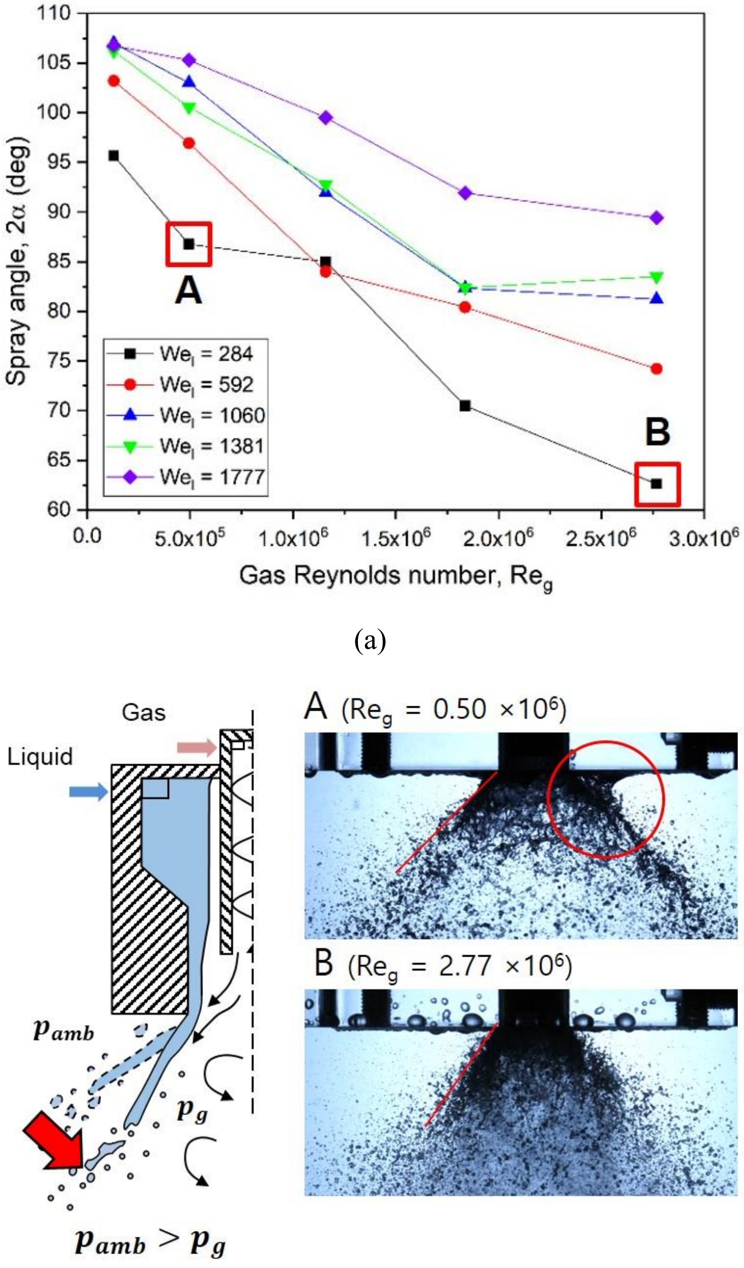

(a)

(b)

Figure 3.20 (a) Spray angle of internal mixing type according to gas Reynolds number (Re_g) and (b) decrease of gas-centered spray [Jeong et al. (2020)].

In Figs 3.17 and 3.18, the intensity of the internal and external mixing spray images are presented, respectively. Both types were somewhat different, but the larger the gas Reynolds value, the larger the axial position reaching the comparable random intensity value. The range hardly changed according to the change of the liquid Weber number.

The axial distance to reach the normalized intensity value of 0.7 increased as the gas Reynolds number increased [Figure 3.19(a)]. However, the fluctuation was insignificant depending on the liquid Weber number [Figure 3.19(b)]. In other words, it can be said that the mist range is dependent on the gas Reynolds number in the internal and external mixing type spraying, and the range of the mist area is related to the gas injection.

The distribution of droplets in the axial and radial directions in the combustion chamber of a liquid rocket engine affects the combustion efficiency. The residence time of the droplets should be longer than the time required for the decomposition, mixing, evaporation and combustion processes. It is known that the travel distance and residence time of the propellant droplets are highly dependent on the injection angle (Yang et al., 2004).

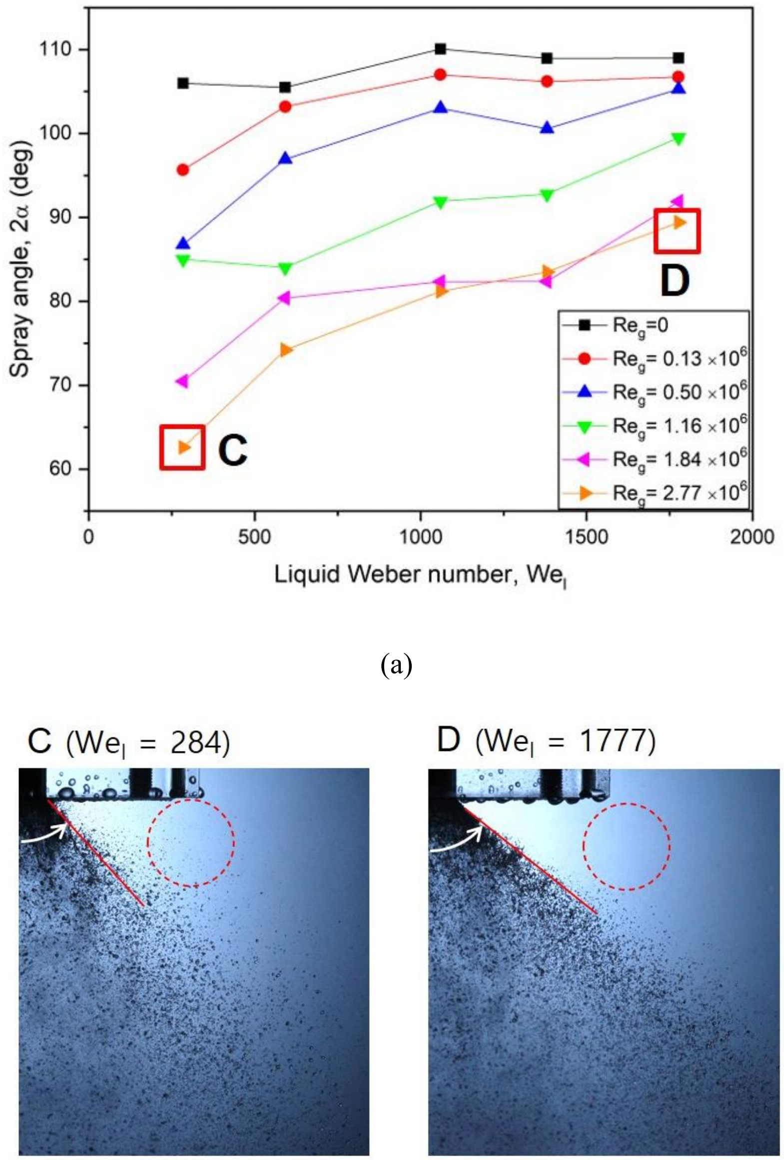

(a)

(b)

Figure 3.21 (a) Spray angle of internal mixing type according to liquid Weber number (We_l) and (b) spray images of the cases *C* and *D* [Jeong et al. (2020)].

In the internal mixing type injector, spray angle decreased as gas Reynolds number increased [Fig. 3.20(a)]. In the left image of Fig 3.20(b), the spray angle of case *B* seems to be smaller than that of case *A*. Since the liquid Weber numbers for cases *A* and *B* are constant, it is clear that this phenomenon is only dependent on changes in the aerodynamic parameters of the gas flow. According to Im et al (2010), the pressure decreases by increasing the velocity of the central gas jet in a spray of GCSC injector. The high-velocity gas flow attracts the gas of the interspace adjacent to the inner surface of the liquid film, and the pressure (p_g) also decreases. At this time, the spray angle of the liquid film decreased since the pressure of the ambient gas (p_{amb}) was relatively larger than p_g. The rotating and translational gas flow had a radial velocity vector component, but the liquid film could not be pushed out directly due to the wall of the recessed region inside the injector. Since the spray consists of droplets and ligaments, the droplets inside the spray cone were entrained to the center and broken up more finely. This is confirmed in the case *B* image that the center of the spray is filled with fine droplets. In case *A*, where the entrainment effect is weakened, the liquid film uplifted, and the liquid drops splashed on the injector wall.

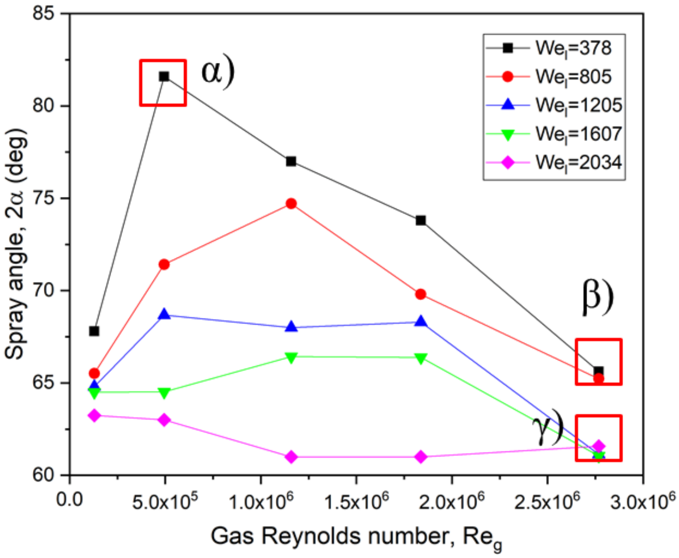

(a)

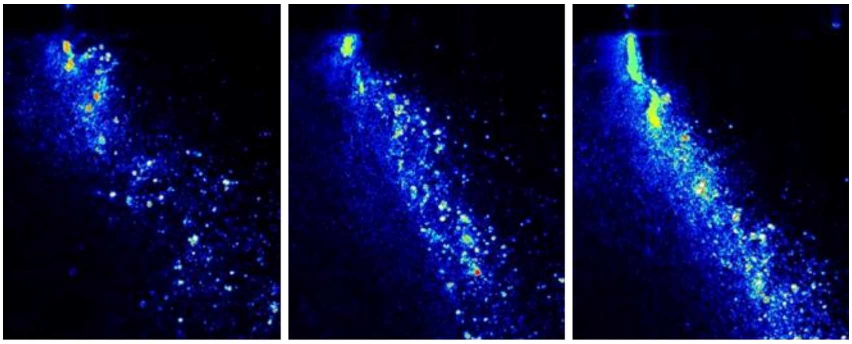

(α) (β) (γ)

(b)

Figure 3.22 (a) Spray angle of external mixing type according to gas Reynolds number (Re_l) and (b) spray images of the cases α, β and γ (α – $We_l = 378$, $Re_g = 4.95 \times 10^5$; β – $We_l = 378$, $Re_g = 2.77 \times 10^6$; γ – $We_l = 2034$, $Re_g = 2.77 \times 10^6$) [Jeong et al. (2020)].

Since the spray angle is directly proportional to the injection pressure, the swirl injector increased as the Weber number increased [Fig. 3.21 (a)]. This is similar to the characteristics of a simplex swirl injector. As in Case *C*, the gas permeates the liquid film and scatters the liquid region, at a low liquid Weber number. So, it was observed that small droplets scattered above the spray cone [Fig 3.21 (b)]. In contrast, the increase in the inertial force of the liquid led to the formation of a rigid spray boundary in case *D* [Fig 3.21 (b)]. The spray angle increasing rate increased, because droplets are more easily swept to the center as the gas Reynolds number increased.

In the external mixing spray, the spray angle increased and then decreased as the gas Reynolds number increased. According to Azzopardi (1997), the droplets swell into a bag shape when the liquid Weber number is lower than that of the gas Reynolds number. A similar phenomenon was also seen in (α). The reason for the increase in the spray angle here is that the gas lifted the liquid film to inflate, and then the droplets were scattered outside the cone. According to the images (β) and (γ) in Fig 3.22 (b), it can be seen that this phenomenon decreased regardless of the liquid Weber number at high gas Reynolds number. According to Fig 3.22 (a), when the liquid Weber number decreased, the spray angle increasing and decreasing rate decreased. This can be explained by the fact that the gas flow could not push the liquid film well because the liquid flow became rigid.

As shown in Figure 3.23, the spray angle generally decreased as the liquid Weber number increased. This decreasing trend was still seen even when no gas was released from the central injector ($Re_g = 0$). That is, it can be said that the rotational speed significantly decreased as the flow rate of the liquid increased. For mixing process outside the nozzle outlet, gas injector wall invaded the liquid film in the liquid injector nozzle. As the lip thickness (t_{lip}) increases, the hydrodynamic resistance of the liquid may increase by interaction with the inner wall of the injector.

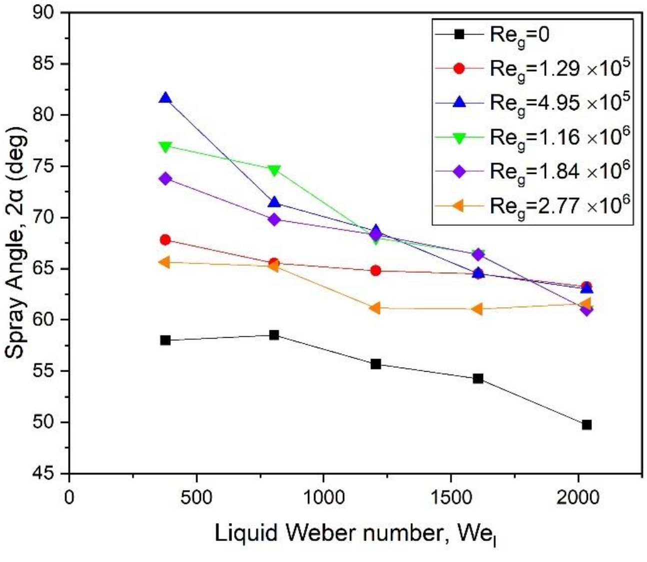

Figure 3.23 Spray angle of external mixing type according to liquid Weber number (We_l).

A simplex liquid swirl injector with a solid cylinder in the inner center as shown in Figure 3.24(a). If there was no object in the center, the spray angle increased by increasing the centrifugal force when the liquid differential pressure increased. The spray angle slightly increased at the beginning as the lip thickness increased (with the d_g fixed). However, when the liquid film was completely invaded by the lip, the spray angle rapidly decreased. According to Figure 3.24(b), when the lip thickness was large, the spray angle decreased as the liquid differential pressure increased. This can be explained by the fact that the rotational motion of the liquid film is prevented by the solid wall. Here, in the case of internal mixing spray (t_{lip} = 2.99mm, RN = 1), the spray angle increase rate has a positive value. This can be considered that the rotational velocity of the liquid film is restored again in the recessed region.

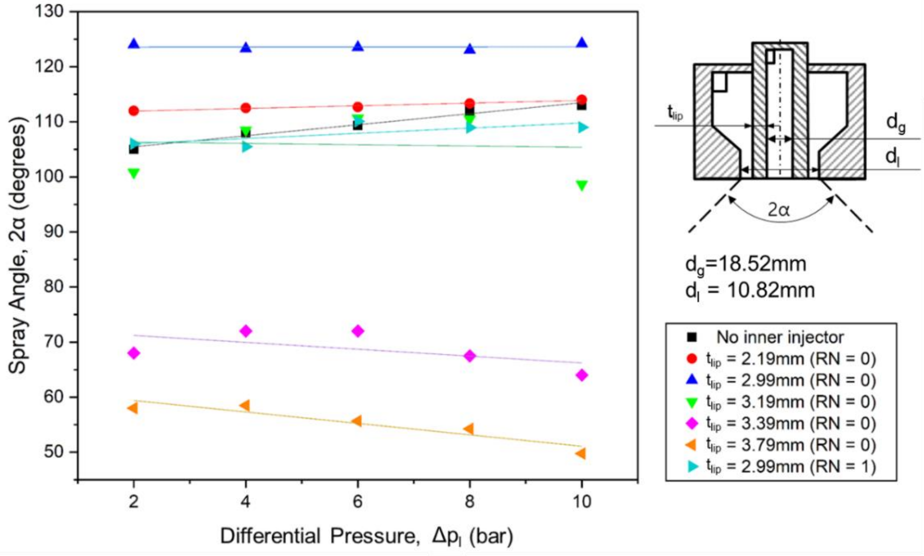

(a)

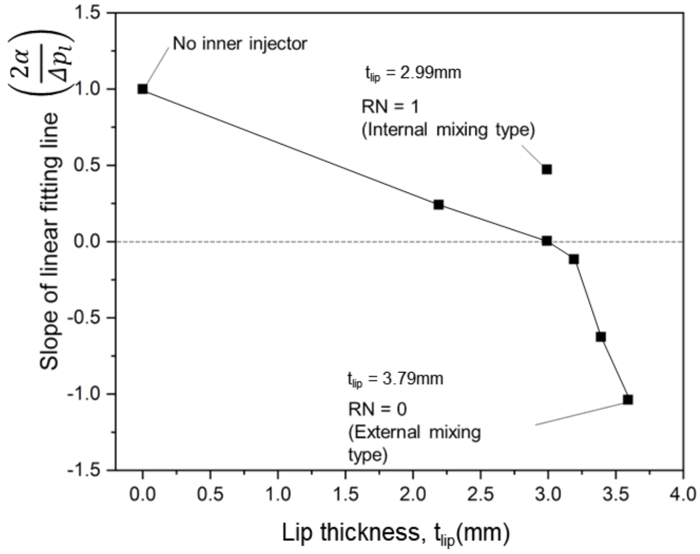

(b)

Figure 3.24 (a) Spray angle without gas flow and (b) fitting line slope of spray angle by increasing differential pressure of liquid.

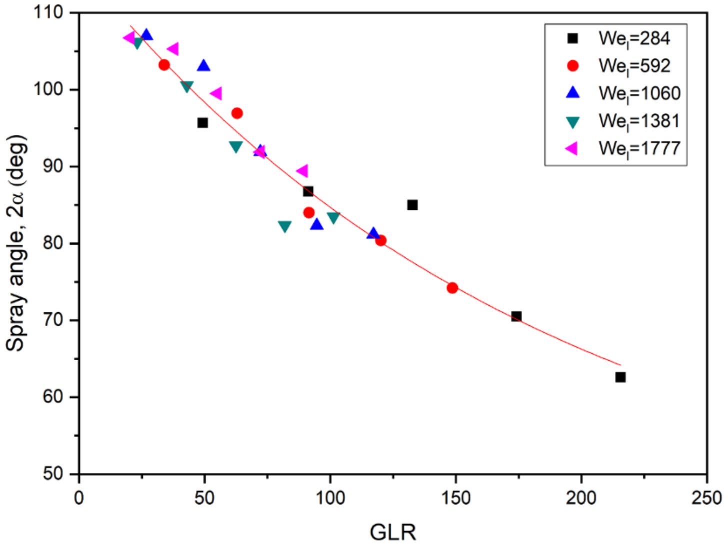

(a)

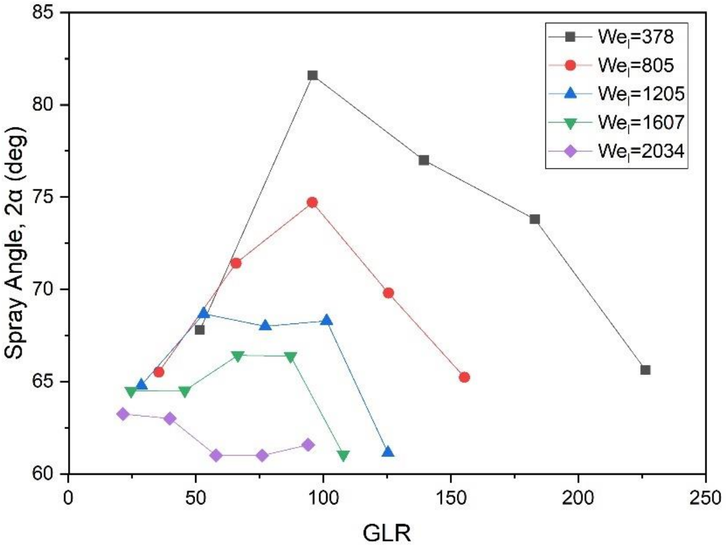

(b)

Figure 3.25 Spray angle of (a) internal mixing type and (b) external mixing type.

Due to these reasons, the characteristics of the two types of spray were different. In the case of the internal mixing spray, the spray angle decreased linearly as the GLR decreased [Figure 3.25(a)]. However, the linear model could not be presented as shown in Fig. 3.25(b) to the external mixing type due to other complex factors applied to the spray, such as friction between the liquid film and the wall, and liquid film inflation by gas flow.

Fig. 3.26 shows the result by performing multiple regression analysis of spray angle with two factors, We_l and Re_g. The abscissa is the dependent variable (spray angle) of the regression equation, and the ordinate is the actual spray angle obtained from experimental measurements. As a result of comparison between the regression model and the experimental values, the coefficient of determination (R^2) was more than 0.6 in both cases. The determination coefficient of the internal mixing type spray was 0.91. But regression model for external mixing type has low relativeness because it R^2 was only 0.64. Eqs (3.7) and (3.8) are the regression analysis equations for the spray angle of the internal mixing and the external mixing type, respectively. According to the equations, it was found that the effects on the spray angle of each type of We_l and Re_g are generally different.

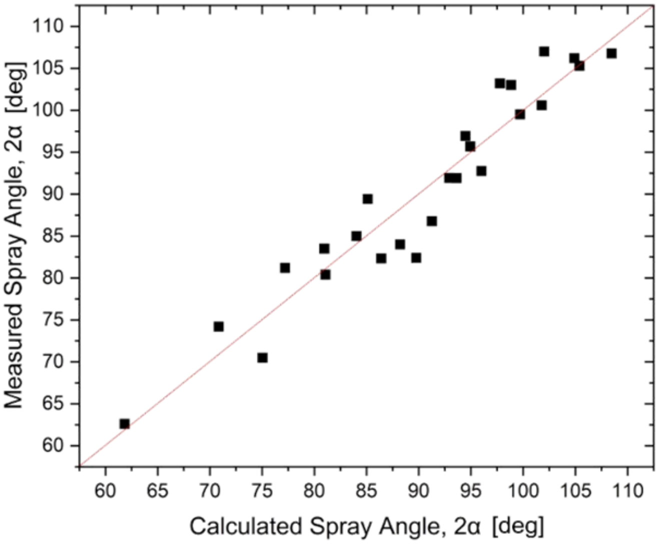

(a)

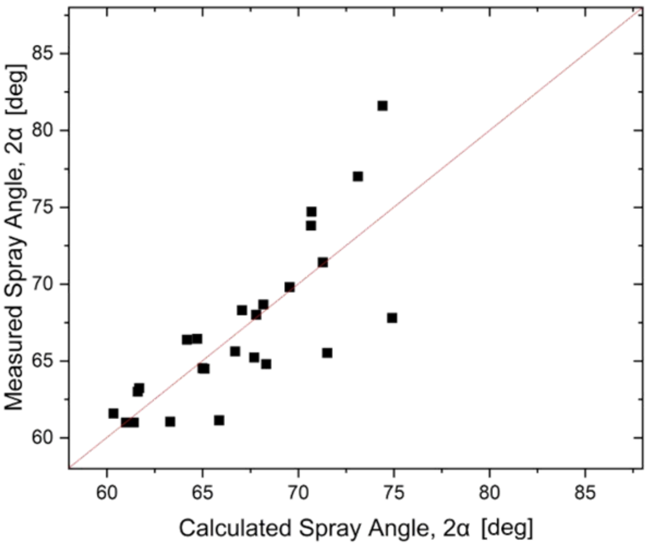

(b)

Figure 3.26 Spray angle model of (a) internal mixing type and (b) external mixing type by multiple regression analysis [Jeong et al. (2020)].

$$2\alpha_{int} = 93.57 + 9.00 \times 10^{-3} We_l - 8.08 \times 10^{-6} Re_g \tag{3.7}$$

$$2\alpha_{ext} = 78.02 - 8.03 \times 10^{-3} We_l + 3.33 \times 10^{-8} Re_g \tag{3.8}$$

3.3 Droplet Distribution of Internal and External Mixing Type Injectors

It can be expected that the breakup mechanism can be found by examining the distribution of droplets in the spray cross section. The liquid discharged through the injector has the form of a thin film. The liquid film is decomposed into a liquid ligament for some reason, and the liquid is decomposed into large droplets again. It is obvious that fine droplets were generated during this decomposition process.

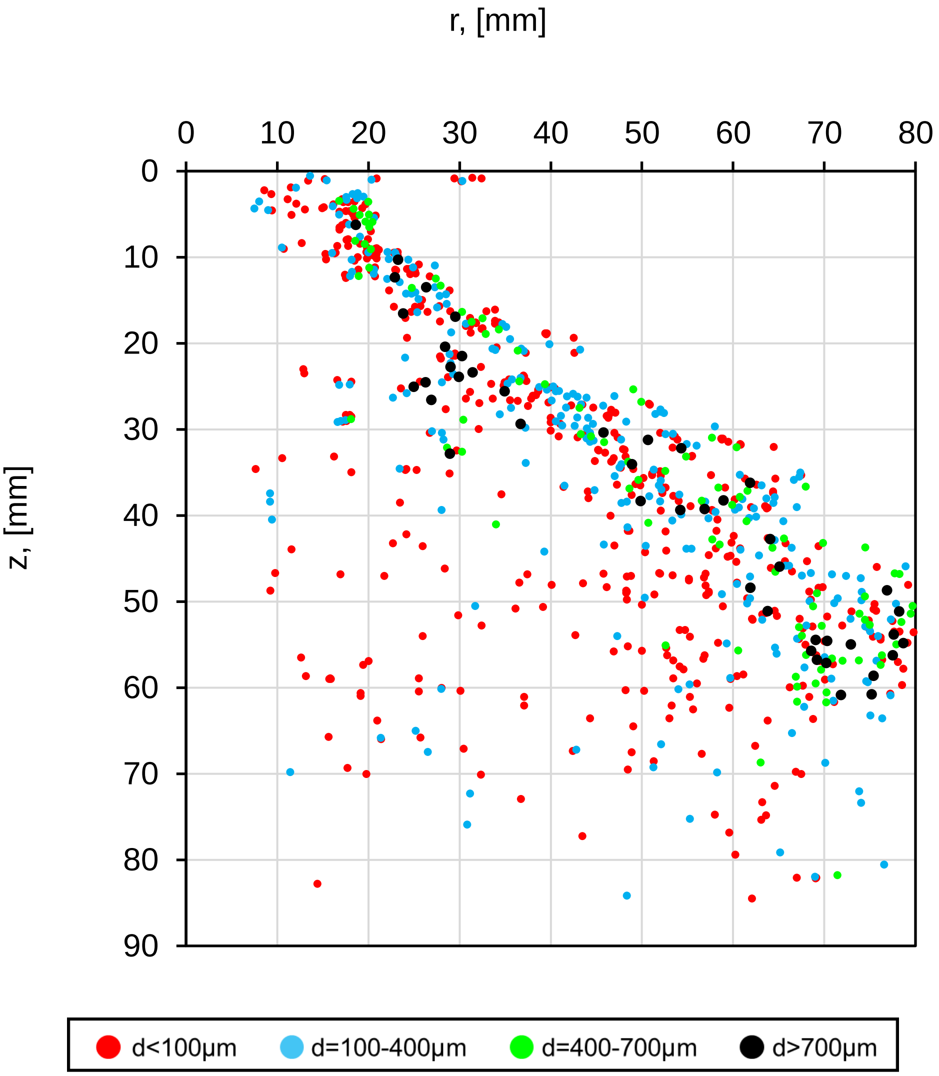
r, [mm]
0
10
20
30
40
50
60
70
80
z, [mm]
0
10
20
30
40
50
60
70
80
90
d<100μm
d=100-400μm
d=400-700μm
d>700μm

(a)

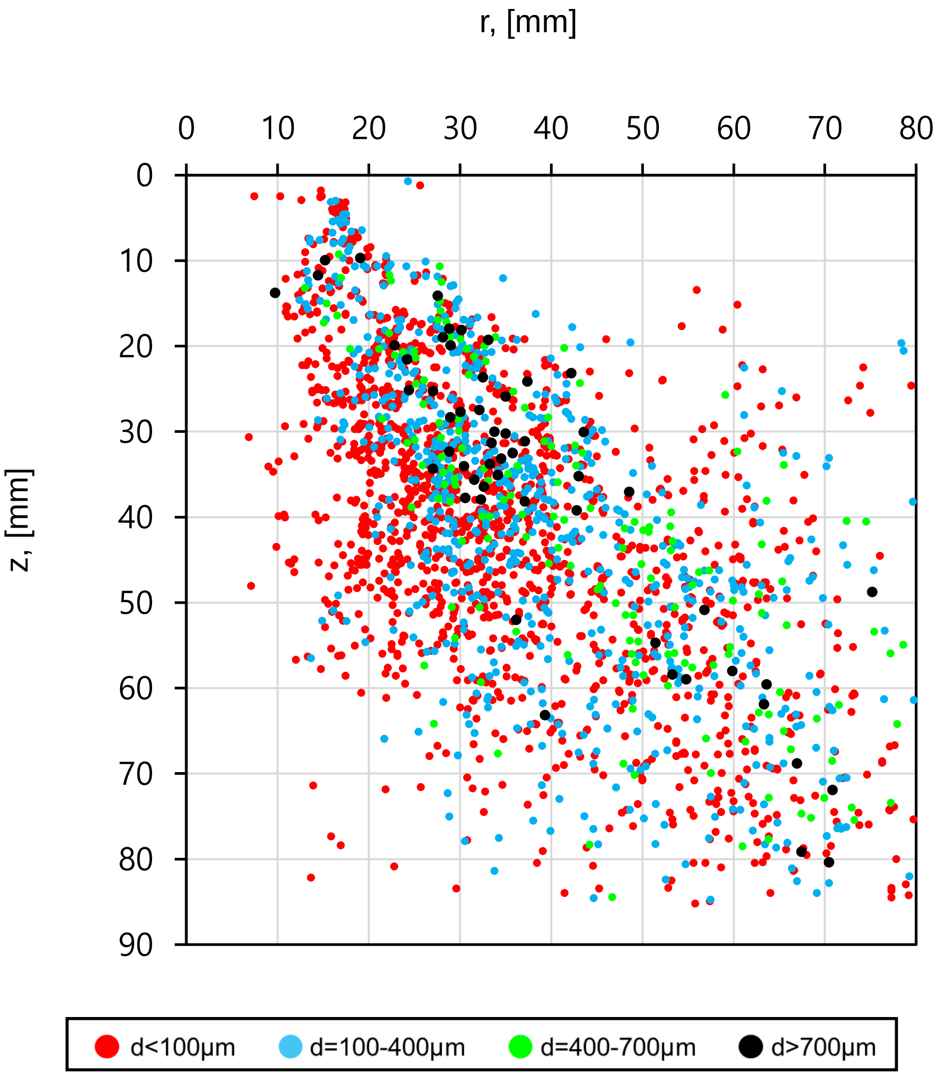
r, [mm]
0
10
20
30
40
50
60
70
80
z, [mm]
0
10
20
30
40
50
60
70
80
90
● d<100μm
● d=100-400μm
● d=400-700μm
● d>700μm

(b)

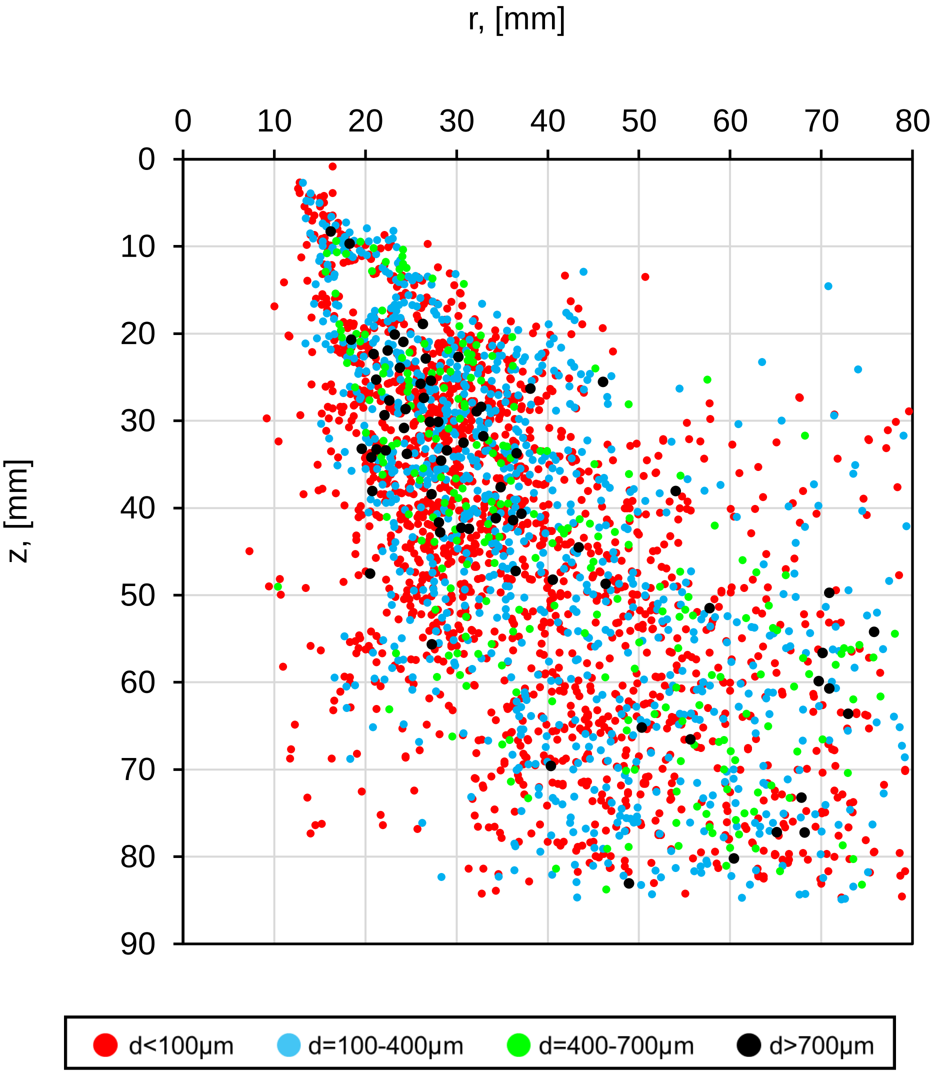
r, [mm]
0
10
20
30
40
50
60
70
80
z, [mm]
0
10
20
30
40
50
60
70
80
90
d<100μm
d=100-400μm
d=400-700μm
d>700μm

(c)

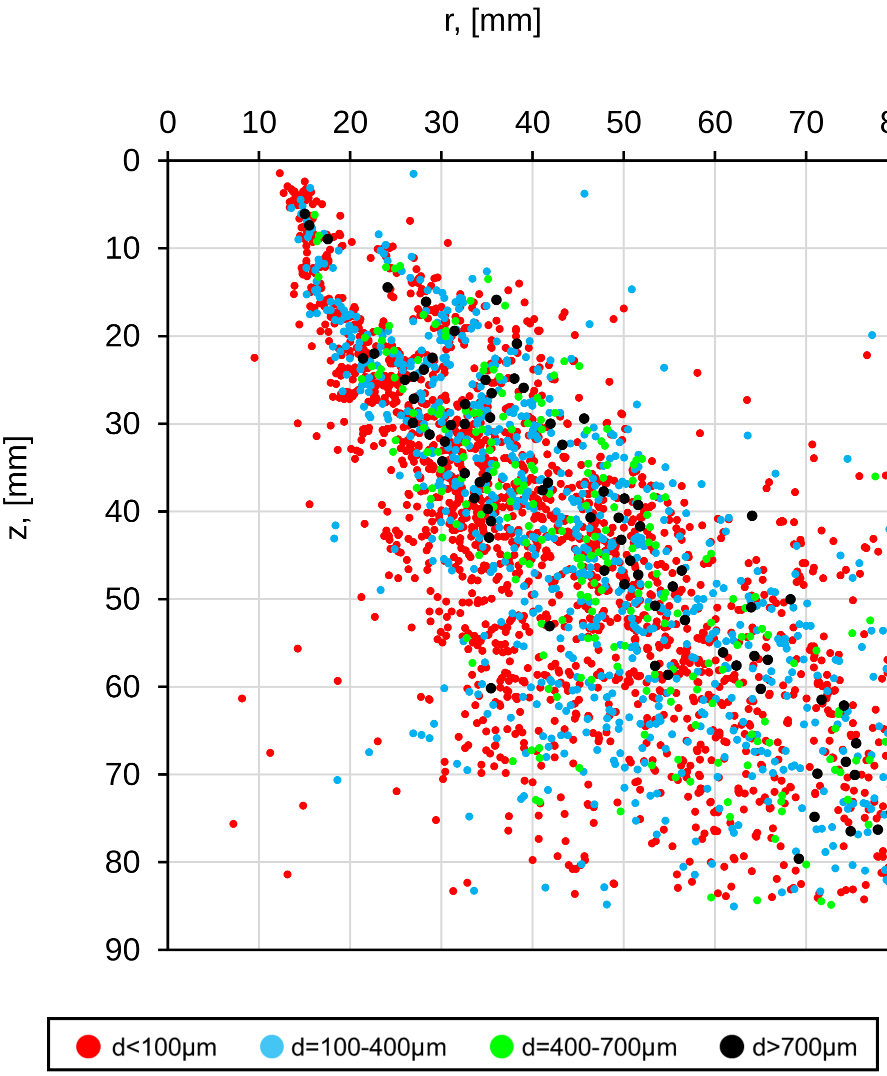
r, [mm]
0
10
20
30
40
50
60
70
80
z, [mm]
0
10
20
30
40
50
60
70
80
90
d<100μm
d=100-400μm
d=400-700μm
d>700μm

(d)

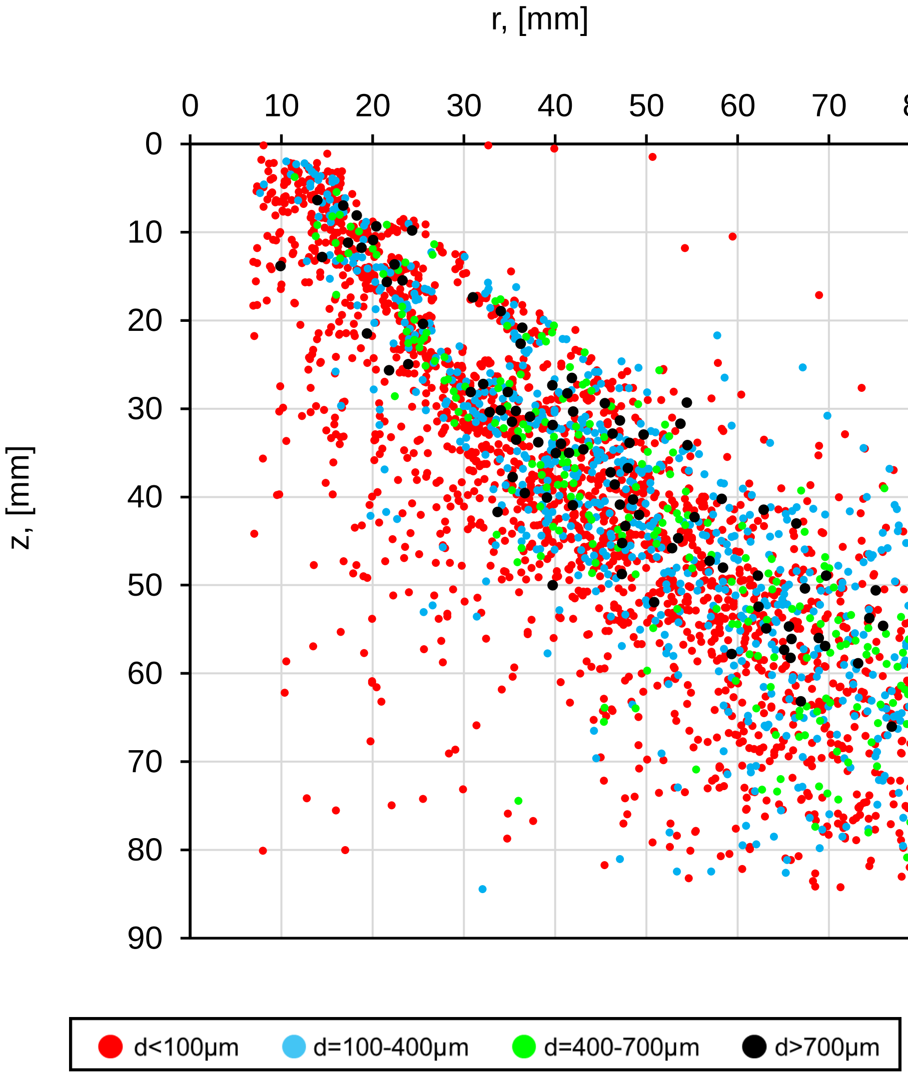

(e)

Figure 3.27 Droplet distribution of internal mixing type spray (a) $We_l = 284$; $Re_g = 0.13 \times 10^6$, (b) $We_l = 284$; $Re_g = 1.16 \times 10^6$, (c) $We_l = 284$; $Re_g = 2.77 \times 10^6$, (d) $We_l = 1060$; $Re_g = 2.77 \times 10^6$, (e) $We_l = 1777$; $Re_g = 2.77 \times 10^6$.

First, the droplet distribution of the internal mixing type is as follows. When the gas Reynolds number increased, the spray angle decreased. If the liquid Weber number and gas Reynolds number were both low value, droplets are generated only inside according to the droplet distribution [Figure 3.27 (a)]. The droplet area boundary was found, and there was no droplet found outside the boundary. However, microscopic droplets are also observed outside of the spray cone due to the liquid film breakup as the influence of the gas increased [Figure 3.27 (b)]. At this time, the spray angle decreased. And a large number of droplets were found inside the top of the spray cone ($z = 30 \sim 40 mm$). Droplets of various sizes are found in this area. When the Reynolds number of the gas further increased [Figure 3.27 (c)], the spray angle further decreased. In addition, droplets of all size ranges were mixed up and scattered. The cause of this phenomenon is that the spray cone contracted due to the gas pressure decrease and was directly affected by the main gas vortex. When the liquid film invaded the gas flow zone, the gas flow naturally penetrated the liquid zone.

At large gas Reynolds number, the spray angle increased as the liquid Weber number increased. When the Weber number of the liquid increases, the microdroplets mainly exist inside the spray cone [Figure 3.27 (d)]. Droplets of various sizes are still mixed under the spray under the decomposition of the liquid film. However, if the Weber number is increased further, fine droplets are mainly found inside as shown in (a) [Figure 3.27 (e)]. The fine droplets generated inside can be swept inside by the strong rotating gas vortex in the center. In addition, in liquid flow with increased inertia force, the changing rate in the traveling direction by the gas decreased. It can be said that the spray angle has increased like a simplex injector. The effect of the gas was constant, and as the flow rate of the liquid increased, the atomization was less affected by the decrease of central gas pressure. Therefore, it can be said that two independent cones appear in this case.

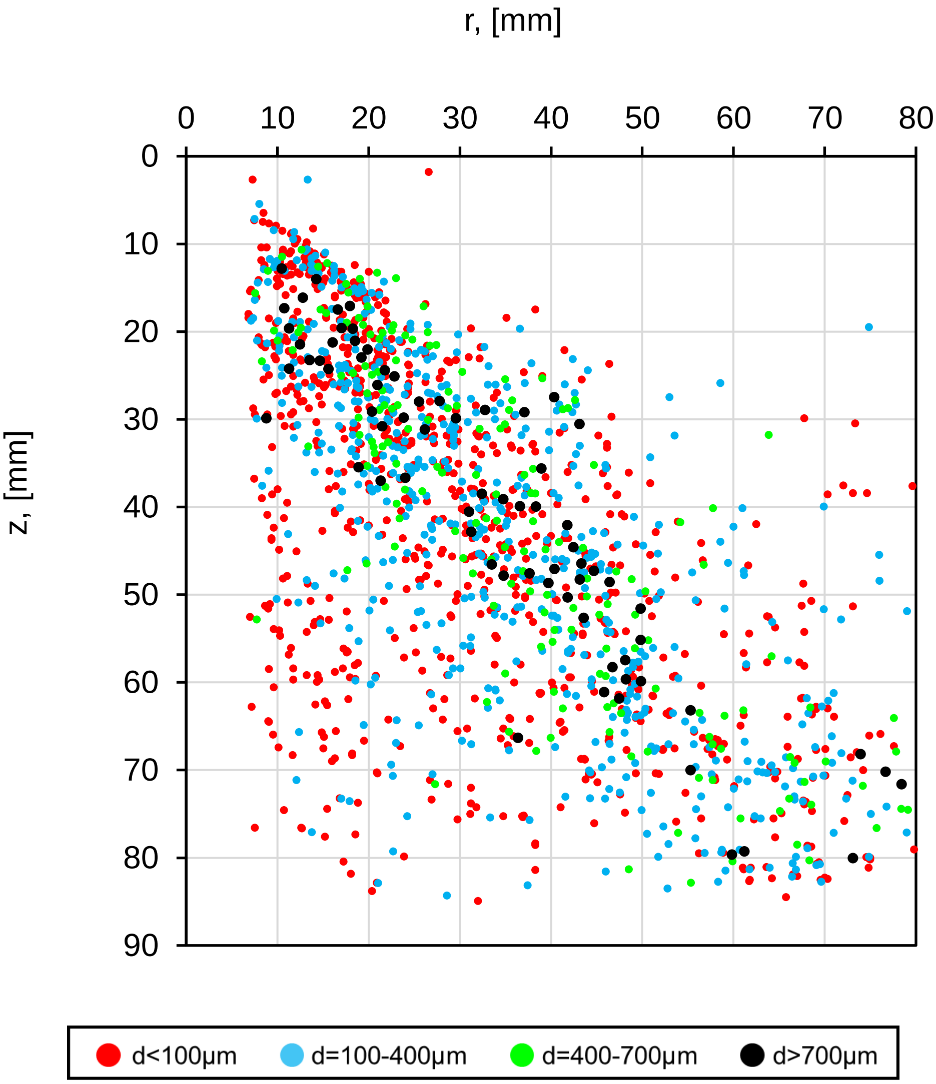
r, [mm]
0
10
20
30
40
50
60
70
80
z, [mm]
0
10
20
30
40
50
60
70
80
90
● d<100μm
● d=100-400μm
● d=400-700μm
● d>700μm

(a)

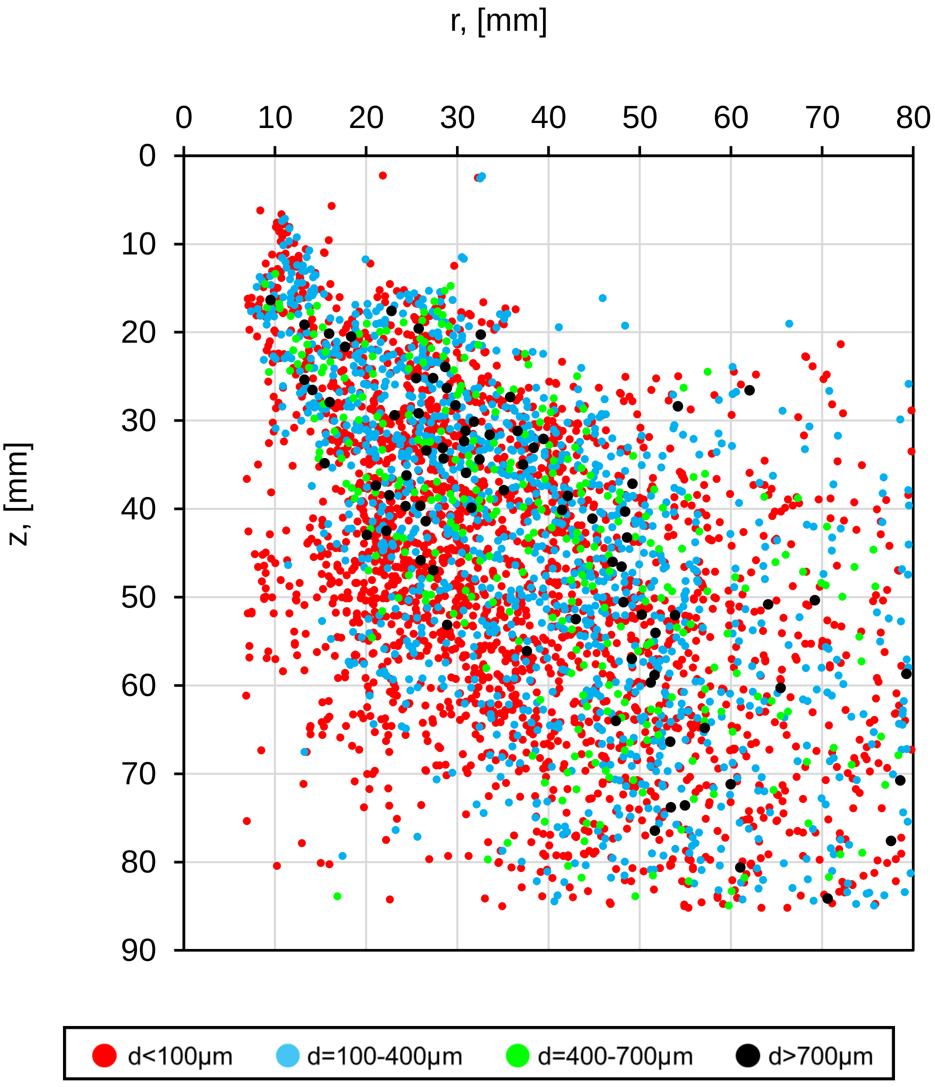
r, [mm]
0
10
20
30
40
50
60
70
80
z, [mm]
0
10
20
30
40
50
60
70
80
90
d<100μm
d=100-400μm
d=400-700μm
d>700μm

(b)

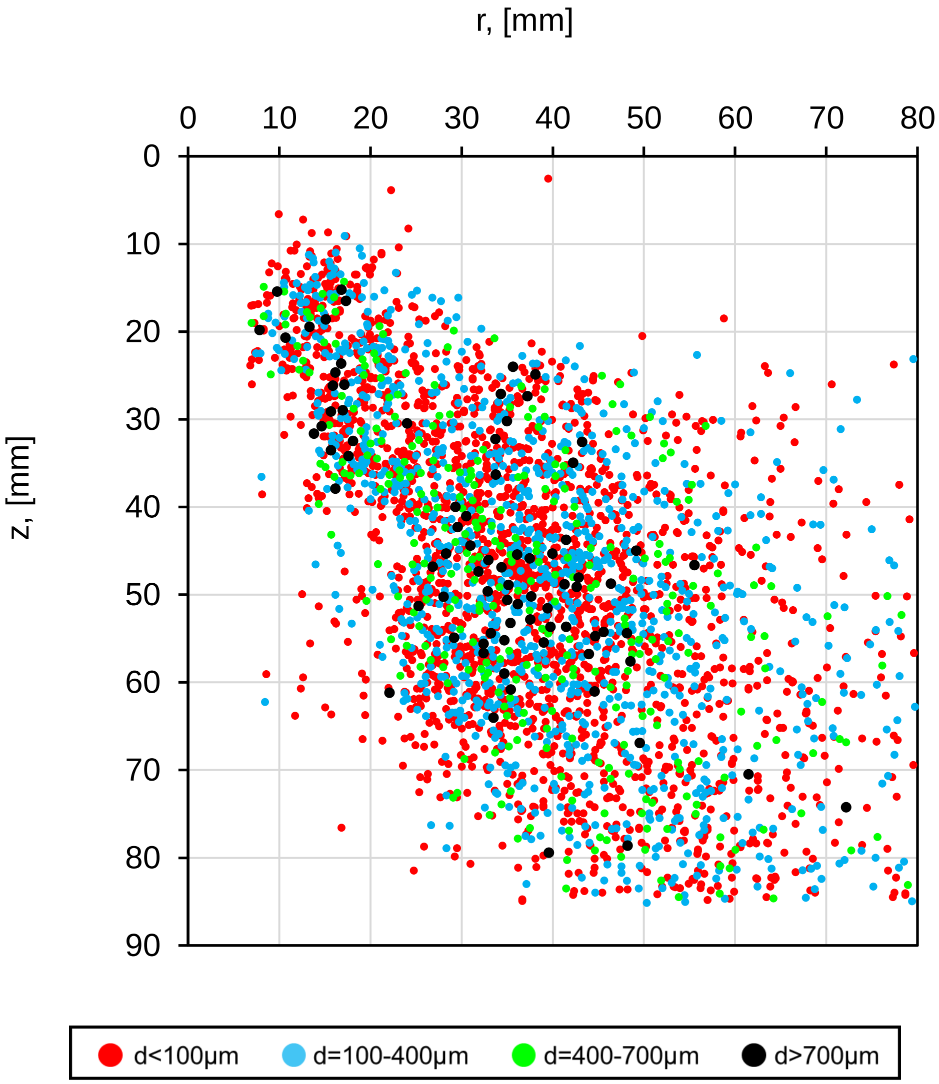
r, [mm]
0
10
20
30
40
50
60
70
80
0
10
20
30
40
50
60
70
80
90
z, [mm]
d<100μm
d=100-400μm
d=400-700μm
d>700μm

(c)

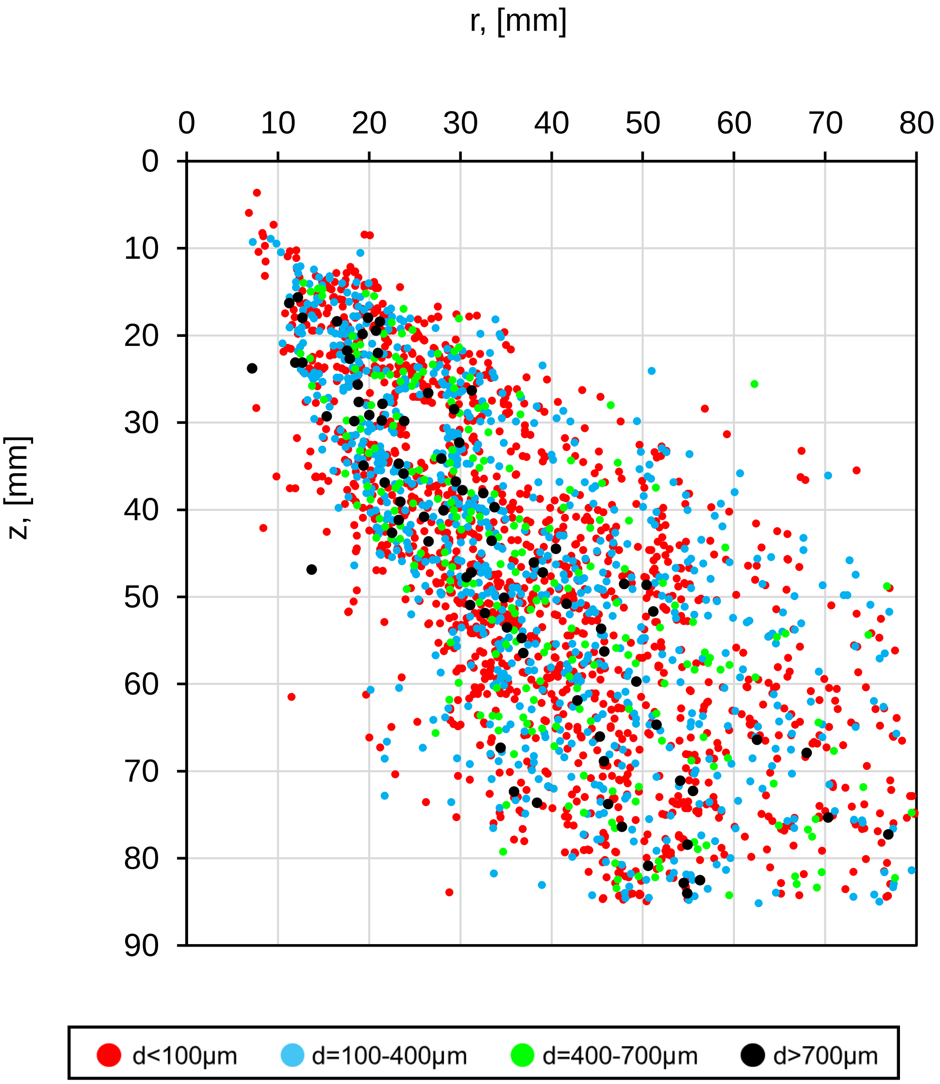
r, [mm]
0
10
20
30
40
50
60
70
80
z, [mm]
0
10
20
30
40
50
60
70
80
90
d<100µm
d=100-400µm
d=400-700µm
d>700µm

(d)

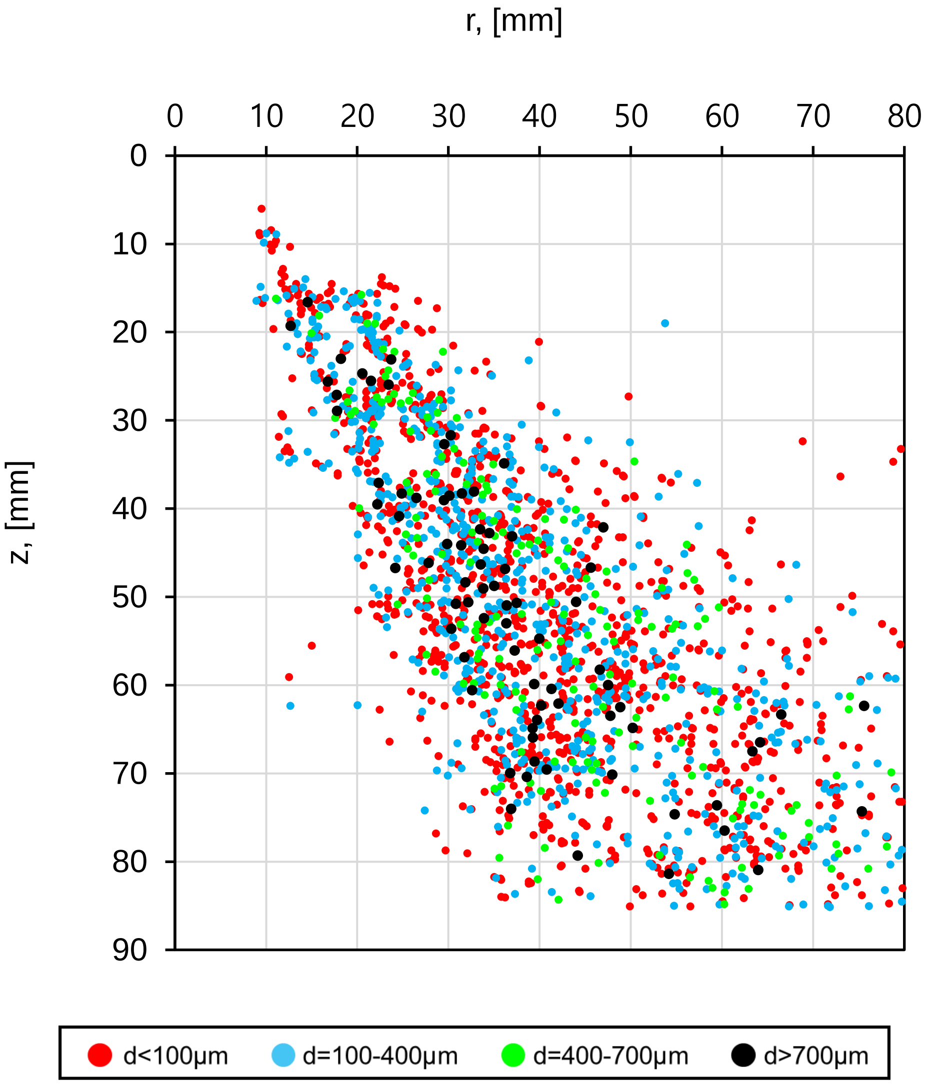

(e)

Figure 3.28 Droplet distribution of internal mixing type spray (a) $We_l = 378$; $Re_g = 0.13 \times 10^6$, (b) $We_l = 378$; $Re_g = 1.16 \times 10^6$, (c) $We_l = 378$; $Re_g = 2.77 \times 10^6$, (d) $We_l = 1205$; $Re_g = 2.77 \times 10^6$, (e) $We_l = 2034$; $Re_g = 2.77 \times 10^6$.

In the external mixing spray, small droplets were distributed inside and outside of the spray cone because the gas flow directly stroke the liquid film. In addition, it was confirmed again that the spray angle increased and then decreased [Figure 3.28(a) ~ (c)]. When the Weber number had low value, the liquid flow was well affected by the small gas flow. Small droplets were mainly distributed inside and outside of the area where large droplets are distributed when the gas flow had low Reynolds number [Figure 3.28(a)]. However, a large number of fine droplets are generated inside the spray cone, and large droplets were found to blow out as the gas flow rate increased [Figure 3.28(b)]. This is because the gas flow pushed the droplets out. However, it can be said that the liquid resisted such gas flow, so that the fine droplets were distributed inside. If the gas flow rate increased further [Figure 3.28(c)], the spray angle decreased again. It can be considered that the entrainment effect applied on this phenomenon. That is, the centrifugal force and attractive force simultaneously applied on the liquid film, and spray shape changed according to the strength of the two forces.

If the Weber number increased at a large gas Reynolds number, the spray angle decreased. And the area where droplets are found became considerably narrower [Figure 3.28(d) ~(e)]. This can be explained by increasing the inertial force as the Weber number increased. In this case, the gas flow simply interrupted the flow rather than penetrating the liquid film and dispersing the droplets outwardly.

The variance value of the droplet diameter was calculated in order to represent the above-mentioned numerically. A parameter that can represent the distribution of droplets on average is the spray angle (2α). The injector axis (OZ) and spray boundary line (IC) can be taken to represent the average spray cone as shown in Fig 3.29. The angle between OZ and IC is determined by the spray half angle α. The spray cone consists of a group of many droplets, and the location of each droplet can be determined by the vertical distance η from the spray boundary IC. The first factor for the calculation of the variance was η and the second factor was the droplet diameter *d*. The class interval of the first element was 5mm, and the interval of the second class was set to 100μm.

The results of this calculation are presented in Fig. 3.30. The zero point on the horizontal axis is the position on the line IC, and the negative and positive numbers mean that the droplets are located inside and outside the spray cone, respectively. The vertical axis is the dispersion value, and if the droplets of all diameter ranges are evenly distributed, the value increases. However, when droplets of a specific diameter range were concentrated, the variance decreased. In addition, the variance value had the value close to 0 in the position where droplets were merely detected.

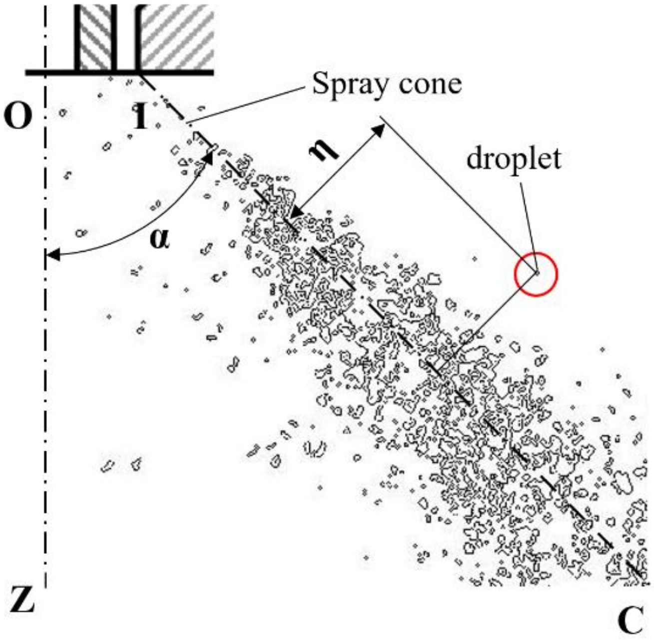

Figure 3.29 Droplet position for the spray cone.

The variance increased as Re_g increased as shown in Fig 3.30(a). This means that droplets are generated actively as the turbulence of the gas increased. In the process of increasing the Re_g value, the peak in the red line deviated from the spray boundary line. This is because, the liquid film could not endure and was pushed up even if the gas collides with the liquid in the injector in the relatively low We_l state. This is also confirmed in Fig. 20(b). The increasing rate inside the spray cone increased and the decreasing rate outside the spray decreased as the Re_g value increased [see Fig. 3.30 (a)]. This can be explained by the distribution of large droplets more than 700 µm in the upper area of the spray [Fig 3.27 (c)]. The gentle line to the right of the blue line peak might be understood as follows. The droplets that were slowly pushed out by the gas flow were broken by interaction with the ambient gas. Steep inclination can be considered that the droplet was drawn to the center and explosively decomposed as the value of Re_g increased.

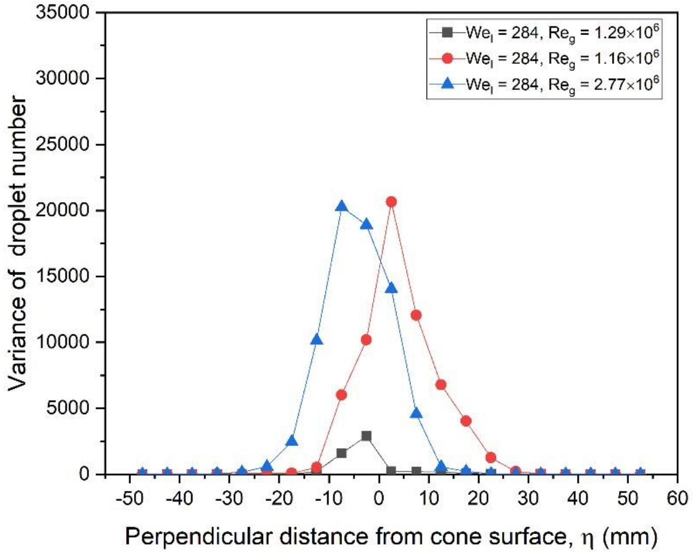

(a)

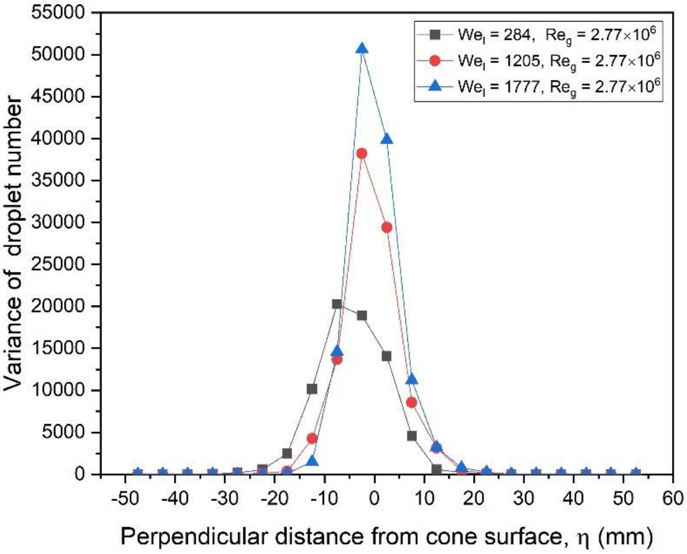
Variance of droplet number
Perpendicular distance from cone surface, η (mm)
We_l = 284, Re_g = 2.77×10^6
We_l = 1205, Re_g = 2.77×10^6
We_l = 1777, Re_g = 2.77×10^6
0
5000
10000
15000
20000
25000
30000
35000
40000
45000
50000
55000
-50
-40
-30
-20
-10
0
10
20
30
40
50
60

(b)

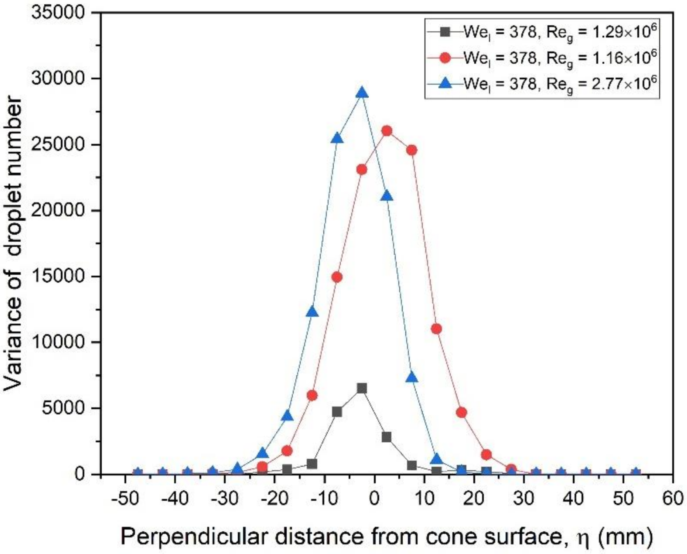
Variance of droplet number
Perpendicular distance from cone surface, η (mm)
We_l = 378, Re_g = 1.29×10^6
We_l = 378, Re_g = 1.16×10^6
We_l = 378, Re_g = 2.77×10^6
0
5000
10000
15000
20000
25000
30000
35000
-50
-40
-30
-20
-10
0
10
20
30
40
50
60

(c)

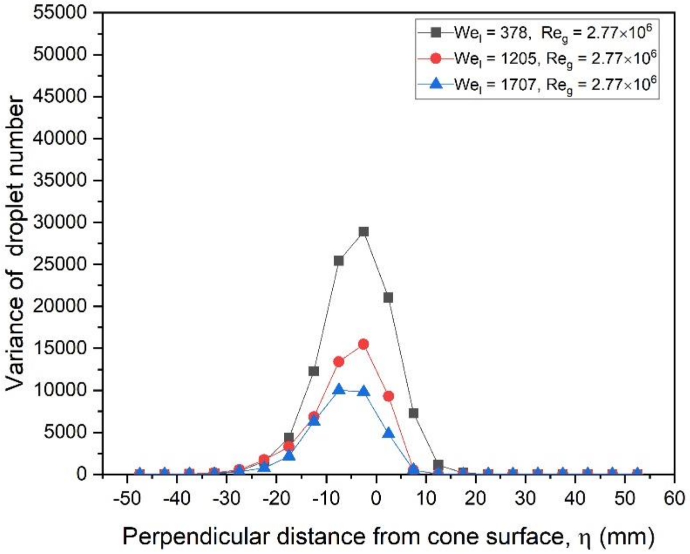

(d)

Figure 3.30 Droplet distribution of the internal (a and b) and external (c and d) mixing types.

Fig. 3.30 (b) shows that both the variance and the changing rates increased as the We_l value increased. As shown in Fig. 3.27 (e), the inside of the spray was filled with fine droplets of less than 100 μm, reducing the variance value. Both large and fine droplets were found in large quantities at the boundary of the spray cone. It can be said that the variance value was high due to scratching by the gas flow, and the variance gradually decreased as the droplets were decomposed by the ambient gas.

Fig. 3.30 (c) showed a similar form to the internal mixing spray. However, the range was wider in which the high variance value was maintained. As shown in Fig 3.28(b), the peak of the red line seemed to have shifted to the right since the droplet was pushed outward. The blue line peaks went back inward. The reason is attraction force increased by the entrainment effect.

In Fig 3.30 (d), the opposite trend was revealed. As We_l increased, variance and slope of the variance line were decreased. As shown in Fig. 3.14, this is because the gas flow only struck cut off the liquid film periodically but did not disperse it. It was confirmed that the atomization process weakened as the liquid inertia increased, the number of We_l increased and the *GLR* decreased.

3.4 Discussion on Atomization Mechanism of the Internal and External Mixing Type Injectors

In coaxial gas-liquid injectors using gas swirl injectors, the spray pattern changed differently from gas jet injectors depending on the injector supply conditions. This is because they intentionally have a velocity vector in a direction different from the axial direction.

In general, the spray angle increased as less droplets were swept into the central gas turbulence zone, since the high liquid Weber number increased (the inertial force increased) in the internal mixing type spray. Also, the spray angle increased as the gas Reynolds number decreases. It means that the gas velocity decreased so that the pressure difference between interspace and ambient atmosphere. In this case, the centrifugal force of the gas is relatively increased to push the liquid film, but the liquid film fluctuates toward the surface of the injector head due to the recessed region. Also, mainly because the gas scrapes the liquid film, a mist zone developed in the axial direction from the center. As the gas Reynolds number decreased, the area became smaller (see Figure 3.31).

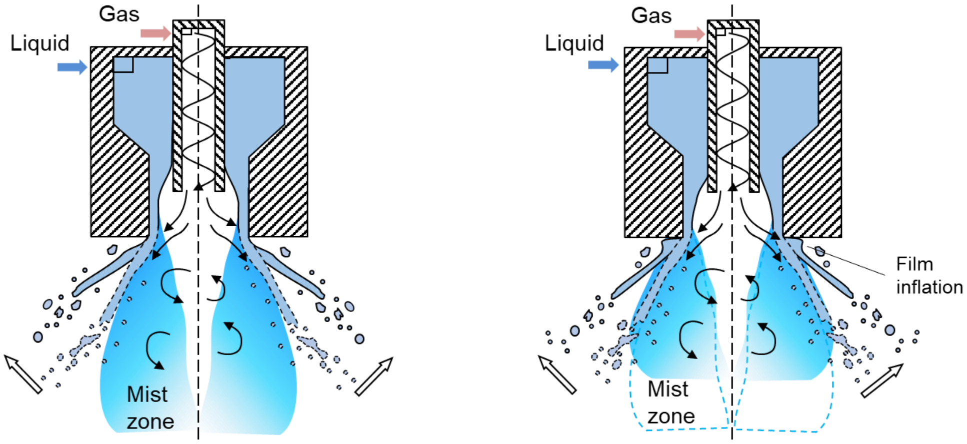

(a) (b)

Figure 3.31 Schematics of breakup mechanism of internal mixing gas-liquid spray (a) with increasing We_l and (b) with decreasing Re_g.

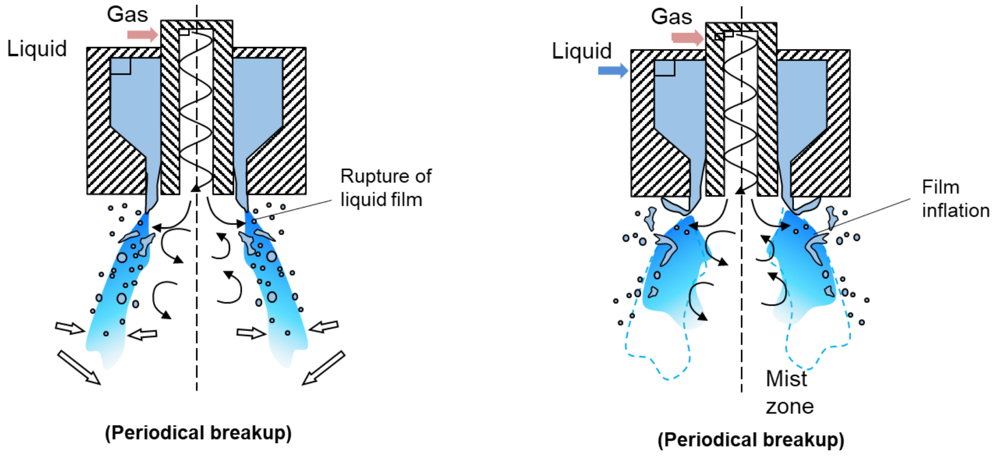

(a) (b)

Figure 3.32 Schematics of breakup mechanism of external mixing gas-liquid spray (a) with increasing We_l and (b) with decreasing Re_g.

In the external mixing type spray, the gas periodically cuts the upper part of the liquid film, creating a mist-zone along the cone. Therefore, when the liquid inertia of the liquid film increased, the gas could not hit to scatter liquid, so that the droplets appeared only in a narrow area. As the liquid weber number increased, the spray angle decreased. The gas vortex cone has the force to push the liquid by rotation and the force to draw the liquid to the center due to the entrainment effect. If the force extruded by the gas vortex is greater than the attractive force of the entrainment effect, the liquid film is lifted up. As with internal mixing injection, the range of the mist zone decreased as the gas Reynolds number decreased (Fig. 3.27).

CHAPTER 4

PERIODICITY MECHANISM OF EXTERNAL MIXING TYPE SPRAY

4.1 Objectives and Test Conditions

As shown in Chapter 3, the spray patten of external mixing type injector has some periodic characteristics. According to Knysh & Uryvsky (1982) and GOST 21980-76, gas swirl injectors can generate their own gas fluctuations. Squire (1953) and Fraser et al. (1963) stated that instability occurs when there is a difference in gas velocity adjacent to both sides of the liquid film, and it is broken into fine droplets when the gas flow and liquid film meet outside the injector. According to Clark & Dombrowski (1972), as the aerodynamic turbulence increases, the liquid film breakup process is accelerated.

Table 4.1. Spray conditions and geometrical dimensions of liquid and gas injector parts.

Fluid Parameter	Liquid (Water)	Gas (Air)
Differential pressure, Δp (bar)	0.5, 1, 1.5, 2, 4, 6, 8, 10	2, 4, 6, 8, 10, 11, 12
Mass flow rate, (g/s)	67 ~ 321	4 ~ 505
Axial velocity, (m/s)	4 ~ 22	75 ~ 392
Weber number	72 ~ 1674	$0.2 \times 10^5 \sim 5 \times 10^5$

Jeong (2004) stated that the impact force in the event of a fluid flow collision is an important factor affecting the liquid film breakup and wavelength. According to the results of the preceding studies, it is expected that oscillation related to droplet generation occurs when gas vortices collide with the inner surface of the liquid film. The characteristics of air-blast injectors using gas swirlers for gas turbine engines have been dealt with by several researchers such as Lefebvre (1980), Batarseh (2009), and Aigner et al. (1988, 1963). It can be said that relatively few studies have been conducted on the case using a gas swirl injector. In this chapter, the dynamic liquid film breakup characteristics of the external mixing type GCSC injector for small thrusters were studied in which a gas swirl injector having the same rotational direction as that of the liquid swirl injector is located at the center. The geometric parameters of the external mixing type injector are shown in Tab. 3.1 and test conditions are presented in Tab. 4.1.

4.2 Acoustic Oscillation of Gas Swirl Injector

According to Schetz et al (1980), it is known that liquid instability occurs under conditions of high gas velocity when liquid jet is injected in a gas cross flow. Since a relatively large liquid flows into a low gas stream, this type of spray has a density similar to Rayleigh-Taylor instability. As shown in Fig. 4.1, waves were generated on the surface of the liquid column disturbed by the gas and bend to the direction of the gas. After that, the liquid clump was separated from the liquid column and showed a pattern of atomization. As soon as the liquid column exited the jet orifice, it was simultaneously affected by the gas flow. It is obvious that aerodynamic forces and surface tension dominate the decomposition of liquid columns in this environment. Schetz and Sherman (1970) experimentally suggested that there was a periodicity in this fracturing process using high-speed imaging technique [see Fig. 4.2]. The amplitude of the jet surface wave increases downstream of the gas, and the lumps are separated at the valleys of the wave. The reason for this repetition is that liquid jet needed time to reach the fracture condition, and the jet stream continued to grow after breakup. Less et al. (1986) used the term ‘fracture frequency’ for this periodic breakup and stated that the frequency is dependent on the velocity of the gas and the Weber number of the liquid.

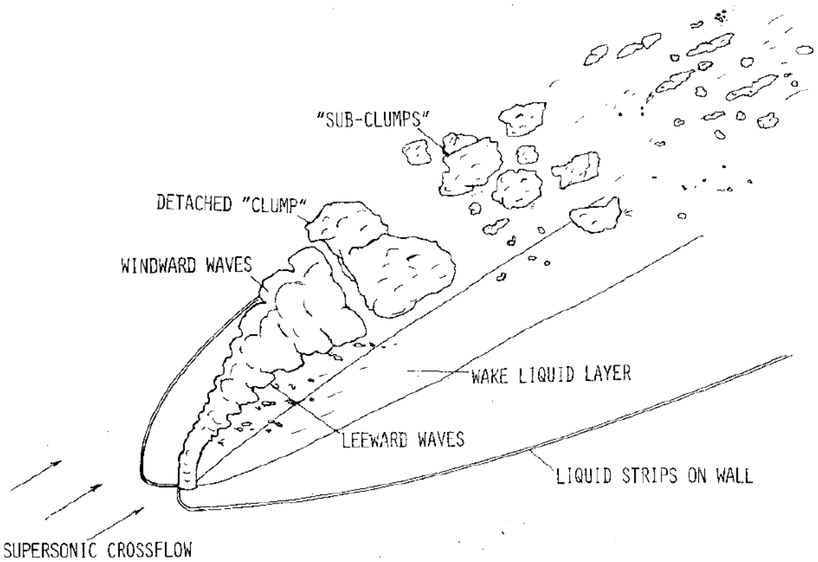

Figure 4.1 Schematic of Jet breakup in the high-speed gas cross flow [Schetz et al. (1980)].

The liquid film is forcibly torn by gas in the external mixing type spray used in this study, so the periodic droplet cluster mentioned in Chapter 3 is considered to be similar to breakup process of jet crossflow. However, there was an inherent rotational inertia as well as aerodynamic force in the liquid film, since the liquid injector is also a vortex type. Also, the effect of the gas discharged from the swirl injector on the outer liquid film cannot be said to be the same as that of the gas in the jet in cross flow. Therefore, it is unreasonable to conclude that both types of spray have the exact same breakup mechanism.

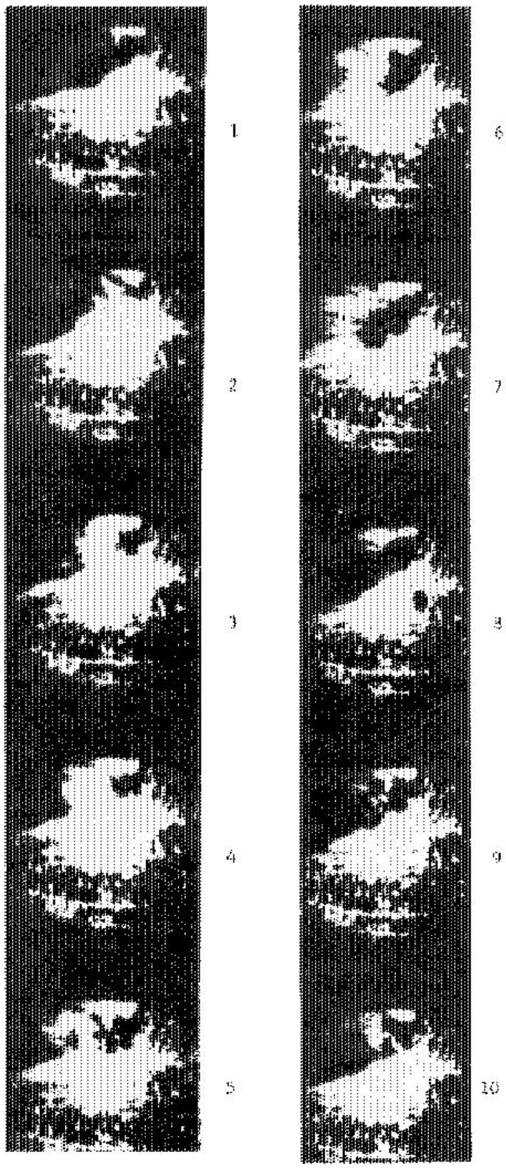

Figure 4.2 Jet breakup images from a high-speed video (gas moves from right to left) [Schetz & Sherman, (1970)].

The gas swirl injector has been used practically and experimentally in the field of liquid rocket engines, but there have been few research data dealing with its effect on liquid atomization. It is known that the exhaust gas flow while rotating in a closed tube causes acoustic vibration. Vonnegut (1954) experimentally suggested that the gas pressure flowing into the tube and the ambient pressure are related to these vibrations, and Michelson (1955) tried to understand this phenomenon in the thermodynamic point of view. The frequency of noise generated by the vortex whistle presented by Vonnegut (1954) was as shown in Eq. (4.1), and the derivation of this equation was included in appendix III:

$$f_g = \frac{a}{\pi D} \nu_t \sqrt{\frac{\Delta p}{p_1}}\ , (Hz) \tag{4.1}$$

where, a – speed of sound (m/s), D – inner diameter of the swirl chamber (m), Δp – differential pressure (bar), ν_t – a factor that considers the decrease in tangential velocity in the swirl chamber due to friction ($\nu_t < 1$).

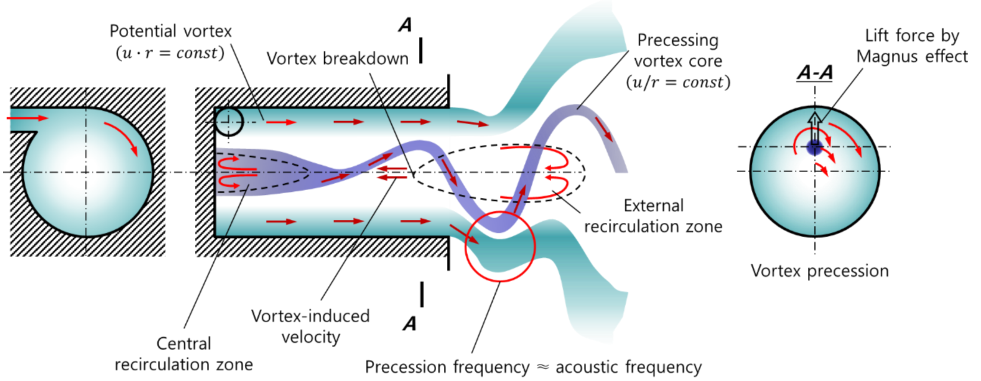

Figure 4.3 Gas perturbation by vortex type injectors [Knysh (1999)].

Knysh (1977) and Knysh (1999) summarized the phenomena that occur in the swirl injector under conditions similar to the properties of the working fluid and the ambient medium as follows. After the rotating gas is introduced from the tangential inlet, the rotational energy is transferred and starts to rotate together. The outer vortex can be conditionally named as a potential vortex, and the secondary vortex that starts to circulate along with it - vortex core. It is believed that the conservation of the velocity moment according to the radius is established in the potential vortex:

$$u \cdot r = const$$

where, u – tangential velocity component, r – current radius. However, the tangential velocity component of the vortex core complies with the rigid body rotation law (ω = const) in this flow region, and the velocity is distributed differently from the potential vortex:

$$\frac{u}{r} = const.$$

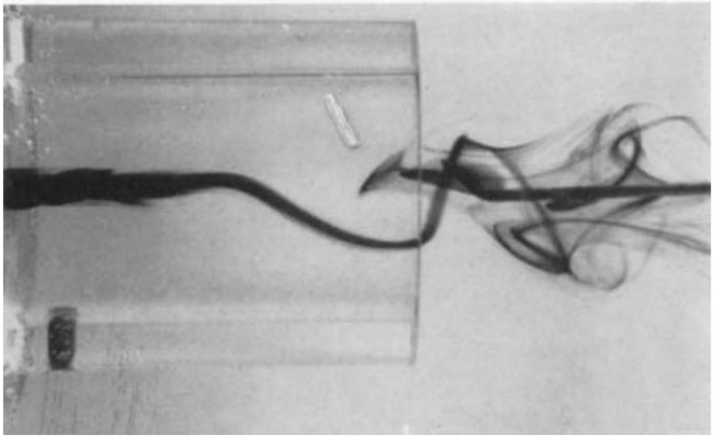

Figure 4.4 Vortex core at high Reynolds number [Chanaud (1964)].

The pressure decreases due to the rotational velocity in the vortex core. For this reason, external gas is introduced into the center creating an external recirculation zone when the ambient pressure is increased. In this case, perturbation occurs when the axially symmetric flow collapses. The vortex core exiting from the inside decelerates while colliding with the recirculation region and changes into a form of precession as it rises above the recirculation region. The change to precession is related to the lift caused by the Magnus effect. Due to this effect, the potential eddy current produces periodic velocity perturbations. This phenomenon is summarized in Fig 4.3.

Chanaud (1964) obtained a photograph of a vortex core at a high Reynolds number. When liquid was injected in the liquid medium with the same density as working fluid, dye was flowed from left to right in order to determine the distortion of the vortex core. Here, the precession and recirculation regions of the core were observed. According to Knysh et al. (1982), this phenomenon mainly occurs when the difference in density between the working fluid and the medium is small. Strong pressure vibration occurs due to this instability, which propagates to the outside in the form of sound waves. According to Chanaud (1963), the regular precession frequency of the secondary vortex coincides with the acoustic frequency and is related to the rotational angular velocity of the semi-rigid flow core. Suzuki (1960) theoretically approached the process of sound generation in the vortex conduit in the stable zone, and studied the interaction between the semi-rigid core and the potential vortex by the micro-perturbation method. As a result, the vibration frequency was expressed as $f = \omega\,\lambda$: where, ω-angular velocity of the vortex core, λ – tangential wave number.

Knysh and Uryvsky (1982) established an equation (4.2) for the definition of vibration frequency based on the analysis of the experimental results.

$$f_g = \frac{u_{gz}\left(1 - \frac{\varphi}{2}\right)}{\pi d_n \sqrt{\frac{\varphi}{2}}(1 - \varphi)} \left[1 - \xi \frac{0.675 A_g \bar{L}}{1 + 0.2 A_g}\right] \frac{1}{1 + \frac{1 - \varphi}{4}} \tag{4.2}$$

The apparatus shown in Fig 4.5 was used to measure the frequency of the noise generated by the gas vortex injector. The pressure change of the injected gas was measured, since acoustic vibration is a longitudinal wave propagating in the air. A dynamic pressure sensor (102A05, PCB Piezotronics) was installed 3cm below the injector, and the pressure change over time was converted into an electric signal. The signal passing through the sensor, sensor signal conditioner and amplifier is controlled by the Labview program on the computer, and the frequency was analyzed using the FFT method (Fig. 4.5).

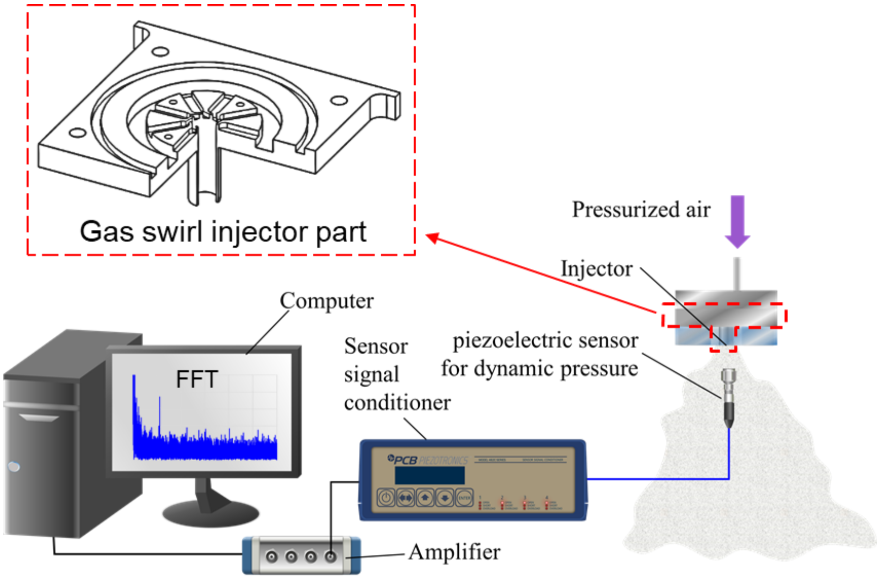

Figure 4.5 Experimental arrangement for pressure oscillation of gas flow from injector.

As the gas Reynolds number increases, the frequency of sound waves tends to increase. In the Eq. (4.1), the minimum error is less than 10% in each experimental condition when the friction coefficient (v_t) is equal to 0.34. In Eq. (4.2), the axial speed was used as a factor. In this experiment, the axial velocity and the differential pressure are linearly proportional, and the gas velocity is close to the sound velocity. It is known that when the density of the ambient gas is less than that of the working fluid, the vortex structure collapses precession occurs due to the pressure drop at the outlet of the injector. In this relationship, Knysh (1977) tried to find out the relationship between the geometric factor and frequency of the injector. In his experiment, a working fluid (liquid) at a low numerical value was injected into the liquid medium. In equation (4.2), the factors representing the flow conditions were the axial velocity and the friction coefficient of the fluid against the wall. In Fig. 4.6, the difference from the experimental value was small at low velocity, but the difference between the value increased as the velocity increased. Therefore, it can be said that Eq (4.2) is somewhat inadequate for high gas velocity conditions.

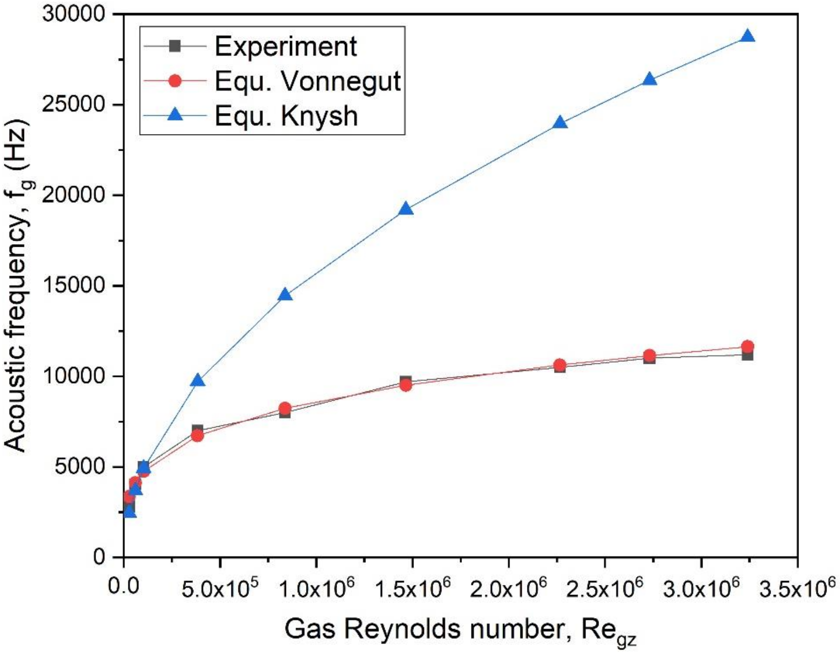

Figure 4.6 Comparison of gas acoustic frequency (f_g) from experimental result and by calculation with empirical equations.

4.3 Breakup Mechanism of the External Mixing Spray

The fracture frequency (f_f) when gas was applied to the liquid film was measured by the method shown in Fig 2.7. As shown in Fig. 4.7, the gas acoustic frequency (f_g) and fracture frequency (f_f) increased as the axial gas velocity increased. Whereas f_g had a range of several thousand Hz, f_f of the liquid film in the case where gas and liquid interacted was in the range of several hundred Hz.

This is quite different from the case shown in the study of Im et al. (2009). In a liquid-centered gas-liquid coaxial swirl injector using a gas jet injector and a recessed region, the acoustic frequency of the gas coincided with the spray frequency. As the gas was blocked by the liquid film, the resistance of the liquid caused a change in the gas pressure. As shown in the image on the left of Fig. 4.8, the liquid film oscillation existed even in the absence of the central gas flow. However, the oscillation frequency of the liquid film was not detected near the injector outlet. It was observed that when the gas normal velocity u_{gn} increased, the still liquid film burst and droplets were generated. According to these observations, it was implied that not all gas perturbations resulted in the effective breakup of the liquid film.

Due to the existence of liquid film vibration due to friction between the injector nozzle wall and liquid flow according to Plateau–Rayleigh instability theory, and liquid film vibration due to liquid motion in a stationary gas medium according to a study by Dombrowski et al. (1970), there may be periodic generation of droplets even if there is no additional gas flow. By the analysis procedure shown in Fig. 4.9, the droplet distribution frequency was obtained at the point where breakup was ended in the liquid spray image. The amount of liquid passing through the red dotted line changed over time. As shown in Fig. 4.9, the numerical values were digitized, and the frequency was obtained again using the FFT method. This may be the liquid fracture frequency (f_l) when no gas is applied on the liquid flow.

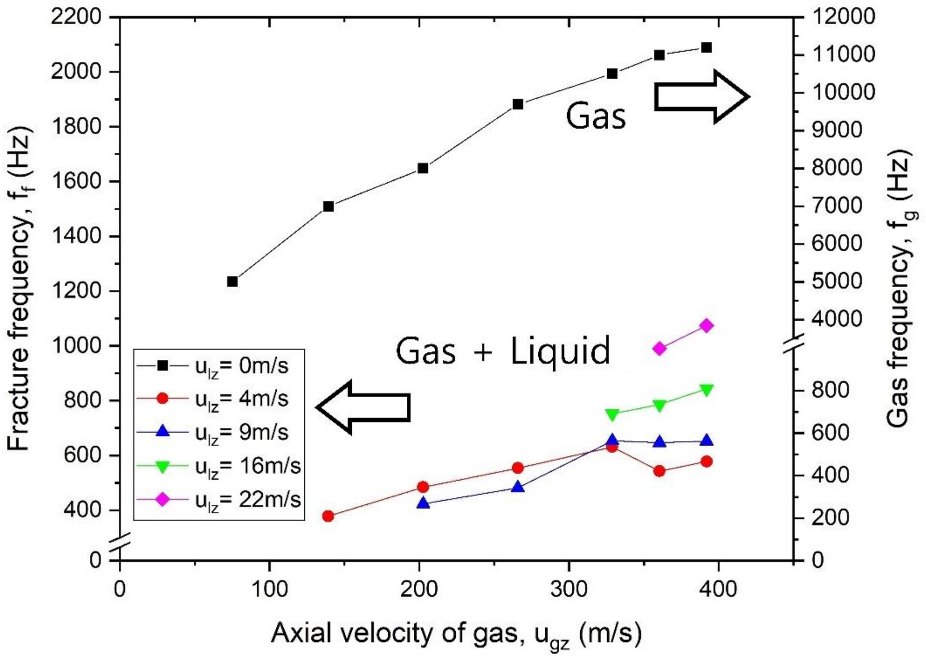

Figure 4.7 Gas frequency (f_g) and gas-liquid frequency (f_f) dependent on the axial gas velocity.

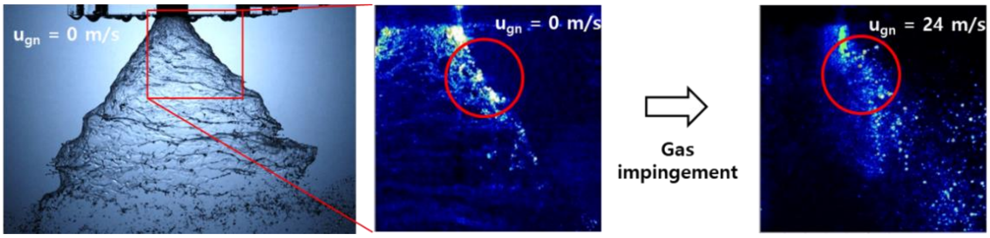

Figure 4.8 Fractural breakup of liquid film caused by gas flow.

As a result of this analysis, the frequency increased as the liquid velocity increased (Fig. 4.10). The periodicity of droplet decomposition in a liquid spray cone is similar to that of gas-liquid sprays. However, when gas flowed out of the central injector, liquid breakup occurred near the injector outlet. As described above, it cannot be said to have the same reason when only a liquid spray cone existed since it was decomposed into a liquid film only after a perforation occurred on the liquid film.

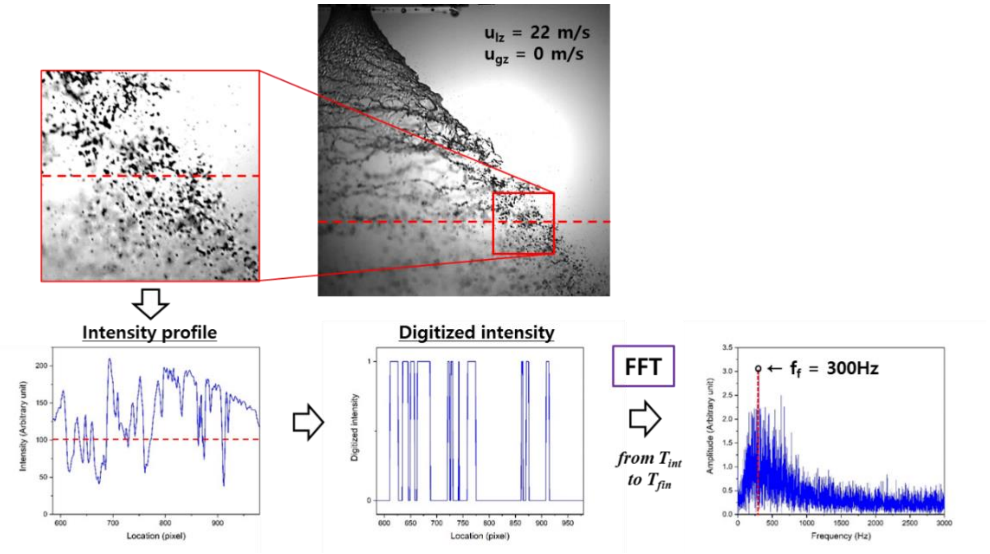

Figure 4.9 Measurement of liquid-only spray frequency.

When gas flow impinges on the liquid film, the breakup length was visually revealed. Fig. 4.11 showed a conceptual diagram of the gas flow impingement on liquid film. The generated droplets moved in a direction perpendicular to the liquid film. This was analytically and briefly shown in Fig 4.11(b). The normal vector (u_{gn}), breakup length (h), and impinging angle (θ) of the gas flow to the liquid film surface can be calculated geometrically.

The turbulent gas flow in this experiment moved in axial direction with oscillational and rotational movement. According to the analysis of images taken with the Schilleren technique, they generally have conical flow. The liquid film can affect the gas flow and change the velocity field. However, this study did not deal with the difference between the case of injection only gas and the case which the liquid and gas are simultaneously injected. The gas injection angle was calculated based on the breakup position as in Eq. (4.1), and the impinging angle (θ) was regarded as the difference between the liquid injection angle and the gas injection angle. The axial velocity of the gas and liquid flow was determined by the flow rate of each injector, as shown in Eqs. (4.2) and (4.3). Δd was determined as the distance in the radial direction (r) from the inner surface of the nozzle of the inner end to the inner wall of the annular end, and its value was 3.59 mm. F_g, F_l are the cross-sectional area of the nozzle outlet filled with gas and liquid respectively. The gas velocity can be separated into a vector ($\overrightarrow{u_{gn}}$) perpendicular to the liquid film and a vector ($\overrightarrow{u_{gl}}$) parallel to the liquid film. Therefore, the normal vector u_{gn} was expressed as Eq. (4.5).

$$\theta = \alpha_g - \alpha_l = \tan^{-1}\left(\frac{\Delta d + t + h\tan\alpha_l}{h}\right) - \alpha_l \tag{4.1}$$

$$u_{gz} = \frac{\dot{m}_g}{\rho_g\, F_g} \tag{4.2}$$

$$u_{lz} = \frac{\dot{m}_l}{\rho_l\, F_l} \tag{4.3}$$

$$\overrightarrow{u_g} = \overrightarrow{u_{gn}} + \overrightarrow{u_{gl}} \tag{4.4}$$

$$u_{gn} = \frac{u_{gz}\ sin\,\theta}{\cos\left[\tan^{-1}\left(\frac{\Delta d + t + h\tan\alpha_l}{h}\right)\right]} \tag{4.5}$$

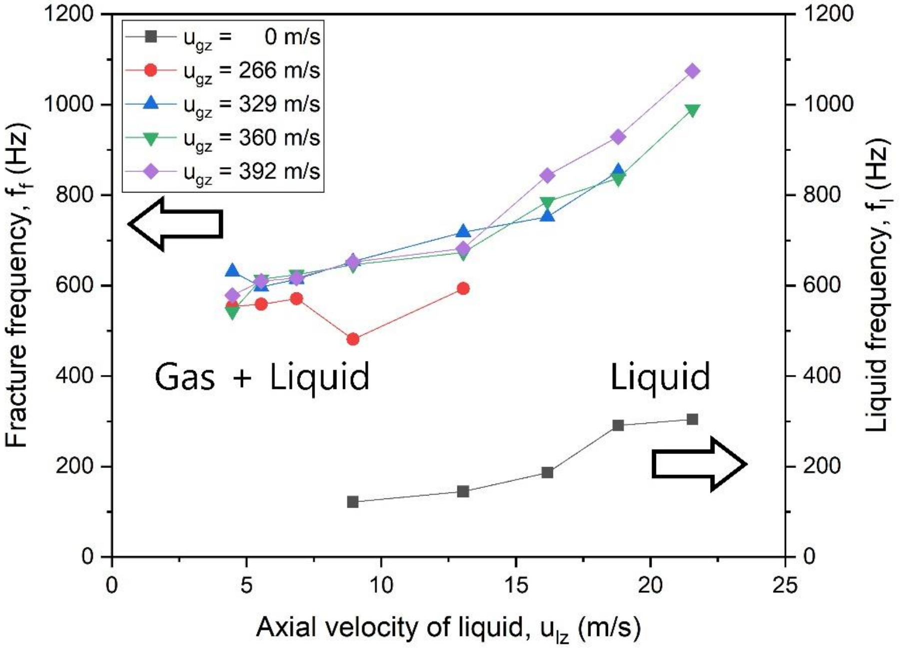

Figure 4.10 Gas frequency (f_g) and gas-liquid frequency (f_f) dependent on the axial liquid velocity.

The breakup length was dependent on the gas axial velocity rather than on the liquid velocity. Fig. 4.12 shows an image of the moment when the liquid film was ruptured. From a general point of view, it can be predicted that the impact point on the liquid film will rise due to the increase of rotational velocity as the gas axial velocity increased when the liquid velocity was constant. However, the experimental results showed that the impact point moved downwardly when the axial velocity increased.

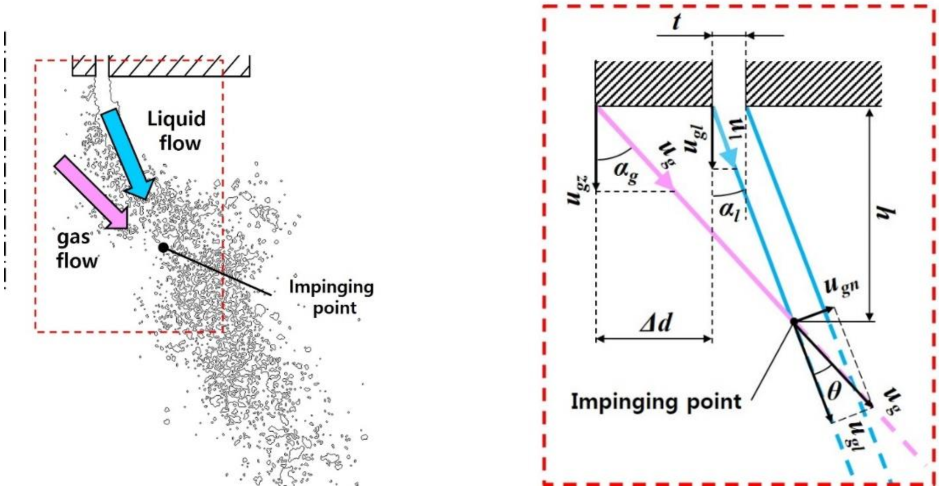

(a) (b)

Figure 4.11 (a) Longitudinal half section of spray at the moment of breakup, (b) Analytical schematic diagram of gas impingement on liquid film from injector (θ : impinging angle).

In Fig 4.13 (a), the split length (*h*) slightly changed as the axial liquid velocity increased. Instead, according to Fig 4.13 (b), the breakup length tended to increase as the axial gas velocity increased. As a result, it is shown that the breakup of the liquid film has a weak relationship with the spraying condition and physical state of the liquid, but the axial velocity of the gas flow is dominantly affected. That is, the liquid film is forcibly broken by the gas flow colliding with the liquid film, and a number of droplets were generated in this process.

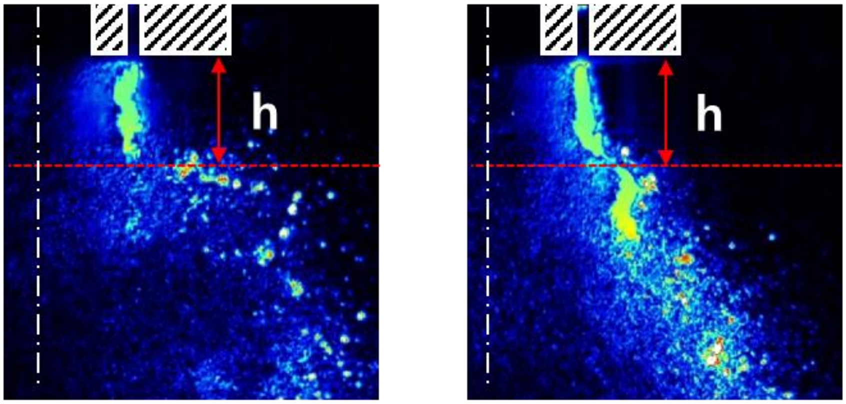

$u_{gz} = 329\,\mathrm{m/s}$, $u_{1z} = \mathbf{13\ m/s}$ $u_{gz} = 329\,\mathrm{m/s}$, $u_{1z} = \mathbf{22\ m/s}$

(a) (b)

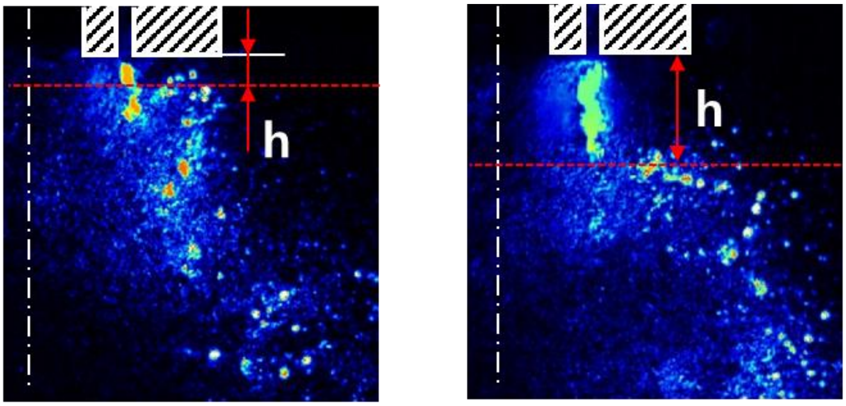

$\mathbf{u_{gz} = 139\ m/s}$, $u_{1z} = 13\ \mathrm{m/s}$ $\mathbf{u_{gz} = 329\ m/s}$, $u_{1z} = 13\ \mathrm{m/s}$

(c) (d)

Figure 4.12 Comparison of breakup length with (a-b) same axial gas velocity, and (c-d) same axial liquid velocity.

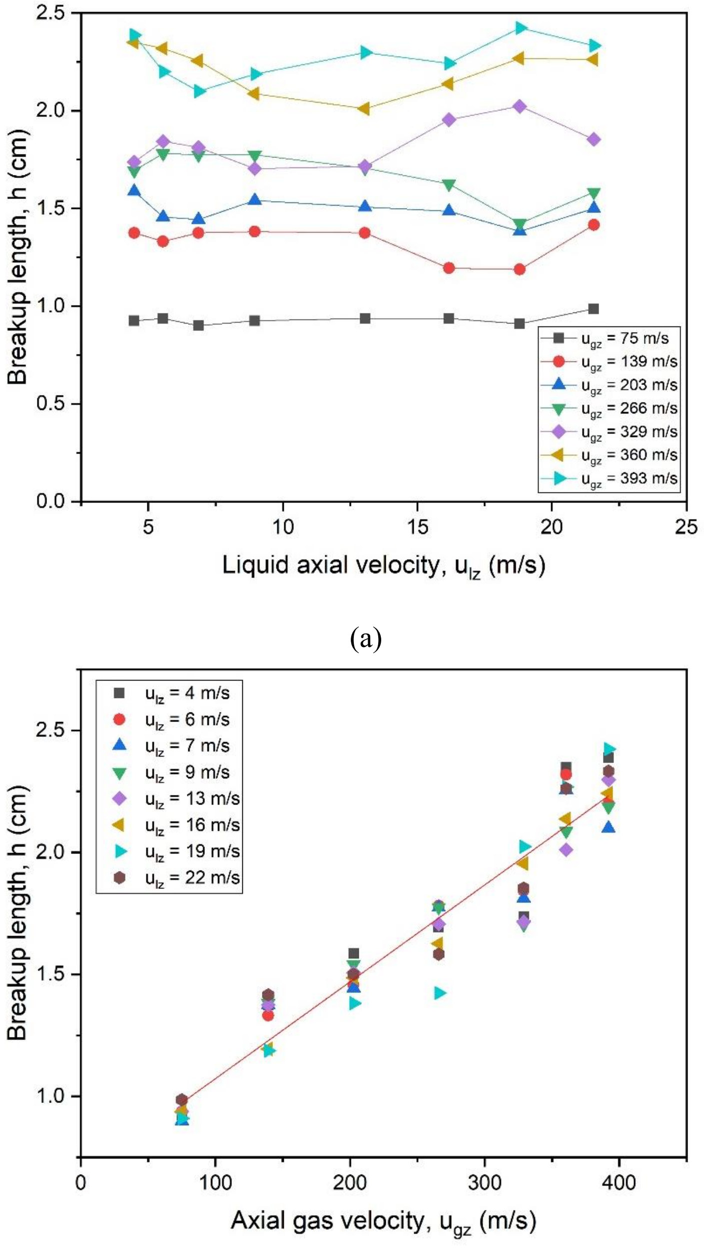

(a)

(b)

Figure 4.13 Relationship of the breakup length of liquid spray cone with axial liquid velocity (a) and axial gas velocity (b).

The gas collision model for the liquid film can be presented by changing several parameters. First, as the axial velocity of the gas increased, the impinging angle θ decreased rapidly (Fig. 4.14). According to Fig. 4.15, as the axial velocity of the gas increased, the normal vector of the gas flow to the liquid also increased linearly. The schematic diagram reflecting these results is shown in Fig 4.16. As the axial velocity increased, the normal velocity vector increased and the impinging angle decreased, so the impinging point moved downwardly. Also, as the axial velocity increased, the normal velocity vector decreased and the collision angle increased, so the impinging point moves upwardly. It was confirmed that, the turbulence cone expanded in the upper radial direction as the velocity of the gas decreased in the images taken with a digital camera.

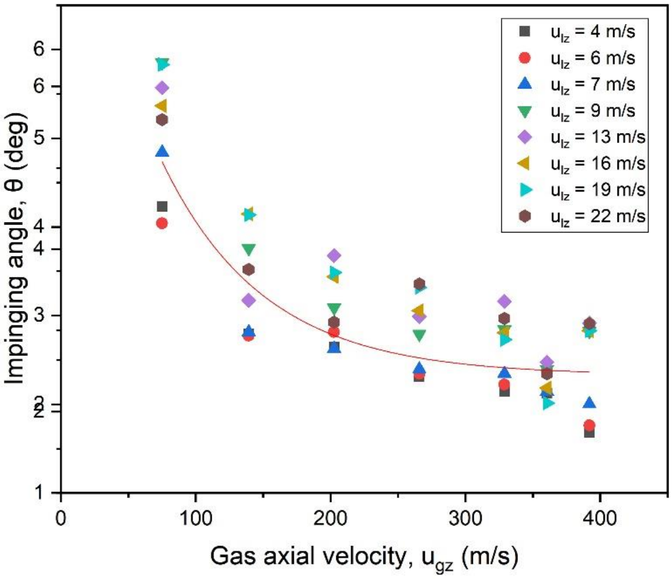

Figure 4.14 Relationship between impinging angle and axial velocity of gas.

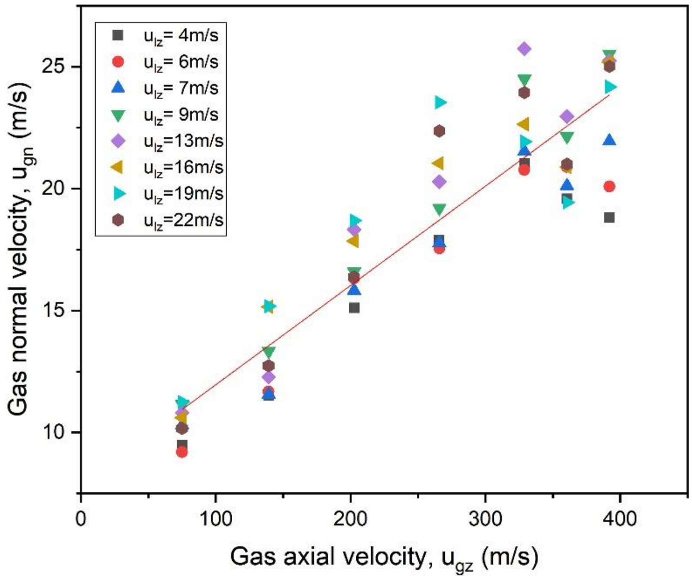

Figure 4.15 Relationship with normal velocity and axial velocity of gas flow.

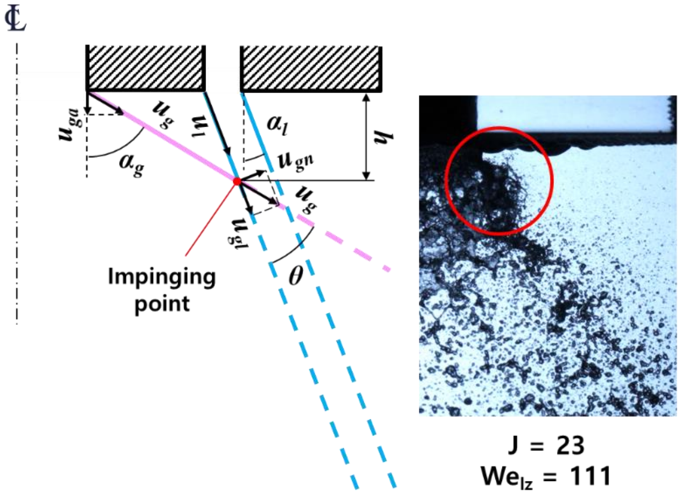

(a)

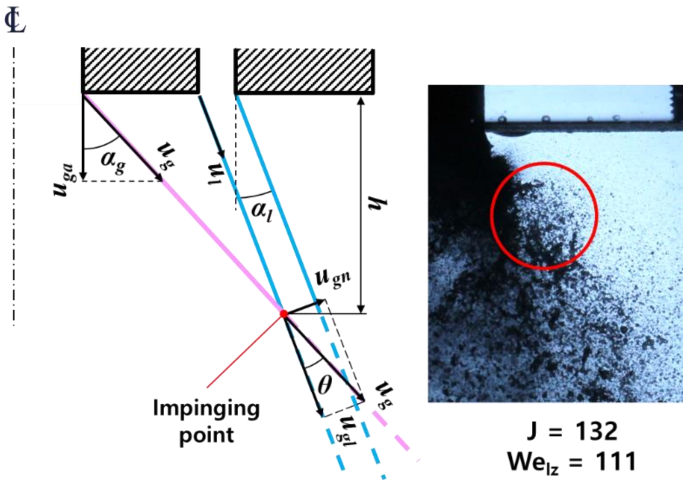

(b)

Figure 4.16 Schematics of gas flow impingement on the liquid film with higher axial.

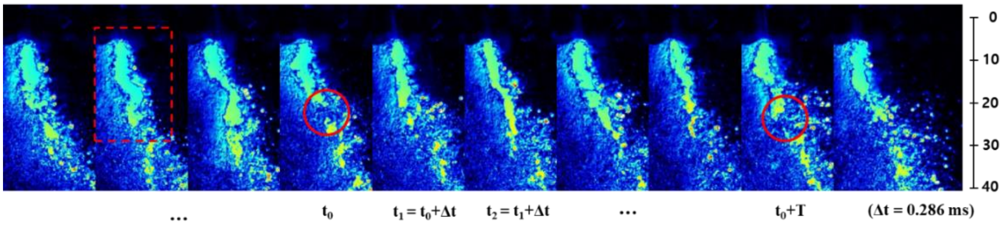

(a)

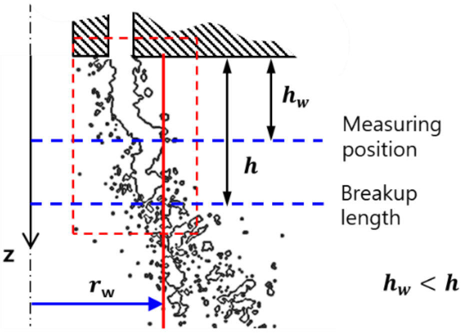

(b)

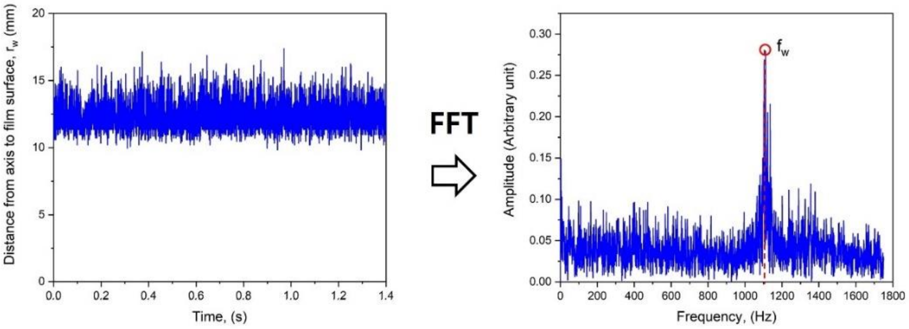

(c)

Figure 4.17 Measurement of wave frequency of gas-liquid spray: (a) time-continuous vibration and disruption of the liquid film, (b) measurement location on the liquid film, and (c) Frequency acquisition through FFT method.

Through the analysis of the continuous liquid film image as shown in Fig. 4.17 (a), it can be seen that the liquid film was regrown after breakup. In addition, the liquid film vibrated in and out of the spray cone, before being crushed by gas flow. The vibration of the liquid film can be determined by the change in the position (r_w) of the liquid film surface over time [Fig. 4.17 (b)]. The frequency of this wave was measured above the breakup position as shown in Fig 4.17 (c).

A liquid film wave caused by Plateau–Rayleigh instability exists, but the amplitude was very small near the injector outlet in the absence of gas flow. Therefore, it can be said that these waves were also influenced by gas flow. high-speed gas oscillation means that the pressure distribution of the gas stream changed. The periodic pressure change caused a dynamic entrainment effect. The decrease in the pressure inside the liquid spray cone attracted the liquid film to the spray center. If this attraction varied with time, the liquid film vibrated. Since the liquid continuously travels in the axial direction, these vibrations appeared as the surface waves. However, it was impossible for every gas pressure fluctuation to directly correspond to the vibration of the liquid film since the liquid film didn't exist in all directions in the traveling direction of the gas. This is similar to the process before separation of the liquid film in the jet in cross flow with high gas velocity, but the wave of the liquid film cannot be clearly revealed visually since the liquid film had rotational movement. Therefore, the wave frequency (f_w) has a narrow Gaussian distribution as shown in Fig 4.17(c).

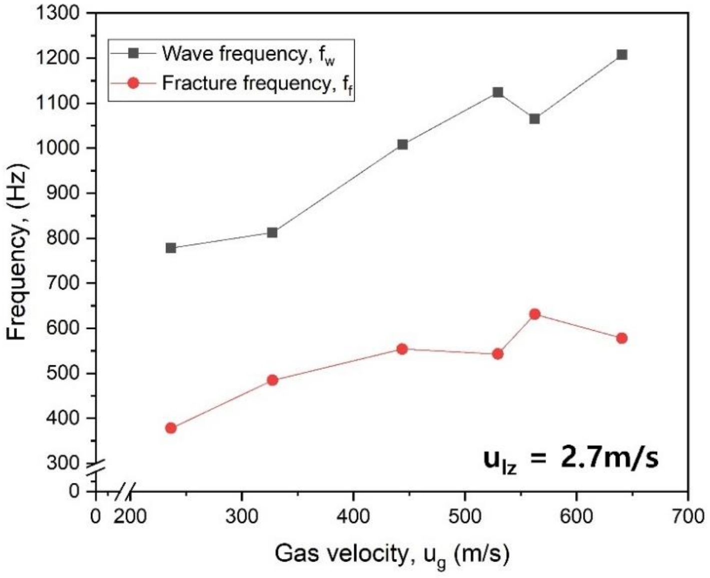

(a)

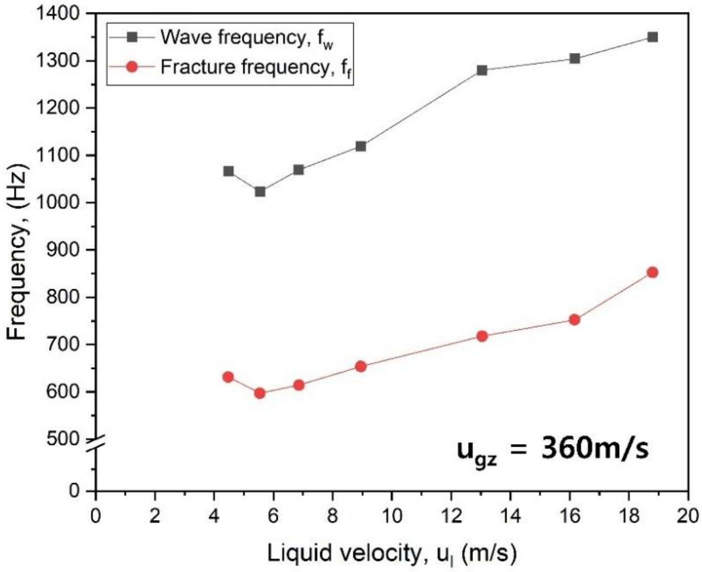

(b)

Figure 4.18 Wave frequency and fracture frequency depending on (a) the gas velocity and (b) the liquid velocity.

According to Fig. 4.18, the wave frequency of the liquid film surface increased when the axial velocity of the liquid is constant [Fig 4.18 (a)] and when the axial velocity of the gas is constant [Fig 4.18 (b)]. This is similar to the outline of the fracture frequency. As shown in Fig 4.17 (a), the liquid film breakup and droplet generation followed after the liquid film wave. The frequency ratio ($n = f_w/f_f$) was between 1.4 and 2.2, and it can be seen that most of the values were near 1.8 in the histogram shown in Fig. 4.19. In other words, it was found that the liquid film wave frequency was approximately 1.8 times larger. Therefore, it can be said that the fracture frequency was shifted from the wave frequency with a difference of several hundred Hertz. Therefore, it is possible that the frequency gradually decreased from the frequency of pressure oscillation of the gas flow, leading to the liquid film wave and then the fractural breakup of the liquid film.

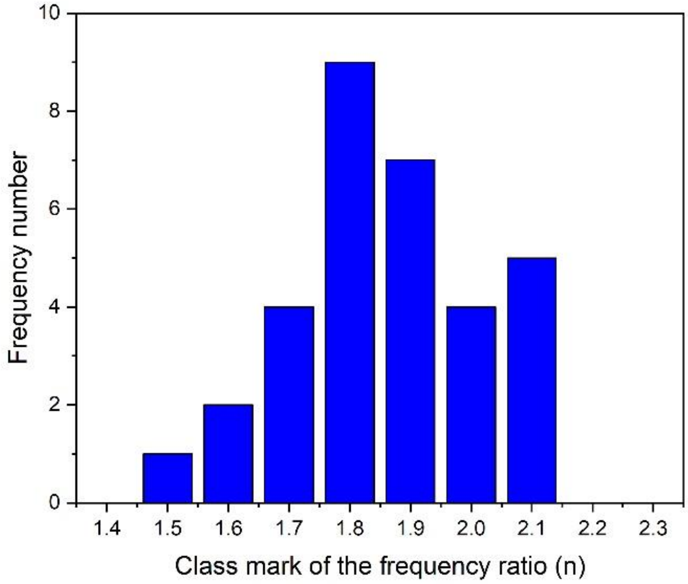

Figure 4.19 Histogram of frequency ratio *n*.

According to Andreev et al. (1991) and Knysh et al. (1982), the pressure around the axis of a fast-rotating gas, discharged through the cylindrical outlet of a single gas swirl injector with tangential inlets, is less than the ambient pressure. Therefore, the vortex structure is damaged by the surrounding gas which flows toward the nozzle of the injector, so that the pressure distribution is periodically flattened [Andreev et al. (1991) and Knysh et al. (1982)].

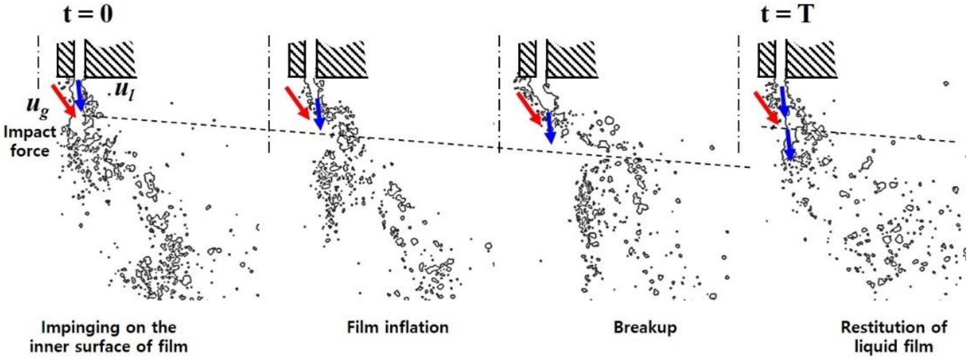

Figure 4.20 Periodical film restitution.

Periodic liquid film breakup was observed from the spray images arranged over time (see Fig. 4.20). In the absence of the effect from gas, the decomposition of the liquid film occurred at a considerably lower position. When the gas flow affects the root of the unbroken liquid film, the liquid film inflated outwardly. When the gas penetrated the swollen liquid film, the liquid film was divided into upper and lower parts. At the same time, the generation of a large number of small droplets was accompanied. The decomposed liquid film was scattered downwardly in the radial direction. Before the next impingement, the intact liquid film pushed down by the axial liquid velocity, and then the breakup occurred again. In this process, it is obvious that the ejection of droplets from the original liquid cone is the effect of the impact force caused by the velocity vector perpendicular to the liquid flow.

CHAPTER 5

DYNAMIC CHARACTERISTICS OF EXTERNAL MIXING TYPE SPRAY

5.1 Factors Affecting Spray Oscillation

According to Less et al. (1986), the wave frequency of the liquid column in the crossflow is proportional to the gas impinging velocity, and the fracture frequency of the jet is related to the wave frequency propagating along the initial jet column. In addition, the frequency is proportional to the liquid velocity Lefebvre (2010) stated that the drag coefficient of a liquid is inversely proportional to the Weber number. In conclusion, the periodicity that appears when the liquid flow breaks up by the gas flow is related to the required time for the liquid film to break up. It can be said that the shape is somewhat different from the jet in crossflow since the periodic turbulent vortex flow impinges on the liquid film in the external mixing spray, but physical similarity is expected yet.

To compare the effects of gas impinging velocity and liquid velocity on the periodicity of the liquid film fracture, three cases are presented as shown in Tab. 5.1. Case *A* and case *B* have the same axial liquid velocity, but case *B* had larger the impact gas velocity. Case *B* and case *C* have the same impact velocity of gas, but the axial liquid velocity of case C is higher than that of case *B*. The right half part of the spray for cases A, B and C is presented in Fig 5.1. It is possible to understand the pattern of periodic liquid film breakup from sequentially arranged instantaneous images. The time interval between adjacent images is 0.286ms, and the period was 2.36ms, 1.53ms, 1.06ms, respectively. When the gas flow collided with the liquid film, the liquid film was separated into upper and lower parts, and the lower part was scattered into small droplets downstream immediately after separation. In Fig. 5.1, the horizontal white line represents the lower position of the upper liquid film, and the vertical white dotted line meant just before separation. The length of the upper liquid film changed periodically. The length at the moment of breakup had a minimum value, and then the length gradually increased. It was found that the liquid film was broken after the length of the liquid film reached the maximum value.

Table 5.1. Fluid-mechanical condition of liquid and gas for case *A*, *B*, and *C*.

Spray case Parameter	case A	case B	case C
Axial gas velocity, u_{gz} (m/s)	203	361	361
Axial liquid velocity, u_{lz} (m/s)	9	9	22
Normal (impact) velocity of gas, u_{gn} (m/s)	17	22	22
Liquid Weber number, We_{lz}	289	289	1674
Gas Weber number, We_{gn}	991	1766	1766
Fracture frequency, f_f (Hz)	423	652	944

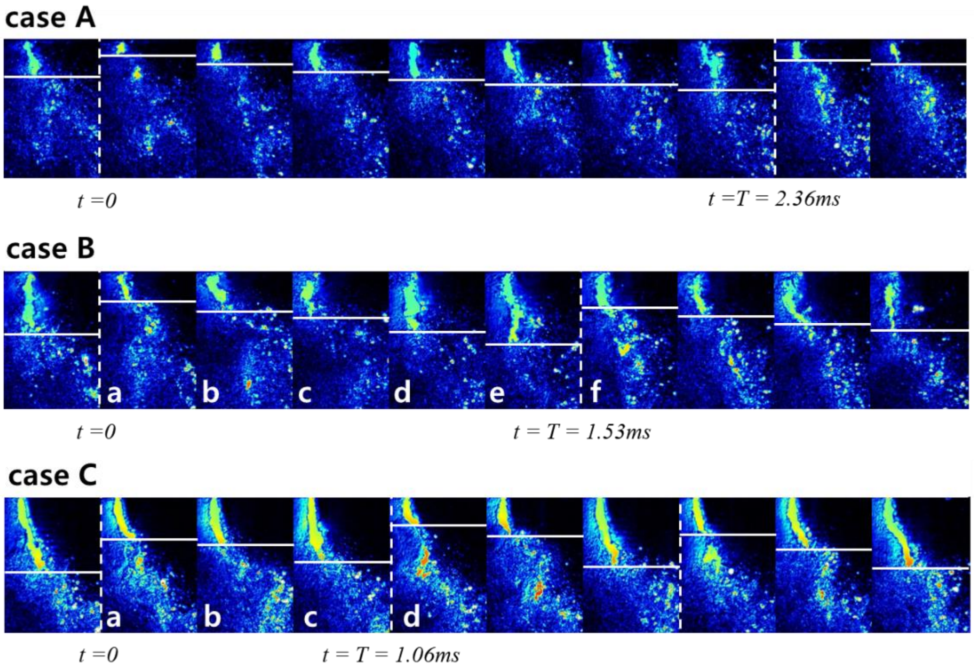

Figure 5.1 Periodic film breakup.

When the gas impinging velocity was increased under the same liquid spray condition (case A to case B), the breakup period decreased. As mentioned in the previous chapter, the impinging position of the gas flow moved in the axial direction as the axial velocity of the gas increased. This position can affect the frequency. However, as the impact position d with absolutely small value and it was a collision against a still liquid film, its effect was negligible. As the axial velocity of the gas increased, the pressure oscillation frequency also increased. When the normal velocity vector of the gas increased, the impulse to the liquid film increased. At the same time, the transmitted kinetic energy also increased since the flow rate increased. This means that the resistance time of the liquid film to gas flow was shortened. The breakup process of case *A* was morphologically similar to that of case *B*. After the liquid film was ruptured in the upper and lower parts, it was seen that the upper part was pulling into the center. However, case *B* and case *C* showed different breakup types. This was characterized by applying the same gas impact velocity to liquid films with different Liquid Weber numbers. Case *B* was a condition with a relatively low Weber number, and case *C* with an increased liquid flow rate was a condition with an increased Weber number. In the comparison of the arranged images as shown in Fig 5.1, it can be seen that the liquid film period was shorter when the liquid had high value of Weber number. The Weber number of a liquid is expressed as the ratio of the inertial force and the surface tension. It can be understood that the liquid film has a rigid property when the liquid film has a large value of Weber number.

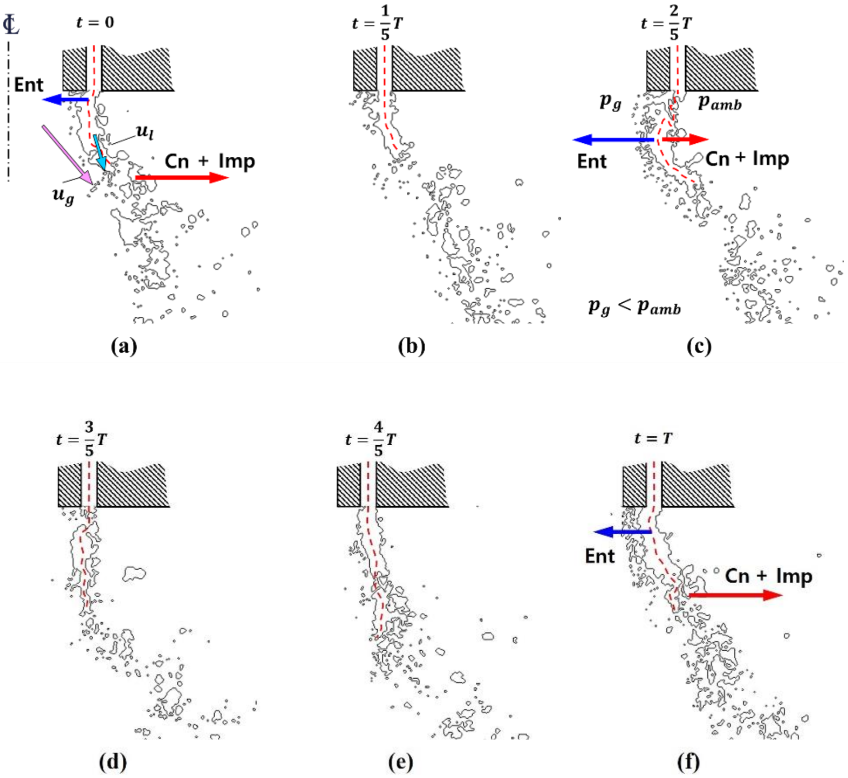

(a) (b) (c)

(d) (e) (f)

Figure 5.2 Breakup process with low liquid Weber number ($We_{lz} = 289$) – case *B*: (*Ent* – force by entrainment effect; *Cn* – centrifugal force; *Imp* – impact force; p_{amb} – ambient pressure; p_g – interspace gas pressure).

The breakup processes in both cases were explained in more detail in Figs. 5.2 and 5.3. Cases with low liquid velocities (i.e. low Weber number) were presented in Fig 5.2. As shown in Fig 5.2 (a), the inside of the upper liquid film was disturbed by the periodic perturbation of gas flow. Fig 5.2 (b) showed that the separated lower liquid film was decomposed into a smaller size, and the liquid film was still bent outwardly. At this time, the liquid film took a form of a second-class lever. That is, the root of the upper liquid film can correspond to the working point, the injector nozzle – the support point, and the lower part of the upper liquid film – the force point. In this case, the root of the liquid film approached the high-speed gas flow region and was affected by the entrainment effect ($p_g < p_{amb}$). The liquid film grew continuously and received strong attraction immediately after it was discharged from the injector outlet. Therefore, as shown in Fig 5.2 (c), the liquid film was bent severely and the inner surface was disturbed, resulting in small droplets. However, liquid had centrifugal force due to rotation in swirl liquid spray, and can be momentarily accelerated in the axial direction due to the centrifugal force of the rotating gas flow. Then, the liquid film was again unfolded in the radial direction due to the radial velocity components of the liquid and gas as shown in Fig 5.2 (d). The liquid film growing in this state was generally straight, but began to swell outwardly again [Fig 5.2 (e)]. The weakened lower part of the liquid film was separated up and down again as it burst by the impact force of the gas. This shape is presented in Fig 5.2 (f). Since the separated upper liquid film was also a second-class lever, the inside of the liquid film root was disturbed again.

However, as shown in Fig. 5.3, in the case of a large Weber number, the period decreased. First, a certain point of the liquid film was cut off by the periodic perturbation of the gas [Fig 5.3 (a)]. Since the gas escapes between the disconnected liquid films, the upper liquid film bent outwardly [Fig 5.3 (b)]. Since the liquid film was like a second-class lever, the portion adjacent to the injector outlet tends to be pushed inwardly. Therefore, liquid peeling appeared on the inner part of the upper part. In other words, there was a disturbance to the liquid film shape due to the impact force and the attractive force toward the center [Fig 5.3 (c)]. Compared to the case with the low Weber number, the film with the high Weber number did not bend inwardly. It can be considered that the liquid with a high Weber number has an increased inertial force, so it was intended to maintain the original spray cone shape. In addition, the broken upper liquid film was pushed down again and restored quickly since the liquid axial velocity increased [Fig 5.3 (d)].

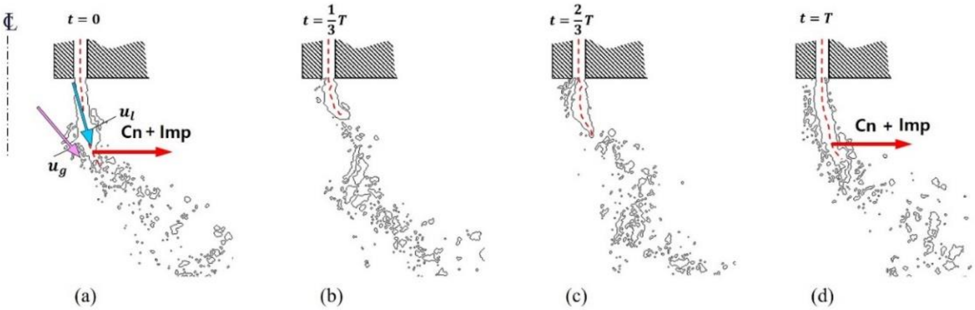

Figure 5.3 Breakup process with high liquid Weber number ($We_{lz} = 1674$) – case *C*: (*Cn* – centrifugal force; *Imp* – impact force).

It is summarized as follows based on the contents of these morphological changes. Based on the contents of these morphological changes, they are summarized as follows. According to Fig 5.4 (a), the fracture frequency tended to increase as the impact velocity increases. And as the axial velocity of the liquid increased, the fracture frequency also increased [see Fig 5.4 (b)].

Simply put, if the liquid film recovers quickly under conditions of the same impact velocity, it may collide with the gas earlier. However, the collision position always was not fixed because the gas injection angle oscillated. It should also be considered that the gas vibrated the liquid film surface. It is interesting to note that the refraction of the liquid film and the second-class lever effect due to the vibration of the surface occurred under low Weber number conditions. The film did not rupture while bending inwardly. This means that before the rupture of the liquid film, the spreading process must be preceded. It is natural that the role of the gas existed for spreading the liquid film. And it is reasonable that the energy of the gas was consumed in this process. Also, if the effective gas perturbated before the liquid film was unfolded, the liquid film might not have a breakup opportunity. This is because the frequency of the gas was remarkably greater than the frequency of rupture of the liquid film. That is, the fracture frequency decreased as the spraying conditions changed so that the refraction of the liquid film became significant.

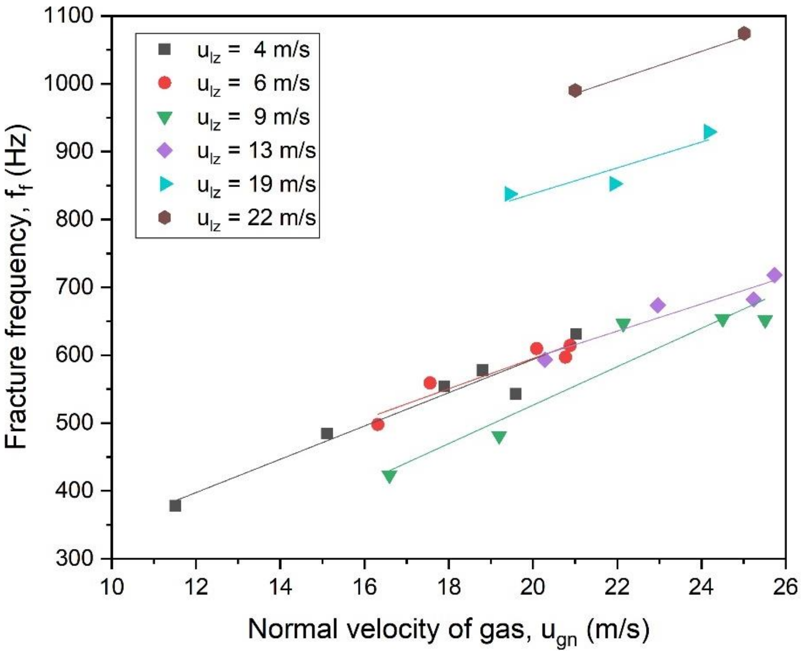

(a)

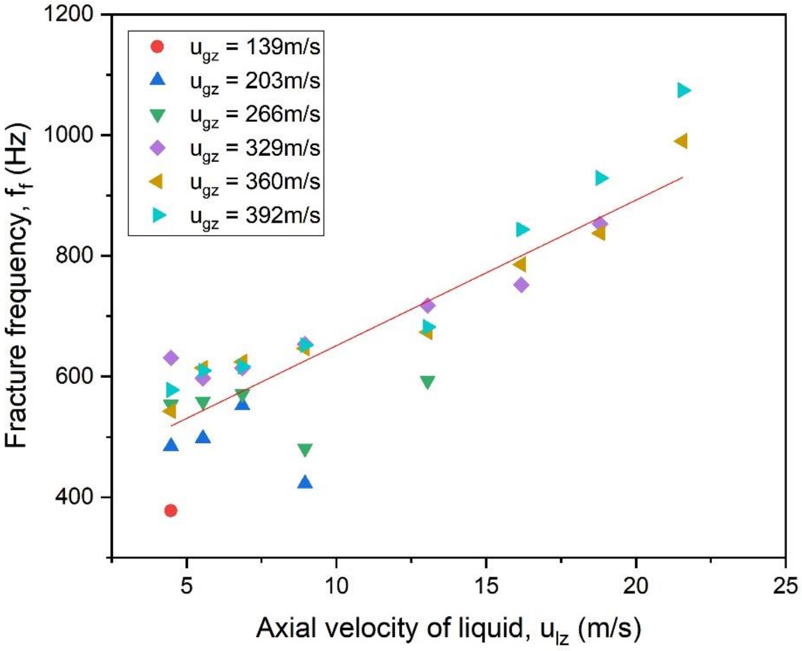

(b)

Figure 5.4 Influence of (a) gas normal velocity on the liquid film (impact velocity) and (b) liquid axial velocity on the fracture frequency.

As the Weber number increased, the liquid became insensitive due to external influences. Therefore, it can be said that the film kept straight. In this case gas perturbation could well capture an effective opportunity to strike the liquid film. If the liquid became more rigid, it would not be able to effectively break the liquid film due to lack of energy even if gas flow got a chance to impinge on film. insufficient energy of the gas for liquid breakup led to damaged regularity.

5.2 Instability Map for Frequency and Amplitude

Spray conditions that fail regular liquid film breakup are shown Fig. 5.5 in the instability map. Figure 5.5 (a) shows the distribution of fracture frequencies according to the injector supply conditions. The frequency was not detected in the lower right of the map. This means that the liquid film was broken unsuccessfully, if the gas differential pressure is smaller than the liquid differential pressure (if the gas velocity is smaller than the liquid velocity).

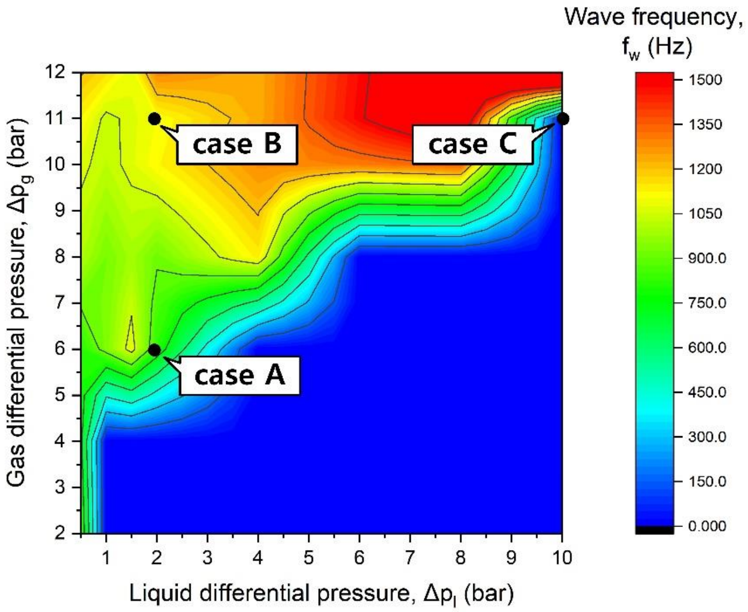

(a)

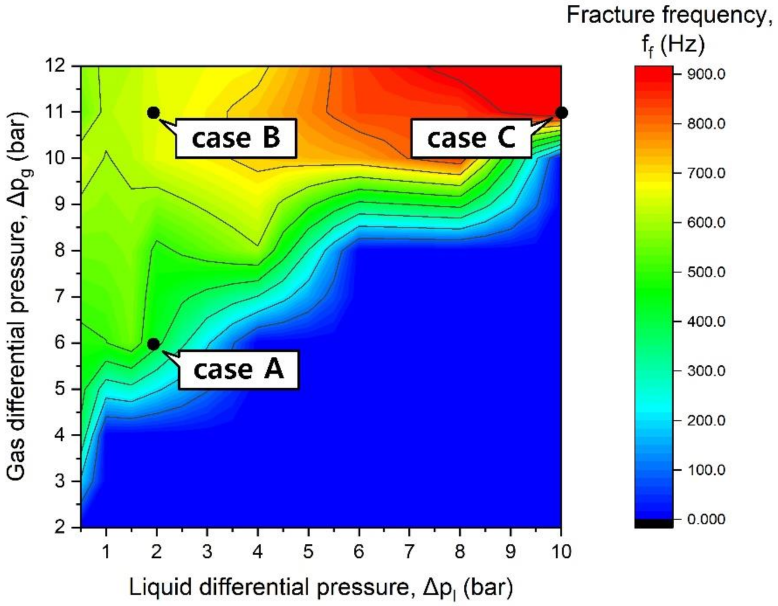

(b)

Figure 5.5 Instability map of (a) wave frequency (f_w) and (b) fracture frequency (f_f).

As mentioned in the previous chapter, gas pressure oscillation disturbed the liquid film. In this process, the frequency of the gas may be transferred to the surface vibration of the liquid film. Vibration and breakup of the liquid film cannot be regarded as separate problems. Therefore, it is obvious that the vibration of the liquid film affects the period of distribution of the droplets. The similarity between the wave frequency and the fracture frequency distribution region according to the spray conditions supported this as shown in Fig. 5.5 (a) and (b).

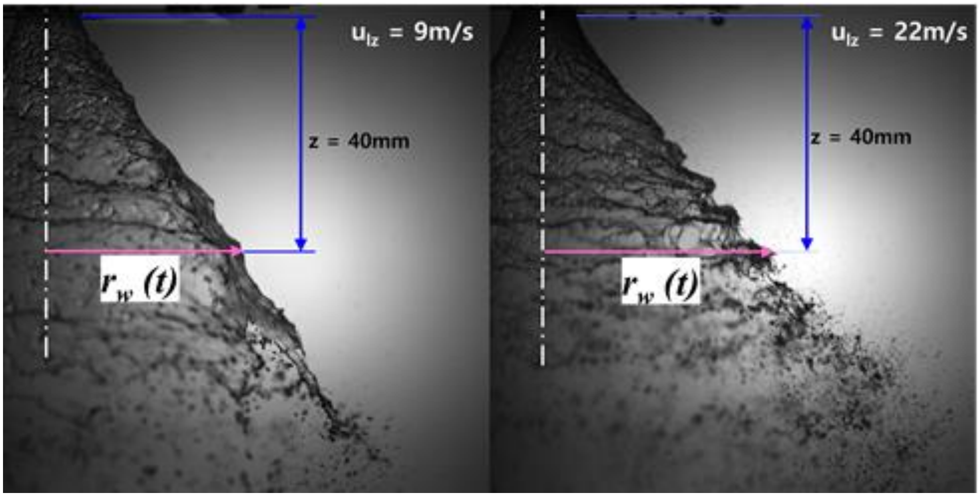

(a) (b)

Figure 5.6 Spray of liquid discharged from annular liquid injector (a) with low axial velocity (u_{lz} = 9m/s) and (a) with high axial velocity (u_{lz} = 22m/s) (distance from axis to liquid film surface).

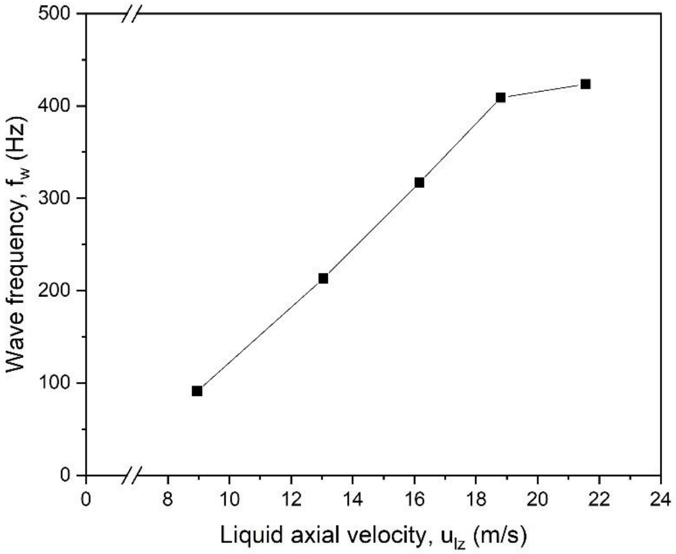

Figure 5.7 Wave velocity of liquid film without central gas stream.

In Fig 5.5 (a), the highest value was shown in the upper right. The gas pressure varied faster inside the liquid film as the pressure frequency of the gas increased. In this case, the frequency of the attractive force value due to the pressure difference between the inside and outside of the liquid film also increased. If the liquid velocity increased, it can be said that a wave caused by Plateau–Rayleigh instability had occurred. It is also known that the surface vibration of the liquid spray film of the swirl injector increased. This phenomenon was also revealed in images by using high-speed camera as seen in Fig. 5.6. The wave frequency at a distance of 40 mm from the injector in the axial direction increased (see Fig. 5.7).

In Fig 5.5 (b), the maximum point was also shown on the upper right. This means that the perturbation of the gas against the liquid film having an invariant shape has a greater probability of obtaining a successful strike, and the larger the gas impact velocity, the larger the probability of the liquid film.

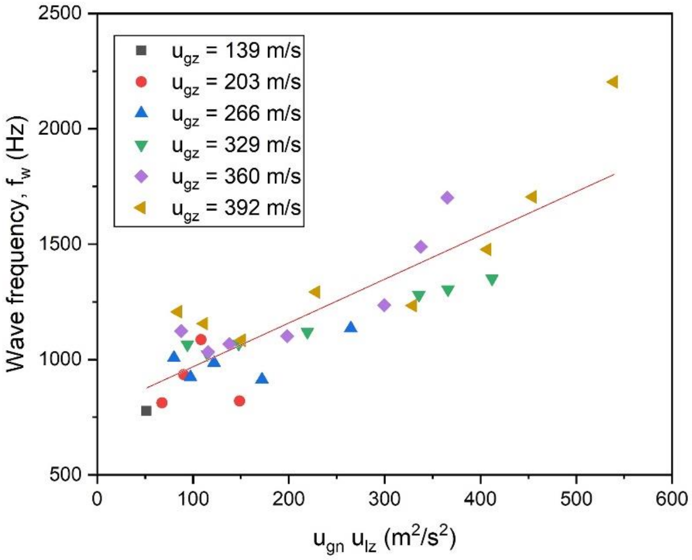

(a)

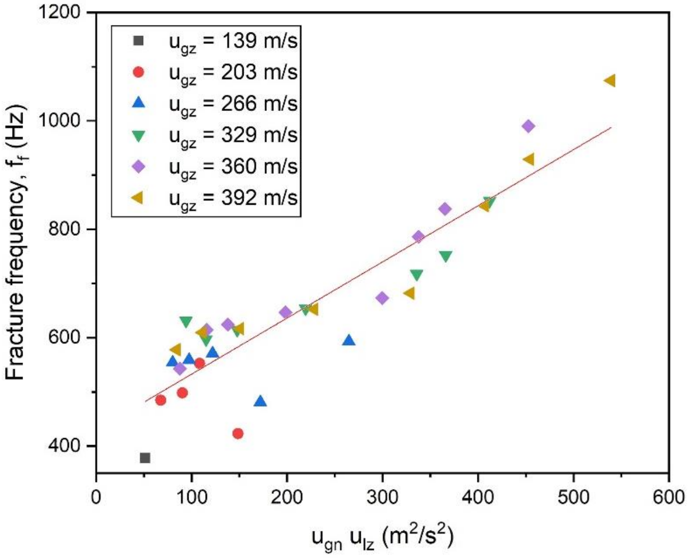

(b)

Figure 5.8 Empirical model of (a) wave frequency (R^2=0.73) and (b) fracture frequency (R^2=0.81).

It revealed that the impact velocity of the gas (normal velocity) and the axial velocity of the liquid affected the frequency. The empirical model of wave frequency and fracture frequency can be presented linearly as shown in Fig. 5.8. The coefficient of determination (R^2) is all over 0.6, so the significance of the model was sufficient. In Fig. 5.8, it was shown that the frequency tended to decrease as the axial velocity of the gas decreased. In the previous chapter, it was mentioned that the impinging position of the gas was dependent on the axial velocity of the gas flow. That is, the frequency somewhat decreased as the impinging position rose upwardly. However, it cannot be concluded that the impact position dominated the frequency, since the frequency have a linear characteristic.

However, in the condition of high liquid differential pressure, the frequency decreased sharply as the gas differential pressure decreased. If the gas had a small differential pressure value, the number of chances to break the liquid film up could be reduced under high Weber number condition. This can be verified that the portion occupied by the blue part in Fig. 4.7 (a) increased as the liquid differential pressure increased. Fig. 4.11 shows a map of the amplitude dependent on the injector supply condition. Similar to the frequency characteristics, it appeared very low amplitude at the bottom right position. The maximum value of the amplitude values is shown in the upper left corner.

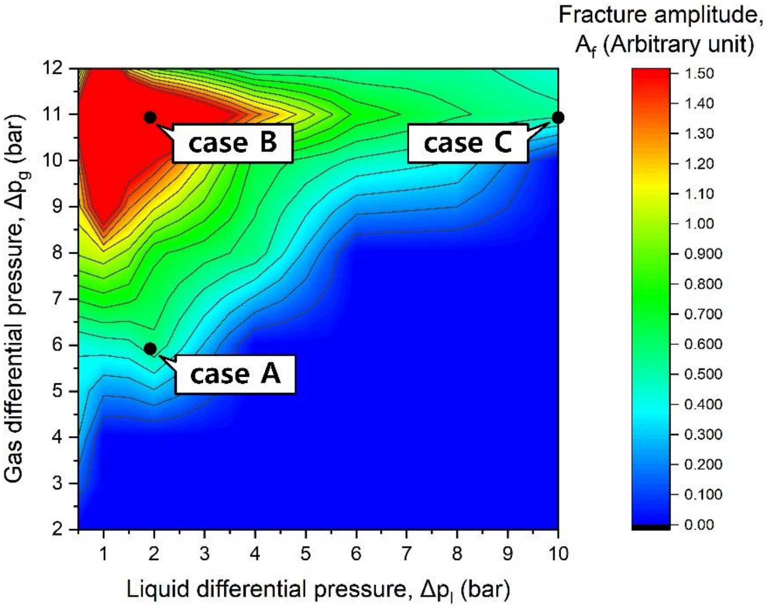

Figure 5.9 Instability map relating to the liquid breakup fracture amplitude.

This can be explained as shown in Fig. 4.12. In the case *B* with the highest amplitude, it has the largest ratio of the gas differential pressure to the liquid differential pressure. When the gas hits the liquid film, the upper part ① is bent and shriveled, but the lower part ② is bent outwardly by the gas impact. As a result of this effect, the amplitude was increased due to the liquid film separated quite clearly. In case *A*, bag-type droplet generation [Azzopardi (1997)] was remarkable due to the low Weber number. When the liquid film swelled and then burst, droplets were generated. Therefore, the boundary was blurred due to a number of liquid fragments generated between the separated liquid film and ligaments. The separation boundary is also not so clear when strong gas flow tore film under high Weber number conditions *C*, as a large amount of fine droplets is generated.

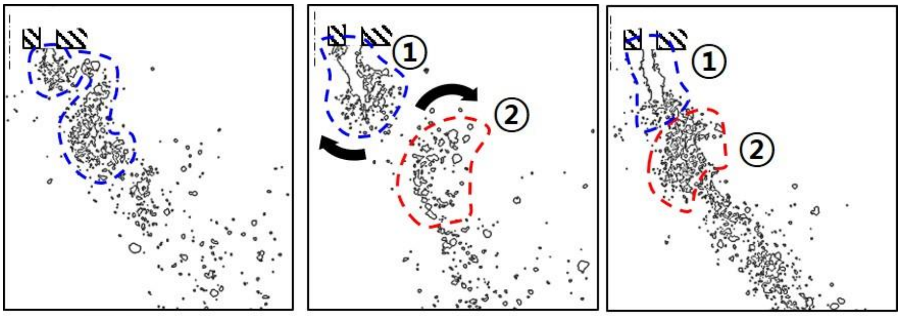

case *A* case *B* case *C*

Figure 5.10 Film breakup process (①: Upper part of the liquid film; ②: Lower part of the liquid film; case *A*: Low-amplitude region (wave-like bag type atomization); case *B*: High-amplitude region; case *C*: Low-amplitude region (film cutting)).

According to Bazarov et al. [4], the liquid-gas velocity ratio can be used to describe the dynamics of a gas-liquid injector. It is reasonable that the normal vector component of the gas is related to the separation of the liquid film.

It was found that the maximum value of the fracture frequency [Fig. 5.5(b)] and that of the fracture amplitude (Fig. 5.9) located on the different position on the map. It cannot be said to be a meaningful model since the R^2 values of the fitting lines in Fig 5.12 are all less than 0.6, but it is considered to be sufficient to show the tendency. In general, as the dynamic pressure ratio ($\bar{q} = \rho_l u_l^2 / \rho_g u_{gn}^2$) increased, the amplitude decreased as shown in Fig 5.12(b). It can be said that the effect of the liquid velocity on the amplitude is in contrast to the effect on the frequency [Fig. 5.1(a)].

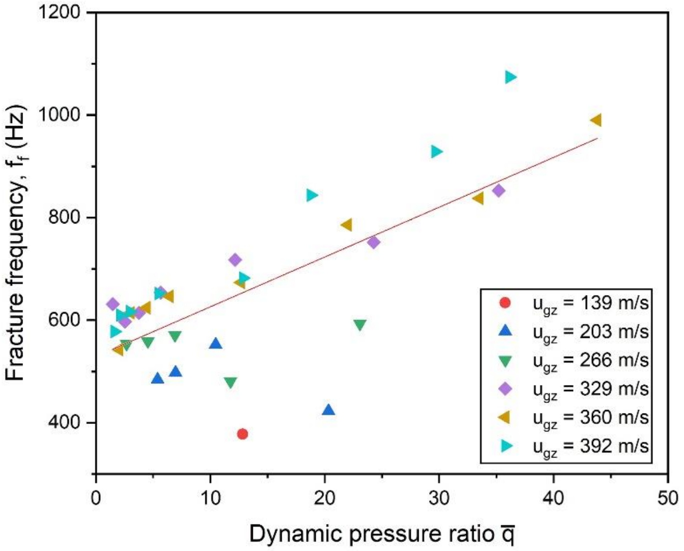

(a)

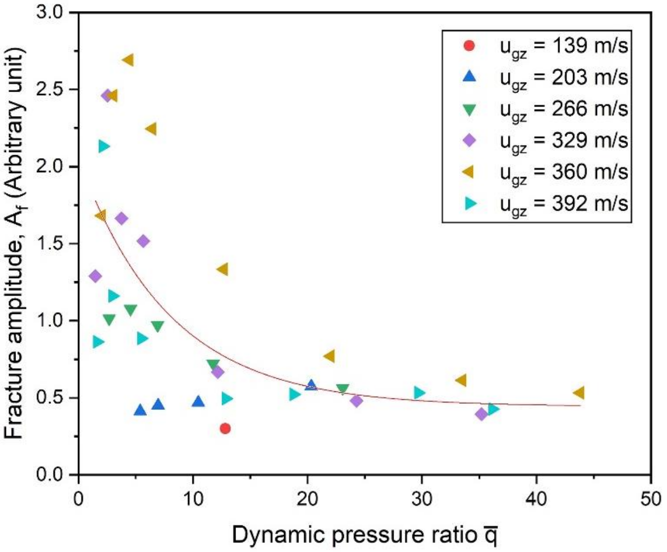

(b)

Figure 5.11 (a) fracture frequency, (b) fracture amplitude depending on the dynamic pressure ratio.

CHAPTER 6

CONCLUSION

Internal and external mixing type injectors used to figure out spray characteristics depending on the impingement position of the gas flow discharged from the swirl injector. In this study, general spray pattern was analyzed by using imaged taken by digital camera. But a large number of fine droplets and liquid ligaments created by turbulent gas vortex flow blocked the view for understanding of spray. In this reason the longitudinal section images were acquired by the principle of Mie scattering. And 2p-SLIPI technique was used to reveal droplets by eliminating multiple scattering signals. Since a piercing shriek occurred when the gas flow went out of the injector nozzle, the acoustic frequency of the gas was measured by dynamic pressure sensor and FFT method. As the droplet distribution varied over time, the wave frequency of liquid film and the fracture frequency were also obtained from instantaneous images by analyzing with FFT method.

Small differences in injector dimensions led to significant differences in spray shape and atomization mechanism. The gas flow from the swirl injector pushed the liquid flow and attracted it to the center by the entrainment effect. In the internal mixing type of spray, the recessed region somewhat hindered gas flow from pushing the liquid film outwardly. Therefore, the gas mainly scraped the inside of the liquid film and generating fine droplets. In this reason, the mist zone was developed in the axial direction. But in the external mixing type, the gas penetrated the liquid film breaking it up to create droplets. Fast gas vortex entrained droplets to the center, but there was no independent mist cone because the liquid spray angle was smaller than that of the gas flow. And it seemed that the droplets clusters were distributed linearly forming spray cone.

In this fractural breakup process, droplets occurred abruptly and periodically. It was found that the breakup length of the liquid film was dependent on the gas injection characteristics, not the liquid atomization characteristics. And the swirling gas flow discharged from the tube generated high-frequency acoustic noise. In addition, film was vibrating with frequency lower than gas oscillation frequency. Therefore, it is reasonable to understand that the pressure oscillation of gas caused periodical attraction force to the liquid film, and this film wave and gas impingement induced film breakup with fracture frequency. It is expected that the discontinuous droplet distribution leads to the flow rate oscillation.

It is obvious that the gas oscillation contributed to fracture frequency, since the frequency did not appear when the gas had low energy. Also, in general, the fracture frequency was proportional to the gas impinging (normal) velocity. It means that liquid film decomposed earlier as the gas impinged with larger velocity. And the frequency was increased as the liquid Weber number increased. It can be said that the gas did not miss effective opportunity to breakup as the rigid liquid film did not flutter, and the liquid film restituted faster with high velocity. Consequently, fracture frequency is related with the aerodynamic force by the gas flow and the aerodynamic drag force of the liquid film.

REFERENCES

1. Aigner, M., & Wittig, S. Performance and optimization of an air-blast nozzle: Drop size distribution and volumetric air flow. *Intl. J. of Turbo & Jet-Engines*, vol.4, 1987, pp.75-80.

2. Aigner, M., & Wittig, S. Swirl and counter swirl effects in prefilming air-blast atomizers. *ASME*, 1988, vol.110.

3. Alpatov, A. V. *Propulsion Systems and Energy Systems: Lecture Course* (in Russian). Alexander Mozhaysky Military Space Academy, St Petersburg, Russia, 2007.
4. Andrea, H.*et al.*, Aerosols–Dusts, Fumes and Mists [MAK Value Documentation, 1999]. *The MAK Collection for Occupational Health and Safety,* 2012, pp.271-278.
5. Andreev, A. V., Bazarov, V. G., Grigor'ev, S. S., Dushkin, A. L., Lyulka, L. A. *Dynamics of gas-liquid injectors* (in Russian), Mashinostroenie, Moscow, 1991.

6. Andreev E. A., Novikov A.V., Shatsky O. E. Computational and experimental study of the reliability of starting and reaching the mode of a low-thrust rocket engine using gaseous components oxygen + methane with electric spark ignition (in Russian). *Engineering Journal: Science and Innovation*, 2017, Vol.64, no.4.
7. Andreev, Yu. Z. *Study of the dependences of the characteristics of a small-size liquid rocket engine with a thrust of 50...400N on propellant of NTO + UDMH on the main parameters of a two-component coaxial swirl injectors and film cooling jet injectors* (in Russian), Ph.D thesis, Roscosmos, Nidjnyaya Salda, Russia, 2005.

8. Arsentiev, V. V., *Dual liquid swirl injectors of liquid rocket engine* (in Russian), Russia, 1972.

9. Azzopardi, B. J. Drops in annular two-phase flow. *Int'l J. of Multiphase Flow*,

1997, Vol.23, no.7, pp.1-53.

10. Batarseh, F. Z., Roisman, I. V., & Tropea, C. Spray generated by an air-blast atomizer at high-pressure conditions. *In Turbo Expo: Power for Land, Sea, and Air*, 2009, vol.47918, pp. 619-627.
11. Bazarov, V. G., & Yang, V. Liquid-propellant rocket engine injector dynamics. *Journal of Propulsion and Power*, 1998, Vol.14, no.5, pp.797-806.
12. Berrocal, E., Kristensson, E., Richter, M., Linne, M., & Aldén, M. Application of Structured Illumination for Multiple Scattering Suppression in Planar Laser Imaging of Dense Sprays. *Opt.Express*, 2008, Vol.16, no.22, pp.17870–17881.
13. Berrocal, E., Structured Laser Illumination Planar Imaging: New horizons for the study of spray dynamics, thermometry and droplet sizing. *18th ILASS*, Lisbon, 2016.
14. Bohren, C. and Human, D. *Absorption and Scattering of Light by Small Particles*. Wiley-VCH, 1983.
15. Chanaud, R. C. Observations of oscillatory motion in certain swirling flows. *Journal of Fluid Mechanics*, 1965, Vol.21, no.1, pp.111-127.
16. Chanaud, R. C., Experiments concerning the vortex whistle. *J. Acoust. Soc. America*, 1963, Vol.35, no.7
17. Clark, C. J., & Dombrowski, N. Aerodynamic instability and disintegration of inviscid liquid sheets. *Proceedings of the Royal Society of London. A. Mathematical and Physical Sciences*, 1972, Vol.329, no.1579, pp.467-478.
18. Dranovsky, M. L. *Combustion instabilities in liquid rocket engines: testing and development practices in Russia*. AIAA, 2007.
19. Dityakin, Yu. F., Klyachko, L. A., Novikov, B. V., Yagodkin, V. I. *Liquid atomization* (in Russian), 2nd Ed., Mashinnostroeine, Moscow, 1977.
20. Egorychev, V. S. *Calculation and design of mixing process in liquid rocket*

engine chamber (in Russian). Publishing house of SSAU, Samara, Russia, 2011.

21. Farago, Z., and Chigier, N. Morphological Classification of Disintegration of Round Liquid Jets, *Atomization and Sprays*, 1992, Vol.2, no.2, pp.137–153.
22. Fraser, R. P., Dombrowski, N., & Routley, J. H. The atomization of a liquid sheet by an impinging air stream. *Chemical Engineering Science*, 1963, Vol.18, no.6, pp.339-353.
23. Fu, Q. F., Yang, L. J., & Wang, X. D. Theoretical and experimental study of the dynamics of a liquid swirl injector. *Journal of Propulsion and Power*, 2010, Vol.26, no.1, pp. 94-101.
24. GOST 21980-76, *Gas centrifugal burners with tangential inlet basic indexes nomenklature and methods of computation* (in Russian), IPK Izdatelstvo Standartov, Moscow, Russia, 2003
25. Gill, G. S., Nurick, W. H. *Liquid rocket engine injectors (NASA SP-8089)*, NASA, Virginia, 1976.
26. Hahn, D. W. *Light scattering theory*. Dept. of Mechanical and Aerospace Engineering, University of Florida, 2009.
27. Im, J. H., Cho, S., Yoon, Y., & Moon, I. Comparative Study of Spray Characteristics of Gas-centered and Liquid-centered Swirl Coaxial Injectors. *J. Propul. Power*, 2010, Vol.26, no.6, pp.1196–1204.
28. Im, J. H., Kim, D., Han, P., Yoon, Y., & Bazarov, V., Self-pulsation characteristics of a gas-liquid swirl coaxial injector. *Atomization and Sprays*, 2009, Vol.19, no.1.
29. Ingebo, R. D. Penetration of drops into high-velocity airstreams, *National Aeronautics and Space Administration*, 1967.
30. Jeong K., *Spray characteristics of impinging type injectors for liquid rocket engines*. Ph.D. Thesis, Seoul Nat'l Univ., 2004.

31. Jeong, G., Lee, Y., Yoon, J., Yoon, Y. Spray Characteristics of Gas-Liquid Coaxial Swirl Injectors by Mixing Method. *KSAS 2019 Fall Conference*, 2019.
32. Jeong, G., Lee, Y., Yoon, Y. Mist Formation of Gas Liquid Coaxial Injectors for Small size Rocket Engine, ILASS-Asia 2019, *20th Annual Conference on Liquid Atomization and Spray Systems*, Ube, Japan, December 21–23, 2019.
33. Jeong, G., Lee, Y., Yoon, J., Jo, H., Yoon, Y. Atomization and Distribution of Droplets in Gas-Liquid Sprays by Coaxial Swirl Injectors. *Atomization and Sprays*, 2020, Vol.30, no.8, pp.607-626.
34. Jeong, S., *Effect of self-oscillation on dynamic characteristics of a closed-type swirl injector*, Ph.D. Thesis, Seoul Nat'l Univ., Seoul, Korea, 2020.
35. Kang, Z., Li, Q., Zhang, J., & Cheng, P. Effects of gas liquid ratio on the atomization characteristics of gas-liquid swirl coaxial injectors. *Acta Astronaut.*, 2018, Vol.146, pp.24–32.
36. Kim, D., Han, P., Im, J. H., Yoon, Y., & Bazarov, V. G. Effect of recess on the spray characteristics of liquid-liquid swirl coaxial injectors. *J. Propul. Power*, 2007, Vol.23, no.6, pp.1194–1203.
37. Kim, I. G., and Lee, S. Y., A simple technique for sizing and counting spray drops using digital image processing. *Exp. Therm. Fluid Sci.,* 1990, Vol.3, no.2, pp.214–221.
38. Kim, H., Kang, H., & Kwon, S. A feasibility study of using pintle injector as sole-throttling device for shallow throttling condition. *Acta Astronautica*, 2020, Vol.167, pp.272–279.
39. Kim, S., Khil, T., Kim, D., & Yoon, Y. Effect of geometric parameters on the liquid film thickness and air core formation in a swirl injector. *Measurement Science and Technology*, 2010, Vol.21, no.3.
40. Kirpichev, M. I. *Mathematical and experimental modeling of heat and mass transfer in the channels of combustion chambers of power plants* (in Russian), Ph.D. Thesis, Voronezh State Tech. Univ., Voronezh, Russia, 2001.

41. Knysh, O. Yu., *Study of self-oscillatory processes in centrifugal injectors of aircraft gas turbine engines* (in Russian), Ph. D thesis, SSAU, Samara, Russia, 1999.
42. Knysh, Yu. A., and Lukachev, S. V. Experimental study of a vortex sound generator (in Russian), *Akustichesky Jurnal*, 1977, Vol.23, no.5, pp.776-782.
43. Knysh, Yu. A., Uryvsky, A. F. On the theory of the occurrence of regular pulsations in a swirling fluid flow (in Russian). *Izvestiya buzov "Aviation technique"*, 1982, no.1, pp.13-19.
44. Kozlov, A. A., Suvorov V. A., Shtekher M. C. *Lecture notes for the course "Propellants and working fluids", part 1* (in Russian). MAI, Moscow, 1977.
45. Kristensson E., *Structured laser illumination planar imaging SLIPI application for spray diagnostics*, Ph. D thesis, Lund Univ., 2012.
46. Kristensson, E., Berrocal, E., & Aldén, M. Two-pulse structured illumination imaging. *Optics letters*, 2014, Vol.39, no.9, pp.2584-2587.
47. Kochanov, A. V., Klimenko, A. G., Rebrov, S. G. Influence of the fuel ignition mechanism by a spark and a heated surface on the starting of a low-thrust oxygen-hydrogen rocket engine (in Russian). *Bulletin of the Moscow State Technical University-Series "Mechanical Engineering"*, 2017, Vol.114, no.3.
48. Kulkarni, V., Sivakumar, D., Oommen, C., & Tharakan, T. J. Liquid Sheet Breakup in Gas-centered Swirl Coaxial Atomizers. *J. Fluids Eng.*, 2010, Vol.132, no.1.
49. Kurpatenkov, V. D., Kesaev, Kh. V. *Calculation of engine injectors* (in Russian). Moscow Aviation Institute, Moscow, USSR, 1987.
50. Lee, Y. *Effects of Lip Thickness and Recess Length on Spray Characteristics in Gas Centered Double Swirl Injector for 400N Methane Rocket Engine*, Master Thesis, Seoul Nat'l Univ., 2019.
51. Lee, C. H., & Reitz, R. D. An experimental study of the effect of gas density on

the distortion and breakup mechanism of drops in high speed gas stream. *Int. J. Multiph. Flow*, 2000, Vol.26, no.2, pp.229–244.

52. Lee, E. J., Oh, S. Y., Kim, H. Y., James, S. C., & Yoon, S. S. Measuring air core characteristics of a pressure-swirl atomizer via a transparent acrylic nozzle at various Reynolds numbers. *Exp.Therm.Fluid Sci.*, 2010, Vol.34, no.8, pp.1475–1483.
53. Lefebvre, A. H. Airblast atomization. *Progress in Energy and Combustion Science*, vol.6, no.3, 1980, pp. 233-261.
54. Lefebvre, A. H. and Dilip, R. B. *Gas turbine combustion: Alternative Fuels and Emissions*. 3-rd Ed. CRC Press, 2010.
55. Less, D. M., & Schetz, J. A. Transient behavior of liquid jets injected normal to a high-velocity gas stream. *AIAA journal*, 1986, Vol.24, no.12, pp.1979-1986.
56. Lightfoot, M. D. A., Douglas G. Atomization rate of gas-centered swirl-coaxial injectors. *21st Annual Conference on Liquid Atomization and Spray Systems, Orlando, FL*. 2008.
57. Lyulka, L. A., Bazarov, V. G. Investigation of the self-oscillating regime of a liquid film in a coaxial air flow. *Izvestiya Vuzov. Aviation technology*, 1978, no.3, pp.19-24.
58. Michelson, I. Theory of vortex whistle. *The Journal of the Acoustical Society of America*, 1955, Vol.*27*, no.5, pp.930-931.
59. Mugele, R. and Evans, H. D. Droplet Size Distributions in Sprays. *Ind. Eng. Chem.*, Vol. 43, no.6, 1951, pp.1317–1324.
60. NFPA 750, N. F. P. A. Standard on Water Mist Fire Protection Systems. National Fire Protection Association, Quincy, MA, USA, 2010.
61. O'Brien, T. F., Bommaraju, T. V., & Hine, F. *Handbook of Chlor-Alkali Technology: Volume I: Fundamentals, Volume II: Brine Treatment and Cell Operation, Volume III: Facility Design and Product Handling, Volume IV: Operations, Volume V: Corrosion, Environmental Issues, and Future*

Developments. Springer Science & Business Media, 2007.

62. Orlov, V. A. *Stationary and dynamic characteristics of mixing process of gas-liquid injectors of liquid rocket engine* (in Russian), Ph. D. thesis, Khimmash, Sergeev pasad, Russia, 2001.
63. Otsu, N., A Threshold selection method from gray-level histograms. *IEEE Trans. Syst. Man Cybern.*, 1979, Vol. 9, no. 1, pp. 62–66.
64. Pages, D. G. and Galustov, V. *Fundamentals of the Technique of Spraying Liquids* (in Russian), Khimiya, 1984.
65. Park, G., Lee, J., Oh, S., Yoon, Y., & Sohn, C. H. Characteristics of gas-centered swirl coaxial injector with acoustic excitation of gas flow. *AIAA Journal*, 2016, Vol.55, no.3, pp.894-901.
66. Rizk, N. K., and Lefebvre, A. H, Prediction of velocity coefficient and spray cone angle for simplex swirl atomizer *Proc. 3rd Int. Conf. on Liquid Atomization and Spray Systems: ICLASS-85 (London, UK),* 1985, Vol.1, pp.111.
67. Santangelo, P. E. Characterization of high-pressure water-mist sprays: experimental analysis of droplet size and dispersion. *Exp. Therm.Fluid Sci.*, 2010, Vol.34, no.8, pp.1353–1366.
68. Saltanov, G. A. *Supersonic two-phase flows* (in Russian). Vysheish. Shkola, 1972.
69. Schetz, J. A., Injection and mixing in turbulent flow, *PrAA,* 1980, vol.68.
70. Schetz, J. A., Kush Jr, E. A., & Joshi, P. B. Wave phenomena in liquid jet breakup in a supersonic crossflow. *AIAA journal*, 1980, Vol.18, no.7, pp.774-778.
71. Schetz, J. & Sherman, A. Breakup of liquid sheets and jets in a supersonic gas stream. *AIAA Journal*, 1971, Vol.9, no.4, pp.666-673.
72. Schumaker, S., Danczyk, S., & Lightfoot, M. Effect of swirl on gas-centered swirl-coaxial injectors. *47th AIAA/ASME/SAE/ASEE Joint Propulsion Conference & Exhibit*, 2011, p.5621.
73. Segal, C. *The scramjet engine: processes and characteristics Vol.25*. Cambridge University Press, 2009.

74. Squire, H. B. Investigation of the instability of a moving liquid film, *British Journal of Applied Physics*, 1953, Vol.4, no.6, pp.167-169.

75. Stochek, N. D., and Shapiro A. S. *Hydraulics of liquid rocket engine* (in Russian). Mashinostroenie, Moscow, 1978.

76. Storch, M., Mishra, Y. N., Koegl, M., Kristensson, E., Will, S., Zigan, L., & Berrocal, E., Two-phase SLIPI for instantaneous LIF and Mie imaging of transient fuel sprays. *Optics letters*, 2016, Vol.41, no.23, pp.5422-5425.

77. Suzuki M., Theoretical and experimental studies on the vortex tube. *Scientific Papers Institute, Physics and Chemical Reseach*, Tokyo, 1960, pp.43-87.

78. Tashev, V. P. *Hydrocarbon fuel based on kerosene with additives to increase the energy efficiency of liquid rocket engines*. Ph. D thesis, MAI, Moscow, 2014.

79. Vasilev, A. P., Kudryavtsev, V. M., Kuznetsov, V. A., Kurpatenkov, V. D., Obel'nitsky, A. M., Polyaev, V. M., Poluyan, B. Ya., *Fundamentals of theory and calculation of liquid-propellant rocket engines* (in Russian), 2nd ed., Vysshaya Shkola, Moscow, 1975.

80. Vasiliev, A. P., Kudryavtsev, V. M., Kuznetsov, V. A., Kurpatenkov, V. D., Obelnitsky, A. M., Polyaev, V. M., & Poluyan, B. Ya. *Fundamentals of theory and calculation of liquid-propellant rocket engines* (in Russian). Vysshaya Shkola, 1983.

81. Vasiliev, A. P., Kudryavtsev, V. M., Kuznetsov, V. A., Kurpatenkov, V. D., Obelnitsky, A. M., Polyaev, V. M., & Poluyan, B. Ya. *Fundamentals of theory and calculation of liquid propellant rocket engines* (in Russian). Vysheshaya Shkola, Moscow, Russia, 1993.

82. Vonnegut, B. A vortex whistle. *The Journal of the Acoustical Society of America*, 1954, Vol.26, no.1, pp.18-20.

83. White, F. M. *Fluid Mechanics*. McGraw-Hill, 2008.

84. Yang, L. J., Ge, M. H., Zhang, M. Z., Fu, Q. F., & Cai, G. B. Spray characteristics of recessed gas-liquid coaxial swirl injector. *J. Propul. Power*, 2008, Vol.24, no.6, pp.1332-1339.

85. Yang, V., Habiballah, M., Hulka, J., Popp, M. *Liquid rocket thrust chambers-aspects of modeling, analysis, and design*, Progress in Astronautics and Aeronautics, Volume 200. AIAA, 2004.

86. Zhu, P., Wang, X. S., Li, G. C., Liu, Y. P., Kong, X. X., Huang, Y. Q., & Yuan, J. W. Experimental study on interaction of water mist spray with high-velocity gas jet. *Fire Saf. J.*, 2017, Vol.93, pp.60–73.

APPENDIX I.

DESIGN OF LIQUID SWIRL INJECTOR

Several approaches are possible for injector design. For this study, the expected injection angle used as input datum for deriving the injector geometry. The initial input values regarded as follows: injector differential pressure Δp_{ϕ}, coefficient of nozzle opening C, injector inlet number i, fluid mass flow $\dot{m}$, fluid density ρ, and fluid viscosity coefficient μ at injector inlet.

The theoretical injection angle according to the initial approximation is as Eq. (I.1).

$$2\alpha_{th} = \frac{2\alpha}{\overline{\alpha_0}} \qquad (I.1)$$

According to Dityakin et al. (1977), $\overline{\alpha_0}$ has a value in the range of 1.0 to 0.7. Considering the viscosity of the working fluid, the geometric coefficient A, the flow coefficient μ_{ϕ}, and the coefficient of passage fullness at the exit of a profiled nozzle φ can be obtained.

The outlet cross-sectional area of the injector nozzle is as follows:

$$F_{c1} = \pi r_c^2 = \frac{\dot{m}_1}{\mu_{\phi 1}\sqrt{2\Delta p_{\phi 1}\rho_1}} \qquad (I.2)$$

If the tangential inlet of the injector has rectangular cross section, the area can be obtained by using Eq. (3). Since the inlet shape ratio B is not known, an approximate value of the inlet flow strain coefficient ε_{in} was introduced ($\varepsilon_{in0} = 0.8$) [Dityakin et al. (1977)].

$$f_{in} = \frac{R_{in} r_c \pi}{\varepsilon_{in0} i A} \qquad (I.3)$$

From Eq. (I.3), the equivalent radius r_{in} of the nozzle is derived.

$$r_{in} = \frac{d_{in}}{2} = \sqrt{\frac{R_{in} r_c}{\varepsilon_{in0} i A}} \tag{I.4}$$

Reynolds number Re_{in} in the swirl chamber inlet is calculated as Eq. (I.5).

$$Re_{in} = \frac{4\,\dot{m}}{\mu\,\pi\,d_{in}\sqrt{i}} \tag{I.5}$$

The friction coefficient λ_{sc} in the swirl chamber depends on the range of Re_{in} [Dityakin et al. (1977)].

$$\lambda_{sc} = \frac{24.6}{{Re_{in}}^{0.75}}\ ;\ (Re_{in} \leq 2.3 \times 10^3) \tag{I.6}$$

$$\lambda_{sc} = \frac{1.22}{{Re_{in}}^{0.36}}\ ;\ (Re_{in} > 2.3 \times 10^3) \tag{I.7}$$

Considering the loss due to the flow at the inlet of the swirl chamber, the coefficient of friction λ_{in} at the inlet is calculated as Eq. (I.8).

$$\lambda_{in} = \frac{0.3164}{(Re_{in})^{0.25}} \tag{I.8}$$

When fluid flows from the tangential inlet to the swirl chamber, the loss must be considered. The inlet loss factor of the tangential path is dependent on the angle α_T between the inlet tangential flow path and the swirl chamber wall.

According to Kurpatenkov & Kurpatenkov (1987), Eq. (I.9) can be expressed as:

$$\alpha_T = 90 - arctan\left(\frac{R_k}{l_{in}}\right) \tag{I.9}$$

, Where R_k is the radius of the swirl chamber, and l_{in} is the length of the tangential flow path. The loss factor at the inlet of the tangential flow path is expressed by Eq.

(I.10) [Kurpatenkov & Kurpatenkov (1987)].

$$\xi_{in.inlet} = -\frac{1}{150}(\alpha_{\text{т}} - 30) + 0.9 \qquad (I.10)$$

The loss factor in the tangential flow path is as shown in Eq. (11) [Dityakin et al. (1977)].

$$\xi_{in.l} = \lambda_{in}\frac{l_{in}}{2r_{in}} \qquad (I.11)$$

The resistance coefficient of the hydrodynamic tangential flow path is shown by the empirical Eq. (I.12) [Dityakin et al. (1977)].

$$\xi_{in.h} = \frac{27.88}{(log\,Re_{in})^{3.572}} + 0.5746 \qquad (I.12)$$

Then, the hydrodynamic resistance coefficient generated in the tangential flow path is equal to the sum of the aforementioned loss coefficients.

$$\xi_{\mathrm{BX}} = \xi_{\mathrm{BX}.in} + \xi_{\mathrm{BX}h} + \xi_{in.l} \qquad (I.13)$$

According to Dityakin et al. (1977), the equivalent geometric coefficient $A_{\text{э}}$ considering the friction in the swirl chamber can be obtained with the complex characteristic coefficient θ_{sc} (Eq. I.14) on the effect of liquid friction around the inner wall of the swirl chamber about the liquid momentum moment:

$$\theta_{sc} = \frac{\lambda_{sc}}{2}A(C_{sc} - 1) \qquad (I.14)$$

$$A_{\text{э}} = \frac{A}{1 + \theta_{sc}} \qquad (I.15)$$

where, $C_{sc} = R_k/r_{\text{c}}$ is the ratio of the inner diameter of the swirl chamber to the inner diameter of the injector nozzle. The hydrodynamic inlet loss factor is shown in Eq. (I.16) [Dityakin et al. (1977)].

$$\mathit{\Delta}_{in} = \xi_{in} \frac{{A_{э}}^{2}}{C^{2}} \qquad (I.16)$$

Next, the loss due to the flow in the swirl chamber must be considered. If the equation is summarized using the parameter $\sigma = 1/A_{э} + (\lambda_{sc}\mathrm{C}_{sc})/2$, the energy loss coefficient due to the flow friction in the swirl chamber is as shown in Eq. (I.17) [Dityakin et al. (1977)].

$$\Delta_{sc} = \frac{\lambda_{sc}}{\sigma^{2}}\left\{\frac{1}{\sigma}\left(1 - \frac{1}{C_{sc}}\right) + \lambda_{sc}\left[\left(\frac{A_{э}}{2} - \frac{1}{2\sigma - \lambda_{sc}}\right)\left(\frac{2}{\sigma} + \frac{A_{э}}{2} + \frac{1}{2\sigma - \lambda_{sc}}\right) + \right.\right.$$

$$\left.\left. + \frac{3}{2\sigma^{2}} \ln \frac{(2\sigma - \lambda_{к})A_{э}C_{sc}}{2}\right]\right\} \qquad (I.17)$$

Considering the liquid friction coefficient $\lambda_{s} = \bar{\lambda} \cdot \lambda_{sc}$ at the side wall of the swirl chamber, the loss according to the swirl chamber length $l_{sc} = \overline{l_{sc}} \cdot D_{sc}$ can be obtained (D_{sc}: inside diameter of the swirl chamber). Since the swirl chamber has the same shape as the fully open injector, the geometric coefficient $A_{open.э}$, the filling coefficient $\varphi_{open.э}$, and the flow coefficient $\mu_{open.э}$ can be corrected as follows [Dityakin et al. (1977), Egorychev (2011)].

$$A_{open.э} = A \cdot C_{sc} \qquad (I.18)$$

$$\varphi_{open.э} = \frac{1}{\left(\sqrt[3]{\frac{A_{open.э}}{2\sqrt{2}} + \sqrt{\frac{{A_{open.э}}^{2}}{8} - \frac{1}{27}}} + \sqrt[3]{\frac{A_{open.э}}{2\sqrt{2}} - \sqrt{\frac{{A_{open.э}}^{2}}{8} - \frac{1}{27}}}\right)^{2}} \qquad (I.19)$$

$$\mu_{ф.open.э} = \frac{\varphi_{open.э}\sqrt{\varphi_{open.э}}}{\sqrt{2 - \varphi_{open.э}}} \qquad (I.20)$$

The energy loss factor by the length of the injector can be calculated with these parameters [Dityakin et al. (1977)].

$$\Delta_L = \frac{A^2}{2\text{С}_\text{к}}\left(1 + \mu_{\text{ф}.open.\text{э}} \cdot A \cdot \text{С}_{sc}\right)\left(1 - \frac{1}{\left(1 + \theta_{sc} \cdot \bar{\lambda} \cdot \overline{l_{sc}} \frac{\text{С}_{sc}}{\text{С}_{sc} - 1}\right)^2}\right) \qquad (I.21)$$

According to Vasiliev (1983), the correction factor of the flow coefficient by the angle φ_c between the swirl chamber and the nozzle is as Eq. (I.22).

$$\overline{\mu_{noz}} = 1.638(180 - 2\varphi_c)^{-0.4893} + 0.7372 \qquad (I.22)$$

The corrected flow coefficient can be obtained by using $\overline{\mu_{noz}}$.

$$\mu_{\phi.noz} = \overline{\mu_{noz}} \frac{1}{\sqrt{\frac{1}{\varphi^2} + \frac{A^2}{1 - \varphi}}} \qquad (I.23)$$

The energy loss coefficient by the angle between the swirl chamber and the nozzle is as follows.

$$\Delta_{noz} = \frac{1}{{\mu_{\phi.noz}}^2} - \frac{1}{\varphi^2} - \frac{A^2}{1 - \varphi} \qquad (I.24)$$

The sum of the energy loss coefficients is shown in Eq. (I.25).

$$\Delta_\Sigma = \Delta_{\text{вх}} + \Delta_\text{к} + \Delta_L + \Delta_{noz} \qquad (I.25)$$

Generalized equivalent geometric coefficients, filling coefficients, and flow coefficients can be calculated similarly to Eqs. (I.14), (I.15), (I.19), and (I.23) [Egorychev (2011)].

$$A_{\text{э.э}} = \frac{A}{1 + \theta_{sc} \cdot \left(1 + \overline{\lambda l_{sc}} \frac{\text{С}_{sc}}{\text{С}_{sc} - 1}\right)} \qquad (I.26)$$

$$\varphi_{э.э} = \frac{1}{\left(\sqrt[3]{\frac{A_{э.э}}{2\sqrt{2}} + \sqrt{\frac{{A_{э.э}}^2}{8} - \frac{1}{27}}} + \sqrt[3]{\frac{A_{э.э}}{2\sqrt{2}} - \sqrt{\frac{{A_{э.э}}^2}{8} - \frac{1}{27}}}\right)^2} \tag{27}$$

$$\mu_{\phi.э} = \frac{1}{\sqrt{\frac{1}{{\varphi_{э.э}}^2} + \frac{{A_{э.э}}^2}{1-\varphi_{э.э}} + \Delta_\Sigma}} \tag{28}$$

According to Dityakin et al. (1977), the flow coefficient of the air-core at the outlet of the injector nozzle is presented by Eq. (I.29), where $\overline{r_{mв}}$ is the relative radius of the air-core at the outlet of the injector.

$$\mu_ф = \sqrt{1 - {\mu_ф}^2 A^2} - \overline{r_{mв}}\sqrt{\overline{r_{mв}}^2 - {\mu_ф}^2 A^2}$$

$$-{\mu_ф}^2 A^2 \ln \frac{1 + \sqrt{1 - {\mu_ф}^2 A^2}}{\overline{r_{mв}} + \sqrt{\overline{r_{mв}}^2 - {\mu_ф}^2 A^2}} \qquad (I.29)$$

The spray angle can be recalculated from the generalized equivalent geometric coefficient $2\alpha_\theta = f(A_{э.э})$.

The spray angle coefficient (ratio of the experimental value to the theoretical value) is shown in Eq. (I.30) [Dityakin et al. (1977)].

$$\bar{\alpha} = \frac{2\alpha_{experiment}}{2\alpha_{theory}} = 0.6292 \cdot {\theta_{sc}}^6 - 2.7656 \cdot {\theta_{sc}}^5 + 4.6262 \cdot {\theta_{sc}}^4$$

$$-3.8308 \cdot {\theta_{sc}}^3 + 1.8381 \cdot {\theta_{sc}}^2 - 0.7454 \cdot \theta_{sc} + 1.0004$$

$$= 0.7713 - 0.10849(\ln(\theta_{sc} + 0.14567)) \qquad (I.30)$$

This can be used to correct the spray angle.

$$2\alpha' = \bar{\alpha} \cdot 2\alpha_{\theta} \qquad (I.31)$$

It is possible to correct the geometric coefficient due to the flow compression of the tangential inlet. The inlet shape ratio B and the inlet flow strain factor ε_{in} can be calculated.

$$B = \frac{R_{in}}{r_{in}} \qquad (I.32)$$

$$\varepsilon_{in} = \frac{R_{in}}{R_{in.e}} = 19.187\frac{1}{B}^{6} - 54.325\frac{1}{B}^{5} + 62.345\frac{1}{B}^{4} - 37.482\frac{1}{B}^{3} + 12.838\frac{1}{B}^{2}$$

$$-2.5597\frac{1}{B} + 1.003 \qquad (\text{I}.33)$$

Each parameter is iteratively calculated by comparing it with the initial approximation.

The air-core radius in the injector nozzle can be calculated as the correlation between factors $\overline{r_m} = r_m/r_c = f(A, C)$ suggested by Kurpatenkov (1987).

$if\ C = 1,$

$$then\ \overline{r_m} = -0.4344 \cdot exp\left(\frac{-\text{A}_{\text{э.э}}}{3.2643}\right) - 0.3258 \cdot exp\left(\frac{-\text{A}_{\text{э.э}}}{0.6465}\right) + 0.82332$$

$if\ C = 2,$

$$then\ \overline{r_m} = -0.4175 \cdot exp\left(\frac{-\text{A}_{\text{э.э}}}{4.55}\right) - 0.3679 \cdot exp\left(\frac{-\text{A}_{\text{э.э}}}{0.7491}\right) + 0.8348$$

$if\ C = 3,$

$$then\ \overline{r_m} = -0.6660 \cdot exp\left(\frac{-\text{A}_{\text{э.э}}}{0.45154}\right) - 0.4355 \cdot exp\left(\frac{-\text{A}_{\text{э.э}}}{3.38244}\right) + 0.73792$$

$if\ C = 4,$

$$then\ \overline{r_m} = -0.7632 \cdot exp\left(\frac{-\text{А}_{\text{э.э}}}{0.47569}\right) - 0.4069 \cdot exp\left(\frac{-\text{А}_{\text{э.э}}}{4.36459}\right) + 0.66879$$

The correction factor of the flow coefficient is calculated as Eq. (34).

$$\overline{\mu_\phi} = \frac{\mu_{\phi.\text{э}}}{\mu_\phi} \qquad (I.34)$$

The differential pressure of the injector is corrected as in Eq. (I.35).

$$\Delta p_{\text{ф}.c} = \frac{\Delta p_{\text{ф}}}{\overline{\mu_\phi}^2} \qquad (I.35)$$

Radius of the nozzle is calculated:

$$r_c' = \sqrt{\frac{1}{\pi\sqrt{2}}}\sqrt{\frac{\dot{m}_{\text{ф}}}{\mu_{\text{ф.э}}\sqrt{\rho\Delta p_{\text{ф.c}}}}} \qquad (I.36)$$

Then, the radius of the air-core at the outlet of the injector is presented as Eq. (I.37)

$$r_m = r_c' \sqrt{1 - \varphi_{\text{э.э}}} \qquad (I.37)$$

The spray angle is recalculated as it can be dependent on the flow change in the nozzle. According to Kurpatenkov (1987), the value of the ratio of length to orifice diameter ($\overline{l_c} = l_c/d_c$) is usually in the range from 0.5 to 2.0. In order to escape the section where hydraulic jump occurs within the nozzle, the length of the initial section should be checked. The length of the initial section is as shown in Eq. (I.38).

$$l_{int} = 4h = 4r_c\left(1 - \sqrt{1 - \varphi_{\text{э.э}}}\right) \qquad (I.38)$$

According to Dityakin (1977), if the dimensionless number of the initial section length of the nozzle has a value greater than 4, it is possible to escape the section of the hydraulic jump.

$$\overline{l_{int}} = \frac{l_c}{h} > 4 \tag{I.39}$$

The relative flow coefficient can be calculated by the following relationship with dimensionless length of initial section.

$$\bar{\mu} = 1.0013 + \frac{1.0697 - 1.0013}{1 + exp\left(\frac{\overline{l_{int}} - 2.0294}{0.4264}\right)} \tag{I.40}$$

The velocity head at the injector inlet (I.41) and the liquid Reynolds number in the nozzle (I.42) can be calculated by hydraulic theory.

$$p_{\text{Т}} = \frac{1}{2\rho}\left(\frac{\dot{m}_{\text{ф}}}{\pi {r_c}^2}\right)^2 \tag{I.41}$$

$$Re_H = \frac{\rho}{\mu} d_c \sqrt{\frac{2p_{\text{Т}}}{\rho}} \tag{I.42}$$

Dityakin (1977) mentioned the momentum loss factor (I.44) depending on the friction factor (I.43) in the injector nozzle.

$$\lambda_{noz} = 0.03019 \cdot \left(\frac{Re_H}{10^4}\right)^{0.92638} \tag{I.43}$$

$$K_{noz} = 1 + \frac{1}{2}\lambda_{noz}\overline{l}_c A_{\text{э.э}}\sqrt{1 - \Delta_{\Sigma}{\mu_{\phi.\text{э}}}^2} \tag{I.44}$$

Using this, Egorychev (2011) proposed the average spray angle of the injector 2αm as shown in equation (I.45).

$$2\alpha_m = 2\bar{\alpha} \cdot \tan^{-1}\frac{2\mu_{\text{ф}.\theta}A_{\text{э.э}}}{\sqrt{{K_{noz}}^2(1 + \bar{r}_{m\text{в}})^2 - 4{\mu_{\text{ф}.\theta}}^2{A_{\text{э.э}}}^2}} \tag{I.45}$$

If the central injector is located, the spray angle can be reduced by interference and invasion by the solid wall. According to Arsentiev (1972), according to the vortex zone invasion coefficient $\bar{r} = r_{c2}/r_{c1\text{H}}$ and the geometric coefficient A, the average spray angle can be obtained by the following relationship.

$$if\ A = 0.5, then\ 2\alpha_m = -473.10562exp\left(\frac{-\bar{r}}{0.46825}\right) + 56.09884$$

$$if\ A = 0.6, then\ 2\alpha_m = -468.784exp\left(\frac{-\bar{r}}{0.48762}\right) + 64.03644$$

$$if\ A = 0.8, then\ 2\alpha_m = -778.5372exp\left(\frac{-\bar{r}}{0.43765}\right) + 79.45151$$

$$if\ A = 1.0, then\ 2\alpha_m = -1093.87521exp\left(\frac{-\bar{r}}{0.40048}\right) + 91.31983$$

$$if\ A = 1.2, then\ 2\alpha_m = -1257.945exp\left(\frac{-\bar{r}}{0.39887}\right) + 105.3338$$

$$if\ A = 1.4, then\ 2\alpha_m = -1451.74exp\left(\frac{-\bar{r}}{0.38554}\right) + 114.1906$$

$$if\ A = 1.6, then\ 2\alpha_m = -2227.20exp\left(\frac{-\bar{r}}{0.31995}\right) + 107.3245$$

$$if\ A = 1.8, then\ 2\alpha_m = -903.74exp\left(\frac{-\bar{r}}{0.5477}\right) + 158.98$$

$$if\ A = 2, then\ 2\alpha_m = -6019.338exp\left(\frac{-\bar{r}}{0.24732}\right) + 112.90053$$

$$if\ A = 3, then\ 2\alpha_m = -2375.234exp\left(\frac{-\bar{r}}{0.36186}\right) + 170.91138$$

$$if\ A = 4, then\ 2\alpha_m = -1126.565exp\left(\frac{-\bar{r}}{0.89236}\right) + 399.25859$$

$$if\ r_m = r_{c.out.center}, 2\alpha = 1569.021exp\left(\frac{-\bar{r}}{0.38481}\right) + 23.10561$$

At this time, the flow coefficient was also proposed.

$$if\ A = 20, then\ \mu_{\Phi} = -367930.6202exp\left(\frac{-\bar{r}}{0.06093}\right) + 0.05316$$

$$if\ A = 10, then\ \mu_{\Phi} = -46265.741exp\left(\frac{-\bar{r}}{0.0747}\right) + 0.10645$$

$$if\ A = 6, then\ \mu_{\Phi} = -25.0956exp\left(\frac{-\bar{r}}{0.03609}\right) + 0.13437$$

$$if\ A = 4, then\ \mu_{\Phi} = -608477.904896exp\left(\frac{-\bar{r}}{0.06744}\right) + 0.19268$$

$$if\ A = 3, then\ \mu_{\Phi} = -422.349exp\left(\frac{-\bar{r}}{0.13298}\right) + 0.26629$$

$$if\ A = 2.5, then\ \mu_{\Phi} = -190.675exp\left(\frac{-\bar{r}}{0.15314}\right) + 0.3096$$

$$if\ A = 2, then\ \mu_{\Phi} = -99.1526exp\left(\frac{-\bar{r}}{0.17513}\right) + 0.35763$$

$$if\ A = 1.5, then\ \mu_{\Phi} = -92.82exp\left(\frac{-\bar{r}}{0.1839}\right) + 0.4047$$

$$if\ A = 1.2, then\ \mu_{\Phi} = -21.273exp\left(\frac{-\bar{r}}{0.2609}\right) + 0.5008$$

$$if\ A = 1.0, then\ \mu_{\Phi} = -33.536exp\left(\frac{-\bar{r}}{0.2421}\right) + 0.5286$$

$$if\ A = 0.8, then\ \mu_{\Phi} = -12.710exp\left(\frac{-\bar{r}}{0.3161}\right) + 0.5985$$

$$if\ A = 0.6, then\ \mu_{\Phi} = -11.060exp\left(\frac{-\bar{r}}{0.35567}\right) + 0.67611$$

$$if\ A = 0.5, then\ \mu_{\Phi} = -5.10523exp\left(\frac{-\bar{r}}{0.49784}\right) + 0.77738$$

$$if\ r_m = r_{c.out.center}, \mu_{\Phi} = -3.2880exp\left(\frac{-\bar{r}}{1.5314}\right) + 1.7093$$

APPENDIX II.

DESIGN OF GAS SWIRL INJECTOR

According to the Russian Federation standard GOST 21980-76, it is possible to calculate for gas swirl injectors in the following order:

Initial value for design are thermodynamic parameters of gas component – molecular weight μ_M, adiabatic index k, inlet temperature T_{in}, inlet density ρ, mass flow rate $\dot{m}_\phi$, viscosity coefficient μ, and factors for determining the injector shape – geometric coefficient A, The relative radius of the swirl arm $\bar{R}_{in}$.

The expansion ratio of the nozzle is determined by the injector differential pressure Δp_ϕ and the combustion chamber pressure p_{ch}.

$$\pi_\Phi = \frac{p_{\text{вх}}}{p_{\text{вых}}} = 1 + \frac{\Delta p_\Phi}{p_{ch}} \qquad (II.1)$$

The relative length to the diameter of the tangential inlet path ($\overline{l_{in}} = l_{in}/d_{in}$) and the relative length of the swirl chamber to the swirl chamber diameter ($\overline{l_{sw}} = l_{sw}/d_{sw}$) have values of 1.0 to 1.5 and 0.1 to 0.3, respectively.

If the relative radius of the swirl arm has a value of 0.2~1.0, the reference value of the flow coefficient $\mu_{\Phi.ref}$ can be calculated as follows according to the geometric coefficient A.

$$if\ A \geq 3.0, then\ \mu_{\Phi.ref} = -0.283exp\left(\frac{-\pi_\Phi}{2.3338}\right) + 0.3219$$

$$if\ A = 2.0, then\ \mu_{\Phi.ref} = -0.267exp\left(\frac{-\pi_\Phi}{1.177}\right) + 0.287$$

$$if\ A = 1.4, then\ \mu_{\Phi.ref} = -1922.0418exp\left(\frac{-\pi_\Phi}{12772.960}\right) + 1922.1068$$

$$if\ A = 1.0, then\ \mu_{\Phi.ref} = -5.4697exp\left(\frac{-\pi_{\Phi}}{30.7952}\right) + 5.58856$$

$$if\ A = 0.8, then\ \mu_{\Phi.ref} = -0.718exp\left(\frac{-\pi_{\Phi}}{1.3426}\right) + 0.7011$$

$$if\ A = 0.6, then\ \mu_{\Phi.ref} = -2.0144exp\left(\frac{-\pi_{\Phi}}{7.1653}\right) + 2.2512$$

$$if\ A = 0.4, then\ \mu_{\Phi.ref} = -7.62876exp\left(\frac{-\pi_{\Phi}}{39.28467}\right) + 8.02409$$

In addition, the coefficient of proportionality $\overline{\mu_{\Phi}}$ for the reference value is calculated by the following empirical formula according to the value of the relative radius $\overline{R}_{in}$ of the swirl arm.

$$if\ \overline{R_{\text{вх}}} = 0.5, then\ \overline{\mu_{\Phi}} = 0.148exp\left(\frac{-A}{1.061}\right) + 0.847$$

$$if\ \overline{R_{\text{вх}}} = 0.6, then\ \overline{\mu_{\Phi}} = 0.101exp\left(\frac{-A}{1.260}\right) + 0.899$$

$$if\ \overline{R_{\text{вх}}} = 0.7, then\ \overline{\mu_{\Phi}} = 0.037exp\left(\frac{-A}{1.337}\right) + 0.961$$

$$if\ \overline{R_{\text{вх}}} = 0.8, then\ \overline{\mu_{\Phi}} = 1.02186 - \frac{0.0214}{1 + \left(\frac{A}{0.75288}\right)^{1.88003}}$$

$$if\ \overline{R_{\text{вх}}} = 0.9, then\ \overline{\mu_{\Phi}} = -0.0932exp\left(\frac{-A}{1.68548}\right) + 1.09423$$

$$if\ \overline{R_{\text{вх}}} = 1.0,$$

$$then\ \overline{\mu_{\Phi}} = -0.41171exp\left(\frac{-A}{8.07701}\right) - 0.02694exp\left(\frac{-A}{0.44687}\right) + 1.43736$$

Then, the flow coefficient is calculated by Eq. (II.2).

$$\mu_{\text{ф}.1} = \overline{\mu_{\text{ф}}}\mu_{\text{ф}.ref} \qquad (II.2)$$

If $4 \geq \overline{l_{sw}} > 0.3$, the Eq. (II.3 ~ II.6) can be used for calculation.

$$\mu_{\text{ф}.ref\ 1.05} = 0.9126 \cdot \exp\left(-\frac{A}{0.6128}\right) + 0.1352 \qquad (II.3)$$

$$\mu_{\text{ф}.2} = \mu_{\text{ф}.ref\ 1.05}\overline{\mu_{\text{ф}}} \qquad (II.4)$$

$$b = 0.0225A(\overline{R_{\text{вх}}} - 0.3)\left(\overline{l_{sw}} - 0.3\right) \qquad (II.5)$$

$$\mu_{\text{ф}} = \mu_{\text{ф}.1} + b \cdot \mu_{\text{ф}.2} \qquad (II.6)$$

The aerodynamic coefficient is calculated by Eq. (II.7).

$$\varphi_{\text{ф}} = \pi_{\text{ф}}\sqrt{\frac{k}{k-1}\left(\frac{1}{\pi_{\text{ф}}^{\frac{2}{k}}} - \frac{1}{\pi_{\text{ф}}^{\frac{k+1}{k}}}\right)} \qquad (II.7)$$

The nozzle diameter is calculated by Eq. (II.8).

$$d_c = \sqrt{\frac{4}{\pi\sqrt{2}}}\sqrt{\frac{\dot{m}_{\text{ф}}\sqrt{RT_{in}}}{\mu_{\text{ф}}p_{ch}\varphi_{\text{ф}}}} \qquad (II.8)$$

The radius of the swirl arm is got by Eq. (II.9).

$$R_{in} = \overline{R_{in}}\frac{d_c}{2} \qquad (II.9)$$

The Reynolds number of the tangential path is calculated by Eq. (II.10).

$$\mathrm{Re}_{in} = \frac{1}{\mu\sqrt{d_c}}d_c^2\frac{\mu_{\text{ф}}p_{ch}\varphi_{\text{ф}}}{\sqrt{RT_{in}}}\sqrt{\frac{A}{R_{in}}} \qquad (II.10)$$

According to White (2008), Nikuradse Eq. (II.11) and Blasius Eq. (II.12) can be used as the coefficient of resistance depends on the range of the Reynolds number of the tangential flow channel.

$$if\ 4000 < \mathrm{Re}_{in}, 10000 > \mathrm{Re}_{in}, \mathrm{then}\ \lambda = \frac{0.3164}{\mathrm{Re}_{in}^{0.25}} \qquad (II.11)$$

$$if\ \mathrm{Re}_{in} \geq 10000, \mathrm{then}\ \lambda = 0.0032 + \frac{0.221}{\mathrm{Re}_{in}^{0.237}} \qquad (II.12)$$

The gas vortex coefficient at the outlet of the injector nozzle can be obtained using the method of Dityakin (1977) as follows.

$$\mu_{\text{ф}} = \sqrt{1 - {\mu_{\text{ф}}}^2 A^2} - \overline{r_{m\text{в}}}\sqrt{\overline{r_{m\text{в}}}^2 - {\mu_{\text{ф}}}^2 A^2}$$

$$-{\mu_{\text{ф}}}^2 A^2 \ln \frac{1 + \sqrt{1 - {\mu_{\text{ф}}}^2 A^2}}{\overline{r_{m\text{в}}} + \sqrt{\overline{r_{m\text{в}}}^2 - {\mu_{\text{ф}}}^2 A^2}} \qquad (II.13)$$

The number of inlet channels *i* is selected based on the condition of the gas distribution inconsistency coefficient *K*.

In the case of a rectangular cross section, the cross-sectional area of the tangential flow path of the injector is obtained by using the width a_{in} and the height b_{in} of the flow path as Eq. (II.14).

$$f_{in} = a_{in} b_{in} = \frac{R_{in} \cdot r_c \cdot \pi}{i \cdot A} \qquad (II.14)$$

Therefore, the equivalent diameter of the tangential flow path is given by Eq. (II.15).

$$d_{in} = 2\sqrt{\frac{R_{in} r_c}{i \cdot A}} \qquad (II.15)$$

The relative diameter $\overline{d_{in}} = d_{in}/d_c$ of the tangential flow path depends on the number of inlet flow paths for fully open injectors:

$$if\ i=2, then\ \overline{d_{in}} \ = 0.1654 \exp\left(-\frac{A}{4.05563}\right) + 0.20859 \exp\left(-\frac{A}{1.42126}\right) + 0.17923 \exp\left(-\frac{A}{25.28635}\right) + 0.06701$$

$$if\ i=4, then\ \overline{d_{in}} = 0.17243 \exp\left(-\frac{A}{4.84971}\right) + 17.54514 exp\left(-\frac{A}{8097.01605}\right) + 0.24875 \exp\left(-\frac{A}{1.0919}\right) - 17.39635$$

$$if\ i=6, then\ \overline{d_{in}} = 0.25594 \exp\left(-\frac{A}{0.76438}\right) + 0.16467 \exp\left(-\frac{A}{3.24383}\right) + 1.2889 \exp\left(-\frac{A}{344.47663}\right) - 1.13856$$

$$if\ i=8, then\ \overline{d_{in}} = 0.17261 \exp\left(-\frac{A}{1.39213}\right) + 0.1456 \exp\left(-\frac{A}{8.11064}\right) + 0.20862 \exp\left(-\frac{A}{0.42063}\right) + 0.06527$$

$$if\ i=10, then\ \overline{d_{in}} = 0.18556 \exp\left(-\frac{A}{0.9352}\right) + 0.15572 \exp\left(-\frac{A}{5.39209}\right) + 0.22606 \exp\left(-\frac{A}{0.26955}\right) + 0.07161$$

$$if\ i=12, then\ \overline{d_{in}} = 0.18276 \exp\left(-\frac{A}{1.3934}\right) + 670.31802 \exp\left(-\frac{A}{86950.65393}\right) + 0.23984 \exp\left(-\frac{A}{0.31985}\right) - 670.16108$$

$$
\begin{aligned}
&if\ i = 14, then\ \overline{d_{in}} \\
&\qquad = 0.15926 \exp\left(-\frac{A}{1.35401}\right) + 0.22159 \exp\left(-\frac{A}{0.34686}\right) \\
&\qquad + 0.13437 \exp\left(-\frac{A}{12.50122}\right) + 0.02107
\end{aligned}
$$

$$
\begin{aligned}
&if\ i = 16, then\ \overline{d_{in}} \\
&\qquad = 3.47171 \exp\left(-\frac{A}{474.06517}\right) + 0.15425 \exp\left(-\frac{A}{1.39057}\right) \\
&\qquad + 0.19077 \exp\left(-\frac{A}{0.38903}\right) - 3.33356
\end{aligned}
$$

$$
\begin{aligned}
&if\ i = 18, then\ \overline{d_{in}} \\
&\qquad = 0.14338 \exp\left(-\frac{A}{0.80635}\right) + 0.15065 \exp\left(-\frac{A}{5.29639}\right) \\
&\qquad + 0.29199 \exp\left(-\frac{A}{0.21833}\right) + 0.03937
\end{aligned}
$$

$$
\begin{aligned}
&if\ i = 24, then\ \overline{d_{in}} \\
&\qquad = 0.51208 \exp\left(-\frac{A}{0.14139}\right) + 0.15696 \exp\left(-\frac{A}{0.65801}\right) \\
&\qquad + 0.16114 \exp\left(-\frac{A}{5.92617}\right) + 0.01294
\end{aligned}
$$

$$
\begin{aligned}
&if\ i = 30, then\ \overline{d_{in}} \\
&\qquad = 0.13994 \exp\left(-\frac{A}{0.82631}\right) + 0.26471 \exp\left(-\frac{A}{0.20308}\right) \\
&\qquad + 12.82844 \exp\left(-\frac{A}{956.36209}\right) - 12.69258
\end{aligned}
$$

The tangential inlet length, the radius and length of the swirl chamber are calculated as follows:

$$l_{in} = \overline{l_{in}} d_{in} \qquad (II.16)$$

$$d_{sw} = 2R_{in} + d_{in} \qquad (II.17)$$

$$l_{sw} = \overline{l_{sw}} d_{sw} \qquad (II.18)$$

The outer radius can be obtained by using these parameters as Eq. (II.19).

$$r_{out} = \sqrt{\left[l_{in} + \sqrt{d_{in}(2R_{sw} - d_{in})}\right]^2 + R_{sw}^2} \qquad (II.19)$$

The formula for filling factor was proposed by Egorychev (2011) as equation (II.20).

$$\varphi = \frac{1}{\left(\sqrt[3]{\frac{A}{2\sqrt{2}} + \sqrt{\frac{A^2}{8} - \frac{1}{27}}} + \sqrt[3]{\frac{A}{2\sqrt{2}} - \sqrt{\frac{A^2}{8} - \frac{1}{27}}}\right)^2} \qquad (II.20)$$

The radius of the air-core is presented as follow.

$$r_m = r_c\sqrt{1 - \varphi} \qquad (II.21)$$

The average spray angle *2α_m* depends on the geometric coefficient *A* and the coefficient of nozzle opening *C*.

$$\begin{aligned} &if\ C = 0.5, then\ 2\alpha_m \\ &\quad = -39.87324exp\left(\frac{-A}{0.39584}\right) - 92.49318exp\left(\frac{-A}{3.74906}\right) \\ &\quad + 147.85861 \end{aligned}$$

$$\begin{aligned} &if\ C = 0.6, then\ 2\alpha_m \\ &\quad = -39.62761exp\left(\frac{-A}{0.21028}\right) - 80.53321exp\left(\frac{-A}{2.55828}\right) \\ &\quad + 124.13007 \end{aligned}$$

$$\begin{aligned} &if\ C = 0.75, then\ 2\alpha_m \\ &\quad = -30.02135exp\left(\frac{-A}{0.29797}\right) - 71.28299exp\left(\frac{-A}{2.39061}\right) \\ &\quad + 112.96373 \end{aligned}$$

$$if\ C = 1, then\ 2\alpha_m$$

$$= -20.6389exp\left(\frac{-A}{0.3549}\right) - 67.5805exp\left(\frac{-A}{2.35423}\right)$$

$$+ 106.6136$$

$$if\ C = 1.5, then\ 2\alpha_m$$

$$= -58.93728exp\left(\frac{-A}{2.43378}\right) - 16.18417exp\left(\frac{-A}{0.40011}\right)$$

$$+ 99.40281$$

$$if\ C = 2, then\ 2\alpha_m$$

$$= -54.79441exp\left(\frac{-A}{2.26334}\right) - 16.67078exp\left(\frac{-A}{2.26334}\right)$$

$$+ 92.29184$$

$$if\ C = 3, then\ 2\alpha_m$$

$$= -21.4618exp\left(\frac{-A}{0.55112}\right) - 46.5080exp\left(\frac{-A}{2.07528}\right)$$

$$+ 85.11186$$

$$if\ C = 4, then\ 2\alpha_{\mathrm{cp}}$$

$$= -53.81049exp\left(\frac{-A}{1.73839}\right) - 17.54235exp\left(\frac{-A}{0.31832}\right)$$

$$+ 80.44731$$

The outer spray angle $2\alpha_{out}$ of the oscillating discharged gas flow is also dependent on the A and C.

$$if\ C = 0.5, then\ \ 2\alpha_{out}$$

$$= \ -33.31475\,exp\left(-\frac{A}{0.01154}\right) - 33.87623\,exp\left(-\frac{A}{0.35764}\right)$$

$$- 138.2173\,exp\left(-\frac{A}{4.83965}\right) + 199.98901$$

$$if\ C = 0.6, then\ 2\alpha_{out} = -32.85201\, exp\left(-\frac{A}{0.20204}\right)$$

$$-111.57009ex\left(-\frac{A}{3.20221}\right) - 8.42738\, exp\left(-\frac{A}{0.00317}\right)$$

$$+160.02032$$

$$if\ C = 0.75, then\ 2\alpha_{out} = -98.07773\, exp\left(-\frac{A}{3.28982}\right)$$

$$-30.01657\, exp\left(-\frac{A}{0.33815}\right) - 27.13527\, exp\left(-\frac{A}{0.00523}\right)$$

$$+146.68738$$

$$if\ C = 1, then\ 2\alpha_{out} = -21.97519 \exp\left(-\frac{A}{0.29237}\right)$$

$$-11.27223 \exp\left(-\frac{A}{0.00683}\right) - 89.19414 \exp\left(-\frac{A}{2.81729}\right)$$

$$+131.11615$$

$$if\ C = 1.5, then\ 2\alpha_{out} = -77.24646 \exp\left(-\frac{A}{2.71402}\right)$$

$$-28.5524 \exp\left(-\frac{A}{0.37809}\right) - 13.21977 \exp\left(-\frac{A}{0.01459}\right)$$

$$+118.94311$$

$$if\ C = 2, then\ 2\alpha_{out} = -27.69215 \exp\left(-\frac{A}{0.41882}\right)$$

$$-64.25631 \exp\left(-\frac{A}{2.57066}\right) - 16.79194 \exp\left(-\frac{A}{0.03006}\right)$$

$$+107.50611$$

$$if\ C = 3, then\ 2\alpha_{out} = -23.4274 \exp\left(-\frac{A}{0.3143}\right)$$

$$-62.76928 \exp\left(-\frac{A}{2.3493}\right) - 17.327 \exp\left(-\frac{A}{0.02195}\right)$$

$$+100.28543$$

$$if\ C = 4, then\ 2\alpha_{out} = -57.87547 \exp\left(-\frac{A}{2.1675}\right) - 25.11934 \exp\left(-\frac{A}{0.37589}\right) - 10.15308 \exp\left(-\frac{A}{0.01833}\right) + 93.07238$$

APPENDIX III.

ACOUSTIC FREQUENCY OF GAS SWIRL INJECTOR

Michelson (1955) derived the acoustic frequency using the following method to understand the noise generated by the vortex whistle (swirl gas injector).

The thermodynamic definition of the speed of sound is expressed as Eq. (III.1):

$$a = \sqrt{k\frac{p}{\rho}} = \sqrt{\gamma RT} \qquad (III.1)$$

where, γ – insulation index, R – gas constant.

The dynamic pressure q of the gas considering the definition of the Mach number M can be expressed as Eq. (III.2):

$$q = \frac{1}{2}\rho \mathrm{v}^2 = \frac{1}{2}\gamma p \mathrm{M}^2 \qquad (III.2)$$

Where, v – velocity of the gas, ρ – density of the gas.

The dynamic pressure is expressed aerodynamically as Eq. (III.3), since it is generated from the pressure difference of the injector. The injector inlet is marked with subscript *1* and the injector outlet is marked with subscript *2*.

$$p_1 - p_2 = \frac{\gamma}{2}p_1\left(\frac{v}{a}\right)^2$$

$$v = a\sqrt{\frac{2}{\gamma}\frac{p_1 - p_2}{p_1}} \qquad (III.3)$$

The frequency is expressed as an angular frequency, $f = \omega/2\pi$ ($\omega = kv$), since the gas flow has rotational motion. Here, k is the angular wavenumber ($k = 2\pi/\lambda$). It can be said that the wavelength of the gas wave rotating inside the cylinder is the same as the circumference of the cylinder ($\lambda \sim \pi D$). Then the frequency can be presented as Eq. (III.4).

$$\omega = kv = ka\sqrt{\frac{2}{\gamma}}\sqrt{\frac{p_1 - p_2}{p_1}}$$

$$f = \frac{\omega}{2\pi} = \frac{a}{\pi \mathrm{D}}\sqrt{\frac{2}{\gamma}}\sqrt{\frac{\Delta \mathrm{p}}{p_1}} = \frac{a}{\pi \mathrm{D}}\nu_t\sqrt{\frac{\Delta \mathrm{p}}{p_1}} \qquad \text{(III.4)}$$

Here, it can be considered that ν_t is related to the thermal insulation index, but it is actually regarded as another parameter.

초 록

높은 효율을 가지는 다단연소 사이클과 같은 액체로켓엔진 시스템에서는 연소실로 기체-액체의 형태로 추진제가 유입된다. 일반적인 축대칭 연소기의 경우, 원통부 뒤에 유체를 가속시키기 위한 노즐이 연결되므로 연소반응이 완료되지 않은 추진제가 배출될 수 있다. 그러므로 동일 축방향 변위에서 이동거리 및 체류시간을 늘릴 수 있는 와류형 분사기를 사용할 필요가 있다.

기체 중심 동축 와류형 기체-액체 분사기의 경우, 혼합실(recessed region)을 적용한다면 기체와 액체는 분사기 내부에서 만나게 된다. 또한 액체의 분무특성은 중심 분사기의 벽에 의해 영향을 받는다. 액체 분사기의 경우, 벽이 분사기 내 액막을 침범하는 정도가 커짐에 따라 저항이 증가하여 분무각이 감소한다. 그러므로 기체 분사각이 일정할 시, 액체 분무각이 감소한다면 분사기 외부에서 기체와 액체유동은 서로 충돌할 수 있다.

내부 혼합식과 외부 혼합식 분무 형상은 stroboscope를 사용한 backlight 방법으로 분무 패턴과 분무각을 측정하였다. 그러나 중심 기체 와류에 의해 액막은 분사기의 출구 근처에서 다수의 작은 액적으로 분열되므로 계측이 어렵다. 그러므로 평면 레이저를 사용하며, 다중산란을 제거하는 2-phase structured laser illumination planar imaging (2p-SLIPI) 기법을 사용하여 분무 단면에서 액막과 액적의 분포에 대한 실시간 정보를 획득하였다. 또한 동압센서를 사용하여 기체 분사의 압력진동을 계측하였다.

와류형 분사기를 빠져나온 기체는 회전하면서 축 방향으로 이동하기 때문에 액막 안쪽 표면을 바깥쪽으로 밀어내는 작용을 함과 동시에 속도증

가로 인한 압력감소를 동반한다. 내부 혼합식 분무에서는 혼합실 내에서부터 기체 흐름이 액막을 긁어내기 때문에 분사기 축 주위에서 미세 액적 구역이 생성된다. 외부 혼합식 분무에서는 충돌에 의해 액막을 파열시키기 때문에 미세액적은 속이 빈 원추형으로 분포하게 된다.

단일 와류형 분사기에 의한 액체 분무의 분열은 기체-액체 간 상호작용에 의한 파동으로 분열된다. 그러나 영상의 분석 결과에서 외부 혼합식 이원 분사기의 경우 액막 분열과정에 기체의 영향은 액체 흐름 자체의 특성에 비해 더욱 지배적이었다. 또한 기체의 압력진동은 액막을 진동시키며, 결과적으로 주기적으로 액막을 분열시키면서 액적을 생성하게 된다. 이러한 과정에서 분열주파수는 기체주파수의 약 1/10, 액막 파동주파수의 약 1/2 정도로 전이된 수치를 나타내었다. 그러나 분무 조건에 따라 분열주파수가 나타나지 않는 구간도 존재하였다. 대체로 분열주파수는 기체의 충돌속도와 액체의 속도에 비례하였으며, 액막의 공기역학적 저항은 유량 진동의 진동수와 진폭에 서로 다른 영향을 줄 수 있다는 것을 파악하였다.

주요어: 기체-액체 동축 분사기, 와류형 기체 분사기, 2p-SLIPI,
분열주파수, 액체로켓엔진

학 번: 2015-31003